PHYSICAL REVIEW B **106**, 094510 (2022)

Evolution of lattice, spin, and charge properties across the phase diagram of $\mathrm{FeSe}_{1-x}\mathrm{S}_x$

N. Lazarević,[1,*] A. Baum,[2,3,*] A. Milosavljević,[1] L. Peis,[2,3,†] R. Stumberger,[2,3,‡] J. Bekaert,[4] A. Šolajić,[1] J. Pešić,[1]
Aifeng Wang,[5] M. Šćepanović,[1] A. M. Milinda Abeykoon,[6] M. V. Milošević,[4] C. Petrovic,[7] Z. V. Popović,[1,8] and R. Hackl[2,3,9]
[1]*Center for Solid State Physics and New Materials, Institute of Physics Belgrade,*
University of Belgrade, Pregrevica 118, 11080 Belgrade, Serbia
[2]*Walther Meissner Institut, Bayerische Akademie der Wissenschaften, 85748 Garching, Germany*
[3]*Fakultät für Physik, Technische Universität München, 85478 Garching, Germany*
[4]*Department of Physics, University of Antwerp, Groenenborgerlaan 171, B-2020 Antwerp, Belgium*
[5]*School of Physics, Chongqing University, Chongqing 400044, China*
[6]*National Synchrotron Light Source II, Brookhaven National Laboratory, Upton, New York 11973, USA*
[7]*Condensed Matter Physics and Materials Science Department, Brookhaven National Laboratory, Upton, New York 11973-5000, USA*
[8]*Serbian Academy of Sciences and Arts, Kneza Mihaila 35, 11000 Belgrade, Serbia*
[9]*IFW Dresden, Helmholtzstr. 20, 01069 Dresden, Germany*

(Received 9 March 2022; revised 27 July 2022; accepted 26 August 2022; published 19 September 2022)

A Raman scattering study covering the entire substitution range of the $\mathrm{FeSe}_{1-x}\mathrm{S}_x$ solid solution is presented. Data were taken as a function of sulfur concentration x for $0 \leqslant x \leqslant 1$, of temperature and of scattering symmetry. All types of excitations including phonons, spins, and charges are analyzed in detail. It is observed that the energy and width of the iron-related B_{1g} phonon mode vary continuously across the entire range of sulfur substitution. The A_{1g} chalcogenide mode disappears above $x = 0.23$ and reappears at a much higher energy for $x = 0.69$. In a similar way the spectral features appearing at finite doping in A_{1g} symmetry vary discontinuously. The magnetic excitation centered at approximately 500 cm^{-1} disappears above $x = 0.23$ where the A_{1g} lattice excitations exhibit a discontinuous change in energy. The low-energy mode associated with fluctuations displays maximal intensity at the nematostructural transition and thus tracks the phase boundary.

DOI: 10.1103/PhysRevB.106.094510

I. INTRODUCTION

Iron-based compounds are widely believed to host unconventional superconductivity, thus being similar to cuprates or heavy fermion systems. All are characterized by competing phases including magnetism, crystal symmetry breaking or nematicity, and fluctuations of charge and spin prior to superconductivity [1–3]. While long-range magnetic ordering was found in the majority of the compounds, it is absent in the binary compound FeSe. Yet a nematic and structural phase transition occurs simultaneously at 90 K [4–6]. Below $T_c =$ 9 K superconductivity is observed [7]. Upon applied pressure T_c increases to approximately 37 K [8]. By substituting sulfur for selenium, the transition temperature to the nematic phase is suppressed to zero for $x \sim 0.2$ [9], suggesting the existence of a quantum critical point (QCP), and a depression of T_c to approximately 2 K. For $x > 0.2$, T_c increases again and reaches 5 K at $x = 1$ [10]. Surprisingly enough, FeS displays a metallic variation of the resistivity and a high residual resistivity ratio RRR of approximately 30, and neither structural nor nematic phase transitions occur [11]. Thus, $\mathrm{FeSe}_{1-x}\mathrm{S}_x$ uniquely offers access to instabilities and critical points and the disappearance thereof while superconductivity survives.

FeSe and FeS are isostructural, thus providing us with the opportunity to probe the evolution of competing order by isoelectronic substitution. We wish to address the question as to which extent the properties and, specifically, superconductivity are interrelated with the other instabilities and how the electronic properties affect the phonons. We employ inelastic light scattering to probe evolution with composition of lattice spin and charge excitations in $\mathrm{FeSe}_{1-x}\mathrm{S}_x$ [12]. We identify the A_{1g} and B_{1g} modes, a two-phonon scattering process as well as additional modes that can be traced to either defect-induced or second-order scattering. The obtained experimental results are in good agreement with numerical calculations. Phonons self-energy temperature dependence supports the results reported in Refs. [13,14] where emerging short-range magnetic order at approximately 20 K was reported.

II. EXPERIMENT

Single crystals of $\mathrm{FeSe}_{1-x}\mathrm{S}_x$ were synthesized as described elsewhere [15]. Before the experiment the samples were cleaved in air.

Inelastic light scattering on phonons was performed using a Tri Vista 557 Raman spectrometer with the first

---

[*] These authors contributed equally to this work.

[†] Present Address: IFW Dresden, Helmholtzstr. 20, 01069 Dresden, Germany.

[‡] Present Address: Robert Bosch GmbH, Robert-Bosch-Platz 1, 70839 Gerlingen, Germany.

Published by the American Physical Society under the terms of the Creative Commons Attribution 4.0 International license. Further distribution of this work must maintain attribution to the author(s) and the published article's title, journal citation, and DOI.

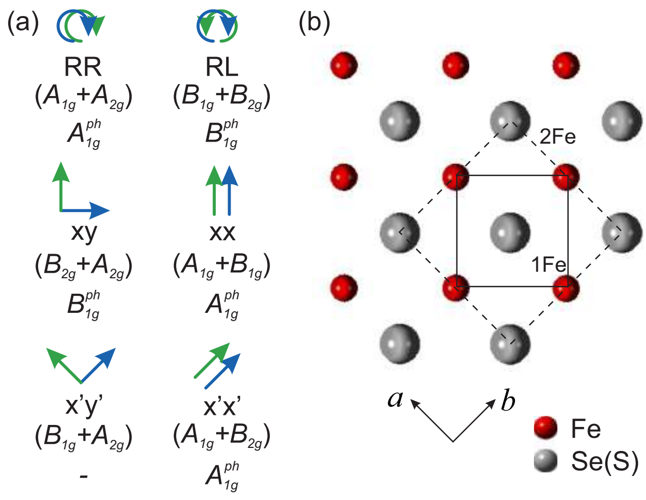

FIG. 1. Crystal structure and selection rules for FeSe(S). Solid and dashed lines represent the 1-Fe and the crystallographic 2-Fe unit cell, respectively. The crystallographic axes are *a* and *b*. In FeSe and FeS only one A_{1g} and one B_{1g} phonon is expected as indicated by A_{1g}^{ph} and B_{1g}^{ph}, respectively. The symmetries projected with the polarizations indicated symbolically with respect to the 1-Fe cell are relevant for electronic and spin excitations. The symmetries of the phonons are in brackets.

two monochromators coupled subtractively and the grating combination 1800/1800/2400 grooves/mm. For excitation a Coherent Verdi G solid state laser was used emitting at 532 nm. The samples were mounted in a KONTI CryoVac continuous helium flow cryostat having a 0.5-mm-thick window. The vacuum was pumped to the range of 10^{-6} mbar using a turbo molecular pump. The laser was focused to a spot size of approximately 8 μm using a microscope objective lens with ×50 magnification. The power absorbed by the sample was $P_a = 0.75$ mW. In backscattering configuration as used here, the incident and scattered photons propagate parallel to the crystallographic *c* axis. All Raman spectra were divided by the Bose factor.

Fluctuations and two magnon excitations were probed with a calibrated scanning spectrometer. The samples were attached to the cold finger of a He-flow cryostat having a vacuum of better than 10^{-6} mbar. A diode-pumped solid state laser emitting at 575 nm (Coherent GENESIS) was used as an excitation source. The laser beam was focused on the sample at an angle of incidence of 66° to a spot of $2r_{\mathrm{f}} \approx 50$ μm. Polarization and power of the incoming light were adjusted in a way that the light inside the sample had the proper polarization state and a power of $P_a = 4$ mW independent of polarization. The ratio P_a/r_{f} is similar for the μ setup and thus the local heating for both experiments can be estimated to be in the range 3–5 K. All four symmetries of the D_{4h} group, A_{1g}, A_{2g}, B_{1g}, and B_{2g}, can be accessed using appropriate in-plane polarizations of the incident and scattered light.

The selection rules are dictated by the crystal structure. Here, only polarizations in the *ab* plane are relevant, as shown in Fig. 1, with solid and dashed lines representing 1-Fe and 2-Fe unit cells, respectively. For the tetragonal system there are six principal scattering geometries and each probes two symmetry channels. We align our laboratory system with the 1-Fe unit cell. As a consequence, the B_{1g} phonon (B_{1g}^{ph}) is observable in the *xy* configuration which corresponds to the B_{2g} symmetry channel in the 2-Fe cell (Fig. 1). We decided to use this orientation since our main focus here is electronic and spin excitations for which the 1-Fe unit cell is more appropriate. A_{1g}^{ph} is the fully symmetric in-phase Se(S) mode with elongations along the *c* axis; B_{1g}^{ph} corresponds to the out-of-phase vibration of the Fe atoms parallel to the *c* axis.

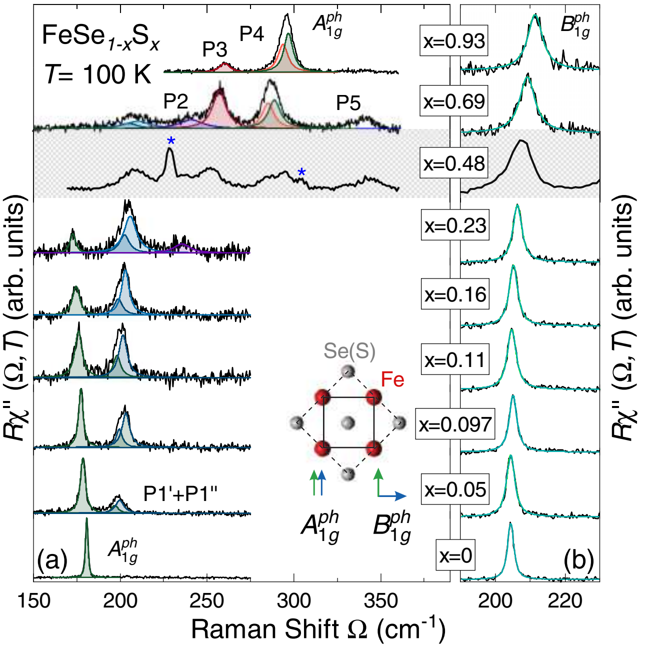

FIG. 2. Phonon spectra of FeSe$_{1-x}$S$_x$ measured at 100 K. We show *xx* and *xy* spectra where *x* and *y* are rotated by 45° with respect to the 2-Fe unit cell, as indicated in the inset, and project A_{1g}^{ph} and B_{1g}^{ph}, respectively. (a) A_{1g}^{ph} spectra. Only for pure FeSe ($x = 0$), a single line is observed at the A_{1g} energy of 165 cm^{-1} expected from lattice dynamics. Above $x = 0.23$ the Se(S) vibration becomes unobservable and reappears only for $x \geqslant 0.69$ at a much higher energy of approximately 290 cm^{-1} similar to that in pure FeS. The spectrum at $x = 0.48$ was measured on the scanning spectrometer and is therefore shaded. There may be an indication of the A_{1g}^{ph} phonon at about 290 cm^{-1}. The peaks other than Raman-active phonons are labeled P1–P5 with increasing energy. Those with asterisks correspond to maxima in the phonon density of states (Fig. 6). Solid lines represent the best fits to the data using Voigt profiles. (b) B_{1g}^{ph} spectra. Energy and linewidth vary continuously with sulfur content.

III. RESULTS AND DISCUSSION

A. Lattice excitations

First, the focus is placed on lattice excitations observable in the *xx* and *xy* scattering configuration projecting A_{1g}^{ph} and B_{1g}^{ph} in the spectral range characteristic for phonons. Figure 2 shows the evolution of the spectra with doping *x*, where *x* indicates the sulfur concentration. Additional spectra for $x = 0.48$ and, for convenience, $x = 1$ are shown in Fig. 7. In order to minimize the thermal broadening of the modes while staying above the nematic phase transition, the spectra

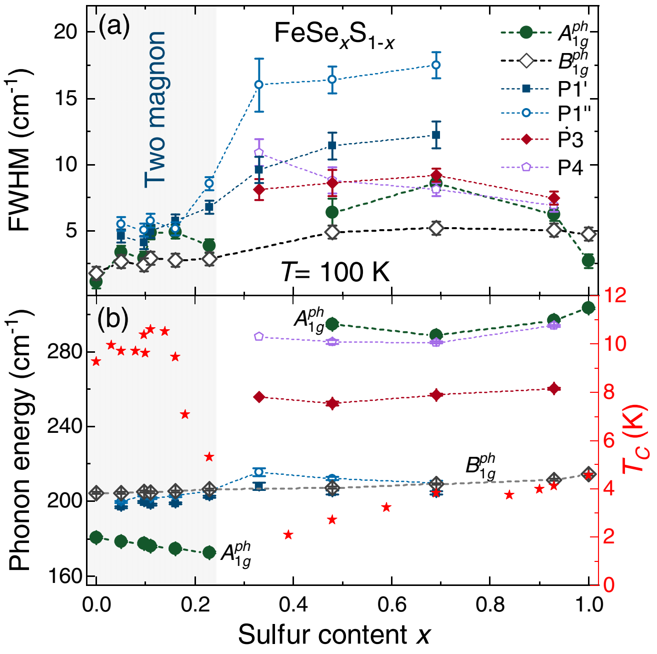

FIG. 3. Energies and linewidths of the Raman-active modes and T_c in FeSe$_{1-x}$S$_x$ as a function of sulfur content x at 100 K. (a) Peak widths (FWHM) and (b) energies as obtained from the fits (left axis). The T_c values of the corresponding solid solution are taken from Ref. [16].

were recorded at 100 K. In pure stoichiometric compounds only one A_{1g}^{ph} and one B_{1g}^{ph} phonon mode is expected (see Fig. 1). This is indeed the case for FeSe [Fig. 2(a), bottom] as described by Gnezdilov *et al.* [17] and corroborated here. In contrast, in pure FeS ($x = 1$) additional modes exist in the *xx* spectrum which were assigned to two-phonon scattering (265 cm^{-1}) and a projection of the phonon density of states (PDOS) (~300 cm^{-1}) [18] as reproduced in Fig. 7(b). The *xy* spectra show only the B_{1g}^{ph} mode for all doping levels displayed here [see also Fig. 7(a)]. It hardens monotonously and exhibits a weak maximum of the linewidth at $x = 0.69$ and $x = 0.93$ highlighting the effect of disorder as summarized in Figs. 3(a) and 3(b).

The *xx* spectra display a much more complex doping dependence. Upon substituting only a small amount of sulfur ($x = 0.05$) for selenium an additional structure appears at about 200 cm^{-1} [Fig. 2(a)]. Closer inspection of the FeSe$_{0.95}$S$_{0.05}$ spectra reveals that this feature consists of two peaks denoted as P1′ and P1″. With increasing x, these structures gain intensity and harden slightly, whereas the A_{1g} phonon softens, gradually loses intensity, and becomes undetectable at concentrations above $x = 0.23$. It reappears as a clear peak only for $x \geqslant 0.69$ at a much higher energy characteristic for FeS [18] and possibly as a remnant structure in the spectrum for $x = 0.48$ [Fig. 7(a)]. As in FeS the A_{1g}^{ph} peak overlaps with a weaker structure which is compatible with the PDOS (P4). At $x = 0.69$ P4 is approximately as strong as the A_{1g} phonon. Here [and at $x = 0.48$, Fig. 7(a)] there is also a broad feature at 340 cm^{-1} (P5). For $x = 0.93$ similar to $x = 1$ there is another structure at 250 cm^{-1} (P3) which gains intensity toward $x = 0.69$ where it has a weak companion at 235 cm^{-1} (P2) being present down to $x = 0.23$. As expected, the increase of crystalline disorder due to substitution leads to a broadening of all observed modes to some maximum value before the trend reverses for compositions close to pure FeS. The widths and energies of the stronger modes are summarized in Fig. 3. As opposed to the B_{1g}^{ph} phonon in *xy* configuration, all modes in *xx* polarization including the Raman-active phonon depend quasidiscontinuously on substitution.

This dichotomy of the substitution dependence of the phonon part in *xx* and *xy* configuration is the most remarkable effect of this study. Whereas the continuous evolution of the Fe B_{1g} line by and large tracks the degree of disorder and lattice contraction, the Se/S A_{1g} mode varies counterintuitively. Naively one would expect a continuous (not necessarily trivial) increase in the phonon frequency and maximal broadening for doping levels around $x = 0.5$ similar to what is observed in isotopically substituted semiconductors [19]. However, the line disappears after a continuous loss of intensity at approximately $x = 0.23$ and 172 cm^{-1} and reappears (presumably) at $x = 0.48$ slightly below 300 cm^{-1}. At low doping the A_{1g} energy decreases by 4% although S is lighter than Se by a factor of 2.13 and the lattice contracts. Above $x = 0.48$ the energy of the A_{1g} phonon varies as expected [see Fig. 3(b)].

The structures appearing in addition to the allowed phonons are rather difficult to interpret in detail. There are essentially two possibilities for intensity to appear in addition to the phonons: defect-induced scattering projecting the PDOS on the site of the defect or overtone (combination) scattering [20]. In FeS one of the peaks (P3) is in the gap between the acoustic and the optical branches and was therefore assigned to an overtone, whereas P4 may originate from the PDOS [18]. The two features depend in the same fashion on doping as the A_{1g} phonon, and the assignment may be maintained. This is plausible on the basis of the PDOS (Fig. 6) although the PDOS of a solid solution cannot be calculated straightforwardly. If we argue that the extra lines vary as discontinuously as the phonon, P1′ and P1″ would have both an overtone and a PDOS component. Interestingly, P1′ and P1″ have the expected doping dependence [see Fig. 3(b)].

The anomalous doping dependence of the A_{1g} phonon may indicate an enhanced electron-phonon coupling which manifests itself also in the linewidth (on top of the inhomogeneous broadening) [Fig. 3(a)]. The slightly enhanced electron-phonon coupling may boost T_c a little bit until the structure becomes unstable and T_c decreases rapidly for $x > 0.16$. There is, in fact, a kink in the c/a ratio at $x = 0.23$ which may be related to the structural instability [15]. In a recent preprint the collapse of T_c is almost precipitous and coincides with the end of the nematic phase [21], and one may speculate about the position of the quantum critical point and its impact. Yet, further work is necessary to finally clarify the issue.

B. Spin excitations and fluctuations

Second, we focus on the electronic B_{1g} symmetry channel projected in the $x'y'$ (1-Fe) configuration. Figure 4 shows the doping dependence of the high-energy Raman spectra at approximately 4 K. The A_{2g} contribution can be neglected in these materials [22]. A broad excitation centered at about

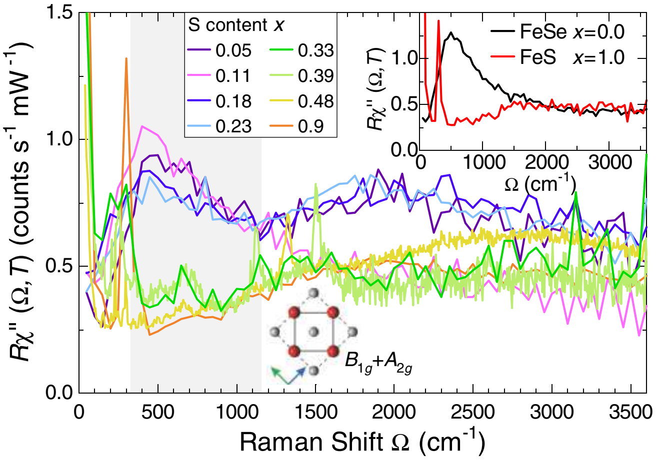

FIG. 4. Doping dependence of the high-energy spectra of $FeSe_{1-x}S_x$ in xy (2-Fe) configuration at 4 K, except for $x = 0.33$, $x = 0.39$, and $x = 0.48$ which were obtained at 100 K. For the electronic unit cell (full line in Fig. 1) relevant here the B_{1g} and A_{2g} symmetries are projected where A_{2g} is negligibly weak. The doping levels are indicated. The inset compares the high-energy spectra of pure FeSe [22] and FeS. The maximum in the range 500 cm^{-1} is compatible with two-magnon scattering [23], whereas the broad shoulder around 2000 cm^{-1} appearing in three out of ten (including all doping levels) spectra was identified as luminescence by using various laser lines for excitation. The peaks in the range 700–1550 cm^{-1} observed only for the doping levels $x = 0.33$, $x = 0.39$, and $x = 0.48$ may originate from either overtones of the phonon density of states [20,24] or from magnetic excitations in the paramagnetic state above the magnetic phase which was observed recently below 20–40 K [25,26]. Since the measuring temperature is well above the magnetic transition the former is more likely.

500 cm^{-1} dominates the spectrum at $x = 0$ which was interpreted in terms of two-magnon scattering [22]. Since the ratio of the nearest to the next-nearest-neighbor exchange coupling $J1$ and $J2$ is close to 0.5 [27] the system is a nearly frustrated antiferromagnet. Consequently the two-magnon Raman peak is pushed to energies well below $3J1$ [23]. No comparable feature is observed in FeS (see inset in Fig. 4).

Upon doping, the two-magnon peak remains relatively robust up to $x = 0.23$ and is absent for higher doping levels. This goes in line with the fact that for $x = 0$, the Fermi velocity in the d_{xy} band, $v_F^{(xy)}$, is significantly smaller than $v_F^{(xz)}$ or $v_F^{(yz)}$ and increases by only 10% for $x \leqslant 0.20$. For $x > 0.20$ $v_F^{(xy)}$ increases significantly towards FeS [28]. Generally, $v_F^{(xy)}$ in FeSe is smaller than $v_F^{(xy)}$ in $Ba(Fe_{1-x}Co_x)_2As_2$ for instance [29], in agreement with theoretical predictions [30–32]. Thus FeSe is close to the localization limit, and the two-magnonlike response may result from the rather slow carriers on the d_{xy} band. In contrast, the more itinerant carriers in the pnictides condense into a stripelike spin density wave (SDW) which becomes manifest in a gap and a coherence peak [22,33].

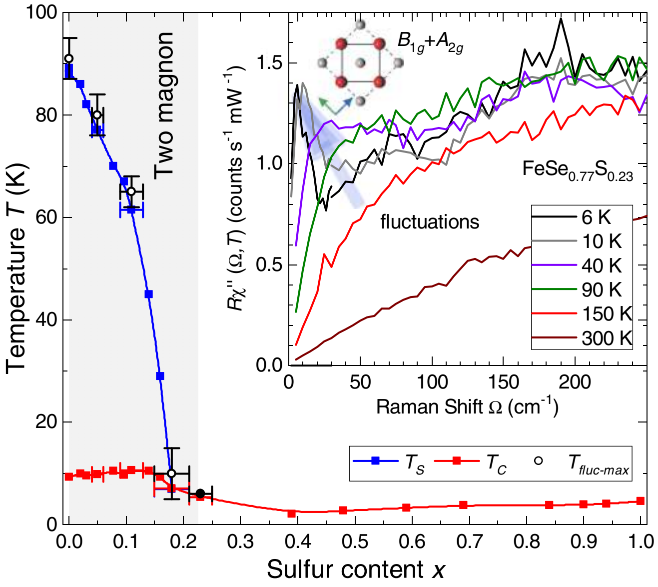

FIG. 5. Phase diagram of $FeSe_{1-x}S_x$ with $T_{\mathrm{fluct,max}}$ tracing T_S in the region where the two-magnon feature was observed in the Raman scattering experiment. T_c taken from Ref. [15]. The full circle represents the lowest accessible temperature. Inset: Low-energy Raman spectrum showing the temperature dependence of the fluctuation contribution at $x = 0.23$. Spectra for all doping levels $0 \leqslant x \leqslant 0.23$ are shown in Fig. 8.

In the energy region $\Omega < 200$ cm^{-1} extra intensity is observed for low temperatures. In FeSe it becomes clearly visible below 200 K and fills the spectral gap below the magnon at 500 cm^{-1}. Below approximately 100 K an isolated peak may be observed for $x = 0$ which continuously softens above the structural transformation at $T_s = 90$ K, fades away below T_s, and almost vanishes at 21 K [22,34]. The line shape and the temperature dependence above T_s can be described quantitatively in terms of critical fluctuations in a similar fashion as in $Ba(Fe_{1-x}Co_x)_2As_2$ [22,33,35]. For increasing doping, this extra intensity starts to develop at lower temperatures. However, remarkably enough the temperature where this peak's intensity is maximal, $T_{\mathrm{fluct,max}}$, always coincides with the respective transition temperature $T_s(x)$. At $x = 0.23$ the fluctuation response gains intensity down to the lowest accessible temperatures as presented in the inset of Fig. 5. Thus, the phase transition line of the nematic phase can also be tracked by the Raman response. For $x = 0.33$ (the next available doping level) the fluctuation response cannot be observed any further. Concomitantly, the two-magnon excitation at 500 cm^{-1} becomes unobservable. The most likely explanation of this coincidence is that the two phenomena have the same origin and result from spin excitations. However, there is no consensus on that view in the literature, and Zhang *et al.* [36] and Chibani *et al.* [34] interpret the same experimental observation in terms of quadrupolar charge fluctuations. Yet, one certainly has to answer the question as to why the fluctuations are not found in the simulations [23].

Most probably, the length scale the simulations can deal with limits the applicability of the exact diagonalization method. Since it was intended to study the temperature dependence the cluster had to be sufficiently small (4×4) to keep the time for the simulations finite [23]. For the two-magnon excitations, the 4×4 cluster is sufficient because only nearest-neighbor spins are important. However, close to the transition the correlation length of fluctuations diverges making them inaccessible for the small clusters tractable numerically. Actually, well above the transition there is a shoulder on the low-energy side of the two-magnon peak which may be associated with the fluctuations but the shoulder is lost close to T_s. Thus, although there are experimental arguments in favor of spin fluctuations at low energy there is no theoretical support for this conjecture.

The last question we wish to address concerns the origin of possible local or quasilocal spin order in $FeSe_{1-x}S_x$ for $x < 0.3$. It was observed a while ago that the width of the various bands derived from the orbitals close to the Fermi surface varies by approximately a factor of 3 or more. There are itinerant yz and xz bands crossing the Fermi surface at E_F and a weakly dispersing xy band just below E_F [29] on which the nearly localized spins may reside [30,32]. It is an important question to which extent the fluctuations at low energy are related to these spins. As a matter of fact, Ba122 displays itinerant SDW magnetism as manifested by a gap and a coherence peak along with fluctuations [22,33], whereas FeSe exhibits signatures of local spins and also fluctuations at low energies as shown here. In $FeSe_{1-x}S_x$ both phenomena disappear together above $x > 0.23$.

IV. CONCLUSION

Raman results covering the entire substitution range $0 \leqslant x \leqslant 1$ in $FeSe_{1-x}S_x$ were presented. The main goal was the study of the physics around the QCP where the nematic instability approached zero transition temperature in the range $0.16 \leqslant x \leqslant 0.23$. We find a striking signature of this transition in both the phonon and the electronic spectra. Whereas the B_{1g} phonon varies continuously with S substitution, the A_{1g} phonon and all structures in the xx spectra show a discontinuity above $x = 0.23$. Similarly, the electronic spectra dominated by spin excitations change abruptly here. Both the two-magnon excitations and the low-energy fluctuations disappear. We argue that they are interrelated. Since we could not observe gap excitation for $x > 0$, statements about the evolution of the superconducting pairing are currently not possible. Another issue is the exact position of the quantum critical transition and its sharpness.

ACKNOWLEDGMENTS

We acknowledge valuable discussions with T. Böhm and D. Jost. The authors acknowledge funding provided by the Institute of Physics Belgrade through a grant by the Ministry of Education, Science and Technological Development of the Republic of Serbia and and SASA Project No. F-134. The work was supported by the Science Fund of the Republic of Serbia, PROMIS, No. 6062656, StrainedFeSC, by Research Foundation-Flanders (FWO), and COST actions CA16218 and CA21144. Further support came from the German research foundation (DFG) via projects Ha2071/8-1, Ha2071/12-1, and 107745057-TRR 80 and from the DAAD via the project-related personal exchange program PPP with Serbia Grant No. 57449106. J.B. is Senior Postdoctoral Fellow of the FWO, and further acknowledges the Erasmus+ program for staff mobility and training (KA107, 2018) for a research stay at the Institute of Physics Belgrade. The computational resources and services used for the first-principles calculations in this work were provided by the VSC (Flemish Supercomputer Center), funded by the FWO and the Flemish Government, department EWI. Work at Brookhaven National Laboratory is supported by the U.S. DOE under Contract No. DESC0012704 (materials synthesis).

APPENDIX A: PHONON DISPERSION AND DENSITY OF STATES

We have performed density functional theory (DFT) calculations as implemented in the ABINIT package [38]. We have used the Perdew-Burke-Ernzerhof functional tailored for solids [39] and optimized norm-conserving pseudopotentials [40,41], where Fe $3s^2 3p^6 3d^6 4s^2$, S $3s^2 3p^4$, and Se $3d^{10} 4s^2 4p^4$ are treated as valence electrons. The energy cutoff for the plane-wave basis was set to 50 Ha. The lattice parameters and atomic positions used in the calculations were directly obtained from our x-ray diffraction measurements (performed at 300 K). Following previous first-principles studies on phonons in, for example, FeS [18], the crystal structures were not further relaxed, to achieve optimal characterization of the phonon frequencies. Here, both FeS and FeSe adopt the simple tetragonal space group $P4/nmm$ (No. 129), where Fe occupies Wyckoff position $2a$ and S/Se position $2c$. The latter comprises an additional degree of freedom, namely, the height of the chalcogen atoms S and Se with respect to the Fe plane, denoted as z. An overview of the lattice parameters that were used in the calculations is provided in Table I.

Subsequently, the phonon dispersions were obtained from density functional perturbation theory (DFPT) calculations, also within ABINIT. Here, we have used a $15 \times 15 \times 9$ k-point grid for the electron wave vectors and a $5 \times 5 \times 3$ q-point grid for the phonon wave vectors. For the electronic occupation we employed Fermi-Dirac smearing with broadening factor $\sigma = 0.01$ Ha.

The results of these calculations are shown in Fig. 6. FeS is found to have phonon frequencies stretching up to 344 cm^{-1} [Fig. 6(a)], which is significantly higher than the maximum phonon value of 273 cm^{-1} obtained for FeSe [Fig. 6(b)], owing to the higher atomic mass of Se compared to S. The atom-resolved phonon densities of states (DOS) of both compounds reveal a mixture of iron and chalcogen contribution throughout the entire phonon spectrum [Figs. 6(c) and 6(d)]. Interestingly, there is a change of dominant phonon character, with the lower modes dominated by Fe in FeS, while the lower modes have predominant Se character in FeSe. This reversal can be understood from the fact that the atomic number of Fe ($Z = 26$) lies in between those of S ($Z = 16$) and Se ($Z = 34$). These differences in atomic masses lead moreover

TABLE I. Lattice parameters, obtained from x-ray diffraction measurements, used in the DFT and DFPT calculations.

Compound	a (Å)	c (Å)	z (units of c)
FeS	3.6795	5.0321	0.2578
FeSe	3.7707	5.5202	0.2671

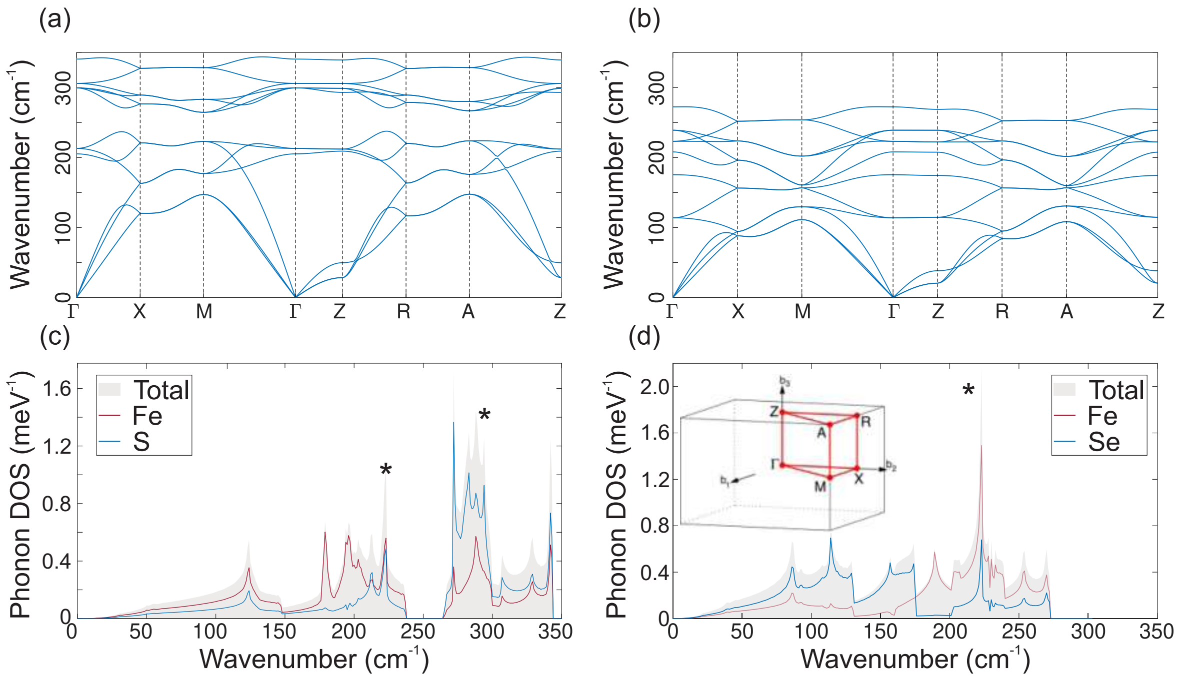

FIG. 6. Calculated phonon band structures of (a) FeS and (b) FeSe. Phonon DOS of (c) FeS and (d) FeSe, including partial contributions from Fe and S/Se. The Brillouin zone of both structures depicted in black is shown in the inset of (d), with the irreducible Brillouin zone, along which the band structures are plotted, in red [37]. The energies of the extra peaks in Fig. 7 are also indicated here by asterisks.

to a small energy gap between Fe- and S-dominated modes in FeS (between 238 and 265 cm^{-1}), which is entirely absent in FeSe.

APPENDIX B: FeSe$_{0.52}$S$_{0.48}$ AND FeS

For convenience we show here additional doping levels in Fig. 7. The spectrum for $x = 1$ in panel (b) was already published elsewhere [18]. Note that for $x'x'$ both A_{1g}^{ph} and B_{1g}^{ph} are projected and that the labels for the symmetry-forbidden peaks P3 and P4 are different from those in the earlier paper [18]. $x = 0.48$ [Fig. 7(a)] is in the middle between FeSe and FeS, and one can therefore expect the strongest contribution from defect-induced scattering. This interpretation is supported by the presence of structures in both configurations. All peaks resolved at $x = 0.69$ in xx configuration are also observed here. In addition there are two lines marked by asterisks which appear only at $x = 0.48$. Since they appear also for $x'x'$ we interpret them in terms of contributions from the PDOS as shown in Fig. 6 where the respective energies correspond to a high DOS of either FeSe or FeS. Structure P5 may be related to the high-energy part of FeS.

APPENDIX C: FLUCTUATION RESPONSE

The Raman response from fluctuations was studied by various authors [22,36,42]. While the experiments agree by and large, the interpretation is still controversial. Here we show that the fluctuations appear along with the two-magnon excitations at approximately 500 cm^{-1} from a frustrated spin system [22,23]. Above $x = 0.23$ we could neither observe fluctuations nor two-magnon excitations (see Fig. 4). We cannot entirely exclude that the fluctuations are masked by insufficient stray-light rejection in the more disordered samples but consider it unlikely.

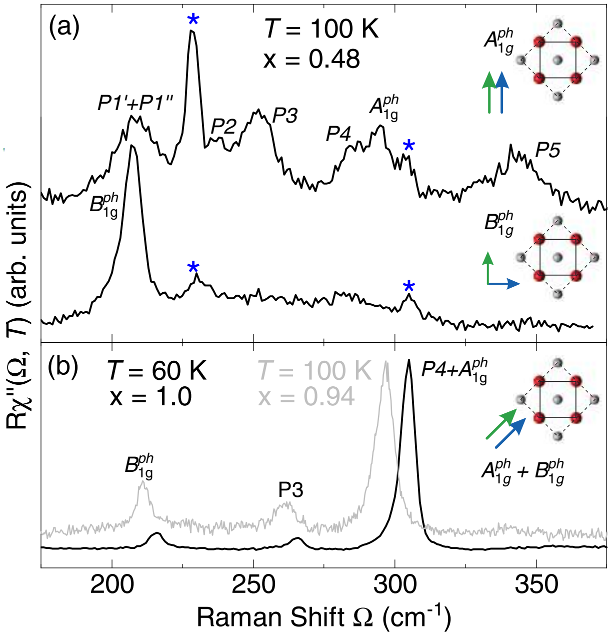

FIG. 7. FeSe$_{1-x}$S$_x$ for $x = 0.48$, $x = 0.94$, and $x = 1$. (a) A_{1g}^{ph} (xx) and B_{1g}^{ph} (xy) spectra for FeSe$_{0.52}$S$_{0.48}$. In addition to the phonons and the structures observed at the other doping levels there are two relatively sharp lines (marked by asterisks) which we associate with the PDOS. They may also arise from a nearly ordered superstructure close to 50% doping.

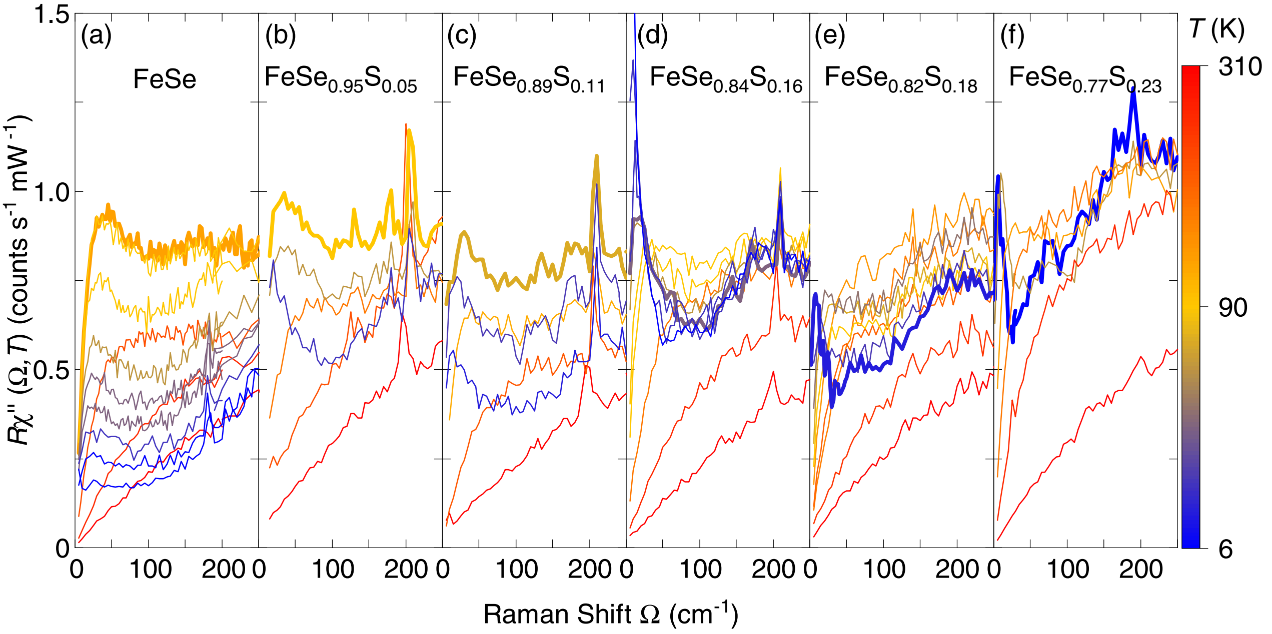

FIG. 8. Fluctuation response of $FeSe_{1-x}S_x$ for $0 \leqslant x \leqslant 0.23$. The spectra with the maximal intensity in the fluctuations are highlighted. The respective temperatures are (a) 91 K, (b) 80 K, (c) 65 K, (d) 25 K, (e) 10 K, and (f) 6 K, where 6 K was the lowest accessible temperature. The temperatures are compiled in Fig. 5 and track the transition to the nematic phase.

If excitations are very close to zero energy one encounters two difficulties: (1) The experimentally accessible quantity is the differential cross section, $d^2\sigma/(d\Omega\, d\omega) \propto S(q=0,\omega)$. The dynamical structure factor or Van Hove function $S(q=0,\omega)$ is related to the imaginary part of the Raman response function $\mathrm{Im}\chi(q=0,\omega)$ through the fluctuation-dissipation theorem as $S(q=0,\omega) = \pi^{-1}\{1 + n(\omega, T)\}\mathrm{Im}\chi(q=0,\omega)$ [43]. The Bose factor $1 + n(\omega, T)$ increases rapidly towards $\omega = 0$ for $\hbar\omega < k_B T$ and conceals all spectral features below $k_B T$. Since the fluctuation-dissipation theorem is derived on purely statistical arguments the response function contains exactly the same information as the structure factor but makes features at low energy visible. Thus it is sensible to show $\mathrm{Im}\chi(q=0,\omega)$ rather than $S(q=0,\omega)$. (2) If the surface is not atomically flat there is stray light from insufficient rejection of the laser. The problem is aggravated when atoms of the residual gas accumulate on the surface at low temperature. In panels (a), (b), and (d) of Fig. 8 this effect can be observed. Fortunately, it can be distinguished from the desired response which always goes through zero linearly for causality reasons. (a) In FeSe only the spectra at 10 K show a slight increase which, however, is separated from the fluctuation peak at finite energy. (b) The increase at 10 K is partially resulting from stray light but the maximal intensity is already observed at 80 K. (c) There is little contribution from stray light. (d) Here the stray light becomes strong below 20 K. In (e) and (f) the stray light is negligible.

Remarkably, the overall intensity of all spectra is approximately the same, whereas the maximal intensity in the fluctuation peak is observed at different temperatures as indicated in Fig. 8. These temperatures compare well with the boundary of the nematic phase as shown in Fig. 5.

---

[1] D. J. Scalapino, A common thread: The pairing interaction for unconventional superconductors, Rev. Mod. Phys. **84**, 1383 (2012).

[2] E. Fradkin, S. A. Kivelson, and J. M. Tranquada, *Colloquium*: Theory of intertwined orders in high temperature superconductors, Rev. Mod. Phys. **87**, 457 (2015).

[3] S. Lederer, Y. Schattner, E. Berg, and S. A. Kivelson, Enhancement of Superconductivity near a Nematic Quantum Critical Point, Phys. Rev. Lett. **114**, 097001 (2015).

[4] A. E. Böhmer, T. Arai, F. Hardy, T. Hattori, T. Iye, T. Wolf, H. v. Löhneysen, K. Ishida, and C. Meingast, Origin of the Tetragonal-to-Orthorhombic Phase Transition in FeSe: A Combined Thermodynamic and NMR Study of Nematicity, Phys. Rev. Lett. **114**, 027001 (2015).

[5] T. M. McQueen, A. J. Williams, P. W. Stephens, J. Tao, Y. Zhu, V. Ksenofontov, F. Casper, C. Felser, and R. J. Cava, Tetragonal-to-Orthorhombic Structural Phase Transition at 90 K in the Superconductor $Fe_{1.01}Se$, Phys. Rev. Lett. **103**, 057002 (2009).

[6] M. D. Watson, T. K. Kim, A. A. Haghighirad, N. R. Davies, A. McCollam, A. Narayanan, S. F. Blake, Y. L. Chen, S. Ghannadzadeh, A. J. Schofield *et al.*, Emergence of the nematic electronic state in FeSe, Phys. Rev. B **91**, 155106 (2015).

[7] F.-C. Hsu, J.-Y. Luo, K.-W. Yeh, T.-K. Chen, T.-W. Huang, P. M. Wu, Y.-C. Lee, Y.-L. Huang, Y.-Y. Chu, D.-C. Yan, and M.-K. Wu, Superconductivity in the PbO-type structure α-FeSe, Proc. Natl. Acad. Sci. USA **105**, 14262 (2008).

[8] S. Medvedev, T. M. McQueen, I. A. Troyan, T. Palasyuk, M. I. Eremets, R. J. Cava, S. Naghavi, F. Casper, V. Ksenofontov, G. Wortmann, and C. Felser, Electronic and magnetic phase diagram of β-$Fe_{1.01}Se$ with superconductivity at 36.7 K under pressure, Nat. Mater. **8**, 630 (2009).

[9] Y. Sato, S. Kasahara, T. Taniguchi, X. Xing, Y. Kasahara, Y. Tokiwa, Y. Yamakawa, H. Kontani, T. Shibauchi, and Y. Matsuda, Abrupt change of the superconducting gap structure at the nematic critical point in $FeSe_{1-x}S_x$, Proc. Natl. Acad. Sci. USA **115**, 1227 (2018).

[10] X. Lai, H. Zhang, Y. Wang, X. Wang, X. Zhang, J. Lin, and F. Huang, Observation of superconductivity in tetragonal FeS, J. Am. Chem. Soc. **137**, 10148 (2015).

[11] U. Pachmayr, N. Fehn, and D. Johrendt, Structural transition and superconductivity in hydrothermally synthesized FeX (X = S, Se), Chem. Commun. **52**, 194 (2016).

[12] N. Lazarević and R. Hackl, Fluctuations and pairing in Fe-based superconductors: Light scattering experiments, J. Phys.: Condens. Matter **32**, 413001 (2020).

[13] S. Holenstein, U. Pachmayr, Z. Guguchia, S. Kamusella, R. Khasanov, A. Amato, C. Baines, H.-H. Klauss, E. Morenzoni, D. Johrendt, and H. Luetkens, Coexistence of low-moment magnetism and superconductivity in tetragonal FeS and suppression of T_c under pressure, Phys. Rev. B **93**, 140506(R) (2016).

[14] F. K. K. Kirschner, F. Lang, C. V. Topping, P. J. Baker, F. L. Pratt, S. E. Wright, D. N. Woodruff, S. J. Clarke, and S. J. Blundell, Robustness of superconductivity to competing magnetic phases in tetragonal FeS, Phys. Rev. B **94**, 134509 (2016).

[15] A. Wang, A. Milosavljevic, A. M. M. Abeykoon, V. Ivanovski, Q. Du, A. Baum, E. Stavitski, Y. Liu, N. Lazarevic, K. Attenkofer *et al.*, Suppression of superconductivity and nematic order in $Fe_{1-y}Se_{1-x}S_x (0 \leqslant x \leqslant 1; y \leqslant 0.1)$ crystals by anion height disorder, Inorg. Chem. **61**, 11036 (2022).

[16] A. Wang, L. Wu, V. N. Ivanovski, J. B. Warren, J. Tian, Y. Zhu, and C. Petrovic, Critical current density and vortex pinning in tetragonal $FeS_{1-x}Se_x$ ($x = 0, 0.06$), Phys. Rev. B **94**, 094506 (2016).

[17] V. Gnezdilov, Y. G. Pashkevich, P. Lemmens, D. Wulferding, T. Shevtsova, A. Gusev, D. Chareev, and A. Vasiliev, Interplay between lattice and spin states degree of freedom in the FeSe superconductor: Dynamic spin state instabilities, Phys. Rev. B **87**, 144508 (2013).

[18] A. Baum, A. Milosavljević, N. Lazarević, M. M. Radonjić, B. Nikolić, M. Mitschek, Z. I. Maranloo, M. Šćepanović, M. Grujić-Brojčin, N. Stojilović *et al.*, Phonon anomalies in FeS, Phys. Rev. B **97**, 054306 (2018).

[19] M. Cardona and M. L. W. Thewalt, Isotope effects on the optical spectra of semiconductors, Rev. Mod. Phys. **77**, 1173 (2005).

[20] G. Turrell, *Infrared and Raman Spectra of Crystals* (Academic, London/New York, 1972).

[21] Y. Mizukami, M. Haze, O. Tanaka, K. Matsuura, D. Sano, J. Böker, I. Eremin, S. Kasahara, Y. Matsuda, and T. Shibauchi, Thermodynamics of transition to BCS-BEC crossover superconductivity in $FeSe_{1-x}S_x$, arXiv:2105.00739.

[22] A. Baum, H. N. Ruiz, N. Lazarević, Y. Wang, T. Böhm, R. Hosseinian Ahangharnejhad, P. Adelmann, T. Wolf, Z. V. Popović *et al.*, Frustrated spin order and stripe fluctuations in FeSe, Commun. Phys. **2**, 14 (2019).

[23] H. Ruiz, Y. Wang, B. Moritz, A. Baum, R. Hackl, and T. P. Devereaux, Frustrated magnetism from local moments in FeSe, Phys. Rev. B **99**, 125130 (2019).

[24] W. Spengler and R. Kaiser, First and second order Raman scattering in transition metal compounds, Solid State Commun. **18**, 881 (1976).

[25] F. Nabeshima, Y. Kawai, N. Shikama, Y. Sakishita, A. Suter, T. Prokscha, S. E. Park, S. Komiya, A. Ichinose, T. Adachi, and A. Maeda, Sulfur-induced magnetism in $Fese_{1-x}s_x$ thin films on $LaAlO_3$ revealed by muon spin rotation/relaxation, Phys. Rev. B **103**, 184504 (2021).

[26] X. Yi, X. Xing, L. Qin, J. Feng, M. Li, Y. Zhang, Y. Meng, N. Zhou, Y. Sun, and Z. Shi, Hydrothermal synthesis and complete phase diagram of $FeSe_{1-x}S_x (0 \leqslant x \leqslant 1)$ single crystals, Phys. Rev. B **103**, 144501 (2021).

[27] J. K. Glasbrenner, I. I. Mazin, H. O. Jeschke, P. J. Hirschfeld, R. M. Fernandes, and R. Valentí, Effect of magnetic frustration on nematicity and superconductivity in iron chalcogenides, Nat. Phys. **11**, 953 (2015).

[28] A. I. Coldea, Electronic nematic states tuned by isoelectronic substitution in bulk $FeSe_{1-x}S_x$, Frontiers Phys. **8**, 594500 (2021).

[29] M. Yi, Z.-K. Liu, Y. Zhang, R. Yu, J.-X. Zhu, J. Lee, R. Moore, F. Schmitt, W. Li, S. Riggs *et al.*, Observation of universal strong orbital-dependent correlation effects in iron chalcogenides, Nat. Commun. **6**, 7777 (2015).

[30] Z. P. Yin, K. Haule, and G. Kotliar, Kinetic frustration and the nature of the magnetic and paramagnetic states in iron pnictides and iron chalcogenides, Nat. Mater. **10**, 932 (2011).

[31] K. M. Stadler, Z. P. Yin, J. von Delft, G. Kotliar, and A. Weichselbaum, Dynamical Mean-Field Theory Plus Numerical Renormalization-Group Study of Spin-Orbital Separation in a Three-Band Hund Metal, Phys. Rev. Lett. **115**, 136401 (2015).

[32] S. L. Skornyakov, V. I. Anisimov, D. Vollhardt, and I. Leonov, Effect of electron correlations on the electronic structure and phase stability of FeSe upon lattice expansion, Phys. Rev. B **96**, 035137 (2017).

[33] F. Kretzschmar, T. Böhm, U. Karahasanović, B. Muschler, A. Baum, D. Jost, J. Schmalian, S. Caprara, M. Grilli, C. Di Castro *et al.*, Critical spin fluctuations and the origin of nematic order in $Ba(Fe_{1-x}Co_x)_2As_2$, Nat. Phys. **12**, 560 (2016).

[34] S. Chibani, D. Farina, P. Massat, M. Cazayous, A. Sacuto, T. Urata, Y. Tanabe, K. Tanigaki, A. E. Böhmer, P. C. Canfield *et al.*, Lattice-shifted nematic quantum critical point in $FeSe_{1-x}S_x$, npj Quantum Mater. **6**, 37 (2021).

[35] U. Karahasanovic, F. Kretzschmar, T. Böhm, R. Hackl, I. Paul, Y. Gallais, and J. Schmalian, Manifestation of nematic degrees of freedom in the Raman response function of iron pnictides, Phys. Rev. B **92**, 075134 (2015).

[36] W. Zhang, S. Wu, S. Kasahara, T. Shibauchi, Y. Matsuda, and G. Blumberg, Quadrupolar charge dynamics in the nonmagnetic $FeSe_{1-x}S_x$ superconductors, Proc. Natl. Acad. Sci. USA **118**, e2020585118 (2021).

[37] W. Setyawan and S. Curtarolo, High-throughput electronic band structure calculations: Challenges and tools, Comput. Mater. Sci. **49**, 299 (2010).

[38] X. Gonze, B. Amadon, G. Antonius, F. Arnardi, L. Baguet, J.-M. Beuken, J. Bieder, F. Bottin, J. Bouchet, E. Bousquet *et al.*, The ABINIT project: Impact, environment and recent developments, Comput. Phys. Commun. **248**, 107042 (2020).

[39] J. P. Perdew, A. Ruzsinszky, G. I. Csonka, O. A. Vydrov, G. E. Scuseria, L. A. Constantin, X. Zhou, and K. Burke, Restoring the Density-Gradient Expansion for Exchange in Solids and Surfaces, Phys. Rev. Lett. **100**, 136406 (2008).

[40] D. R. Hamann, Optimized norm-conserving Vanderbilt pseudopotentials, Phys. Rev. B **88**, 085117 (2013).

[41] M. van Setten, M. Giantomassi, E. Bousquet, M. Verstraete, D. Hamann, X. Gonze, and G.-M. Rignanese, The PseudoDojo: Training and grading a 85 element optimized norm-conserving pseudopotential table, Comput. Phys. Commun. **226**, 39 (2018).

[42] P. Massat, D. Farina, I. Paul, S. Karlsson, P. Strobel, P. Toulemonde, M.-A. Méasson, M. Cazayous, A. Sacuto, S. Kasahara *et al.*, Charge-induced nematicity in FeSe, Proc. Natl. Acad. Sci. USA **113**, 9177 (2016).

[43] L. D. Landau and E. M. Lifshitz, *Electrodynamics of Continuous Media* (Pergamon, Oxford, 1960), p. 377.

Nanotechnology

PURPOSE-LED
PUBLISHING™

PAPER • OPEN ACCESS

Influence of crystal structure and oxygen vacancies on optical properties of nanostructured multi-stoichiometric tungsten suboxides

To cite this article: Bojana Višić *et al* 2022 *Nanotechnology* **33** 275705

View the article online for updates and enhancements.

You may also like

- A Solar Coronal Hole and Fast Solar Wind Turbulence Model and First-orbit Parker Solar Probe (PSP) Observations
  L. Adhikari, G. P. Zank and L.-L. Zhao
- Ab Initio Tomography Analysis of Lithium Incorporation and Diffusion in Multidomain Silicon Suboxide Anode Materials
  Somin Chae, Hyung-Kyu Lim and Sangheon Lee
- Oxide-Thickness-Dependent Suboxide Width and Its Effect on Inversion Tunneling Current
  Yen-Po Lin and Jenn-Gwo Hwu

This content was downloaded from IP address 147.91.83.249 on 06/03/2026 at 12:11

OPEN ACCESS
IOP Publishing
Nanotechnology
Nanotechnology **33** (2022) 275705 (11pp)
https://doi.org/10.1088/1361-6528/ac6316

Influence of crystal structure and oxygen vacancies on optical properties of nanostructured multi-stoichiometric tungsten suboxides

Bojana Višić[1,2,5], **Luka Pirker**[1,5], **Marko Opačić**[2], **Ana Milosavljević**[2], **Nenad Lazarević**[2], **Boris Majaron**[3,4] and **Maja Remškar**[1]

[1] Department of Condensed Matter Physics, Jozef Stefan Institute, Jamova Cesta 39, 1000 Ljubljana, Slovenia
[2] Institute of Physics Belgrade, University of Belgrade, Pregrevica 118, 11080 Belgrade, Serbia
[3] Department of Complex Matter, Jozef Stefan Institute, Jamova 39, 1000 Ljubljana, Slovenia
[4] Faculty of Physics and Mathematics, University of Ljubljana, Jadranska 19, Slovenia

E-mail: bojana.visic@ipb.ac.rs

Received 8 March 2022, revised 28 March 2022
Accepted for publication 31 March 2022
Published 20 April 2022

Abstract

Four distinct tungsten suboxide (WO_{3-x}) nanomaterials were synthesized via chemical vapour transport reaction and the role of their crystal structures on the optical properties was studied. These materials grow either as thin, quasi-2D crystals with the W_nO_{3n-1} formula (in shape of platelets or nanotiles), or as nanowires (W_5O_{14}, $W_{18}O_{49}$). For the quasi-2D materials, the appearance of defect states gives rise to two indirect absorption edges. One is assigned to the regular bandgap occurring between the valence and the conduction band, while the second is a defect-induced band. While the bandgap values of platelets and nanotiles are in the upper range of the reported values for the suboxides, the nanowires' bandgaps are lower due to the higher number of free charge carriers. Both types of nanowires sustain localized surface plasmon resonances, as evidenced from the extinction measurements, whereas the quasi-2D materials exhibit excitonic transitions. All four materials have photoluminescence emission peaks in the UV region. The interplay of the crystal structure, oxygen vacancies and shape can result in changes in optical behaviour, and the understanding of these effects could enable intentional tuning of selected properties.

Supplementary material for this article is available online

Keywords: tungsten oxides, Magnèli phases, nanowires, quasi-2D materials

(Some figures may appear in colour only in the online journal)

1. Introduction

The family of tungsten oxides, including stoichiometric WO_3 and WO_2 and substoichiometric Magnèli phases (WO_{3-x}, $0 < x < 1$), is widely studied due to numerous intriguing properties [1–5]. These tungsten (sub)oxides have been used as photodetectors [6, 7] and gas sensors [8–10], in photocatalysis and photoelectrochemical water splitting [3, 11, 12],

---

[5] These authors contributed equally.

Original content from this work may be used under the terms of the Creative Commons Attribution 4.0 licence. Any further distribution of this work must maintain attribution to the author(s) and the title of the work, journal citation and DOI.

© 2022 The Author(s). Published by IOP Publishing Ltd

in smart windows [13] and optoelectronics [14]. In bulk form, WO_3 is a large indirect bandgap n-type semiconductor, with bandgap values reported in the 2.6–3.0 eV range [15–17]. In nanosized WO_3, quantum size effects appear, resulting in a blueshift of the bandgap up to 3.25 eV, with the bandwidth modulation correlated to the size of the nanoparticles [18]. This is a direct consequence of the quantum confinement effect.

Due to the crystal shear mechanism, various sub-stoichiometric Magnèli phases with different combinations of edge- or corner-sharing WO_6 octahedra can be formed [19]. This may lead to appearance of crystal shear (CS) planes and pentagonal columns (PC), which form to accommodate oxygen vacancies [20, 21]. For less reduced suboxides (i.e. $x < 0.2$), CS planes occur; while PCs are formed for x greater than 0.2. In the former, CS planes' corner-sharing WO_6 octahedra become edge-sharing [22], while in the latter WO_7 bipyramids are formed and share their equatorial edges with the WO_6 octahedra [23]. The degree of reduction and appearance of oxygen vacancies can be crucial for understanding the change of the optical response with respect to the fully oxidized WO_3 [8]. Furthermore, it was reported that the oxygen vacancy defect states induced by annealing can significantly improve electrical conductivity [24]. Substoichiometric WO_{3-x} are mostly found to be blue or light green, which is a structure-sensitive phenomenon and is mainly a consequence of the stoichiometry or oxygen vacancies [25, 26]. First-principles pseudopotential and total-energy projector-augmented wave method calculations showed that single oxygen vacancies and substoichiometric crystal structures modify the optical properties and generate different types of defect states in the bulk [27, 28].

For nanostructured $WO_{3-x,}$ various phenomena may lead to different size- and shape- dependent behaviour within the same stoichiometry. This can lead to seemingly contradictory results, if only the effect of the degree of reduction is considered. It was reported that the metallic $WO_{2.83}$ nanorods ($W_{24}O_{68}$) can sustain strong localized surface plasmon resonances (LSPR), centred around 1.4 eV (corresponding to $\lambda = 900$ nm) [26]. Electrical transport measurements of $WO_{2.8}$ (W_5O_{14}) show that they exhibit metallic behaviour [29]. On the other hand, based on electrical transport measurements and photoluminescence spectra, $WO_{2.72}$ ($W_{18}O_{49}$) nanowires (NWs) show a semiconducting behaviour [30, 31].

A close relationship between the creation of oxygen vacancies and stoichiometry (i.e. degree of reduction) and morphology has been reported [32–34]. Both the stoichiometry and the amount of oxygen vacancies heavily depend on the synthesis conditions, and in turn determine the optical and electrical properties, such as photoluminescense and electrical conductivity. Therefore, a careful structural study of these materials is significant for interpreting optical spectra. In this paper, we report on optical properties of various nanostructured suboxides; namely, multistoichiometric W_nO_{3n-1} in two distinct morphologies (platelets and nanotiles), and W_5O_{14} ($WO_{2.8}$) and $W_{18}O_{49}$ ($WO_{2.72}$) nanowires.

2. Methods

2.1. Synthesis

All the materials were synthesized via chemical vapour transport reaction in a two-zone furnace, using iodine as the transport agent. The synthesis protocols are described in detail in [29, 35–37].

2.2. Electron microscopy

Scanning electron microscopy (SEM) was performed on Supra 35 VP (Carl Zeiss, Germany). High-resolution transmission electron microscopy (HRTEM) and electron diffraction (ED) images were obtained by a Cs probe-corrected TEM/STEM JEOL ARM 200CF microscope equipped with a cold-FEG electron source, operating at 200 kV. Cross-sections of the samples for TEM analysis were obtained using a Helios NanoLab 650 Focused Ion Beam-scanning electron microscope (FIB).

2.3. Photoluminescence

The solutions for the optical measurements were prepared using purified water (extinction) or ethanol (photoluminescence and Raman spectroscopy).

Photoluminescence spectra were measured using an optical spectrometer (PTI QuantaMaster 8000 by Horiba) with a continuous Xe lamp and a photomultiplier sensitive in visible and near-infrared part of the spectrum (Hamamatsu R2658). Holographic reflection gratings blazed at 300 nm were used in the dual-stage excitation monochromator, and ruled gratings (500 nm blaze) in the single-stage emission monochromator. The spectra were measured in the wavelength range of 290–450 nm (corresponding to 3.1–4.3 eV) at nominal resolution of 3 nm, with the excitation spectral band centered at 275 nm (4.51 eV). All presented spectra were corrected for spectral dependence of the instrument's excitation and emission channels.

2.4. Extinction measurements

Extinction measurements were performed with an UV–vis spectrometer (Perkin-Elmer lambda 950). The spectra were recorded with a 1 nm resolution. The solution was hand-shaken and the suspensions were measured using quartz cuvettes.

2.5. Raman scattering

The Raman scattering measurements were performed using a Tri Vista 557 Raman system in backscattering micro-Raman configuration. The 532 nm line of VerdiG solid-state (for platelets) and the 514.5 nm line of Ar^+/Kr^+ ion gas laser (for nanotiles and nanowires) were used as an excitation source. A microscope objective with ×100 magnification was used for focusing the laser beam and collecting scattered light. Laser power was kept below 0.5 mW at the sample surface, in order to minimize local heating. Spectra were recorded in parallel and crossed polarisation configuration. All measurements were performed in air, at room temperature. Spectra were corrected for the Bose factor.

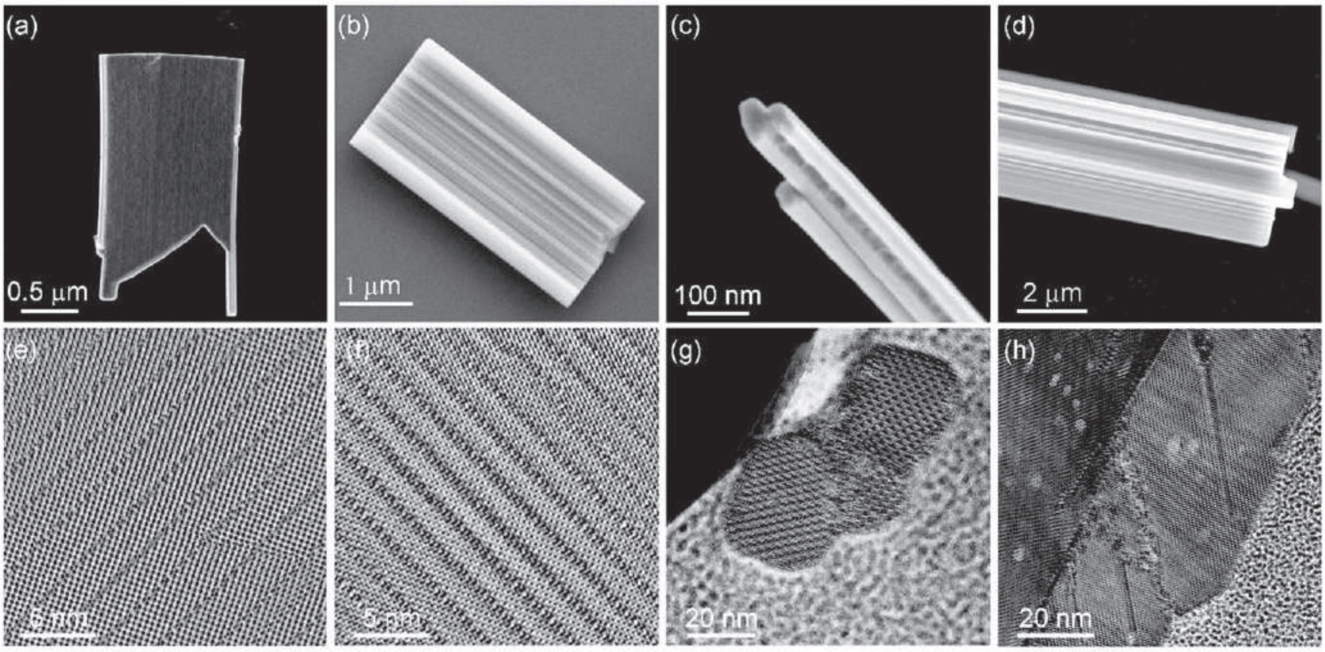

Figure 1. Electron microscopy images of (a), (e) platelets, (b), (f) nanotiles, (c), (g) W_5O_{14} NW and (d), (h) $W_{18}O_{49}$ NW. Top panel corresponds to SEM, while the bottom panel corresponds to TEM images.

Table 1. Stoichiometry of tungsten suboxide nanomaterials, their shape, thickness and lateral size (for 2D $W_nO_{3n\text{-}1}$) or *-diameter and length (for nanowires), and the assessed work function.

Stoichiometry	Shape	Thickness/diameter*	Lateral size/length*	Work function (eV)
$W_nO_{3n\text{-}1}$	Platelets	100 nm	Up to 4 μm	4.18–4.31
$W_nO_{3n\text{-}1}$	Nanotiles	100 nm	Up to several μm	4.94–5.30
W_5O_{14} ($WO_{2.8}$)	Nanowires	100–200 nm	Several tens μm	4.20–4.34
$W_{18}O_{49}$ ($WO_{2.72}$)	Nanowires	Up to 3 μm	Several tens μm	4.55–4.57

2.6. Kelvin probe force microscopy

The work function (WF) was measured with the Kelvin probe force microscopy (KPFM) method using a non-contact frequency-modulated atomic force microscope (NC-AFM, Omicron VT-AFM, Taunusstein, Germany) operating in ultra-high vacuum (10^{-9} mbar). The samples were dispersed in isopropanol and drop casted on a freshly cleaved highly oriented pyrolytic graphite (HOPG) substrate. The AFM and the KPFM images were taken simultaneously on the same area. KPFM was used to determine the WF of the samples by measuring the contact potential difference (CPD) between the substrate (HOPG) and the samples. As HOPG has a fairly stable WF value of 4.60 eV [38], it is commonly used as a reference material in KPFM measurements.

3. Results and discussion

3.1. Composition and morphology

The studied WO_{3-x} phases grow as thin plate-like crystals (platelets, nanotiles) or as nanowires (W_5O_{14}, $W_{18}O_{49}$). Figure 1 shows SEM and TEM images of the $W_nO_{3n\text{-}1}$ platelets (a), (e) and nanotiles (b), (f); W_5O_{14} nanowires (c), (g), and $W_{18}O_{49}$ nanowires (d), (h). The stoichiometry and size of all four studied WO_{3-x} phases is summarized in table 1.

The $W_nO_{3n\text{-}1}$ platelets grow epitaxially from $W_{19}O_{55}$ nanowires. These nanowires can either get detached from the platelets by mild sonication, or remain at the long edge of the platelet, as seen in figure 1(a). The platelets grow in a rectangular geometry and are approximately 100 nm thick with the lateral size of up to 4 μm. Several $W_nO_{3n\text{-}1}$ Magnèli phases, such as $W_{18}O_{53}$ ($WO_{2.944}$), $W_{17}O_{50}$ ($WO_{2.941}$), $W_{16}O_{47}$ ($WO_{2.938}$), $W_{15}O_{44}$ ($WO_{2.933}$), $W_{14}O_{41}$ ($WO_{2.929}$), W_9O_{26} ($WO_{2.889}$) and $W_{10}O_{29}$ ($WO_{2.9}$), were found within a single platelet [36].

The nanotiles with the length and width up to a few μm are approximately 100 nm thick. They have characteristic surface corrugations that can be several tens of nm deep. They are multi-stoichiometric, with six distinct stoichiometries within a single nanotile: $W_{16}O_{47}$ ($WO_{2.938}$), $W_{15}O_{44}$ ($WO_{2.933}$), $W_{14}O_{41}$ ($WO_{2.928}$), $W_{13}O_{38}$ ($WO_{2.923}$), $W_{12}O_{35}$ ($WO_{2.917}$), and $W_{11}O_{32}$ ($WO_{2.909}$), all having the same $W_nO_{3n\text{-}1}$ formula [37]. In both plate-like morphologies (i.e. nanotiles and platelets), CS planes are observed, as shown in

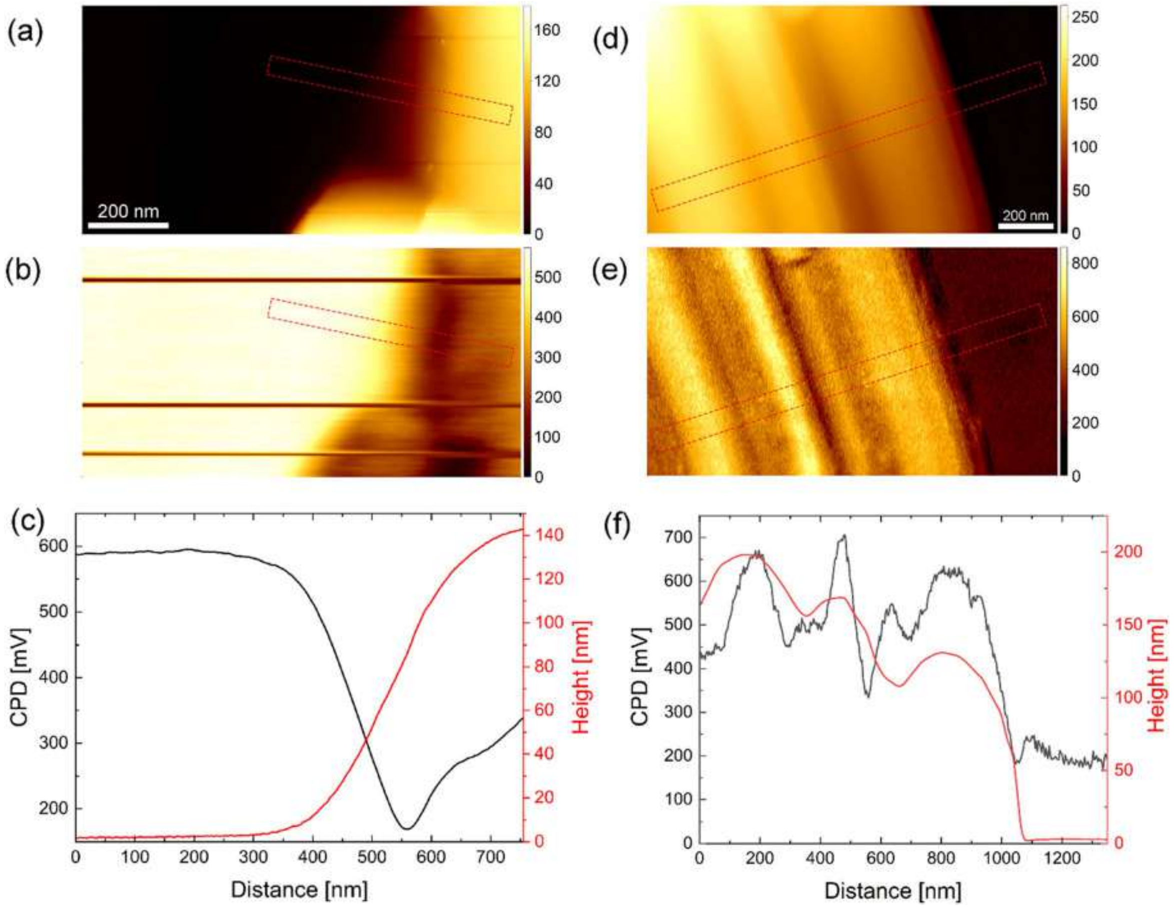

Figure 2. AFM (a), (d) and KPFM images (b), (e) of platelets and nanotiles, respectively. The CPD profiles and the matching thickness (c), (f) correspond to the areas marked with dashed rectangles.

figures 1(e), (f). The distance between the CS planes reflects the stoichiometry of a particular block.

Both W_5O_{14} and $W_{18}O_{49}$ nanowires have constant diameters along the lengths of several tens of μm. The W_5O_{14} NWs are thinner, with the mean diameter of 100–200 nm, while $W_{18}O_{49}$ NWs have significantly larger diameters of up to 3 μm, with rarely observed thin ones [35]. The cross-sectional views of such nanowires (figures 1(g), (h)) reveal that they are composed of several single-crystalline units.

3.2. Work function

The WF was measured on an individual WO_{3-x} nanotile or platelet. The results are compared with the previously published data obtained on the W_5O_{14} and $W_{18}O_{49}$ nanowires [35]. The topography and Kelvin images are shown in figure 2.

The platelet shown in figure 2(a) is around 140 nm thick. The CPD measured on the platelets was between 290 and 420 mV lower than on HOPG, corresponding to a WF of 4.18–4.31 eV. Very similar WF values were reported earlier for W_5O_{14} nanowires (4.20–4.34 eV) [35]. On the other hand, the CPD obtained on the nanotiles was between 340 and 700 mV higher than on HOPG, indicating a WF of 4.94–5.30 eV. The WF of the nanotiles is thus substantially higher compared to both W_5O_{14} and $W_{18}O_{49}$ nanowires (4.55–4.57 eV) [35].

The KPFM and AFM images also reveal that the WF is morphology dependent. In the case of platelets, the WF is slightly lower at the edge (figure 2(c)), similar to measurements performed on the edges of W_5O_{14} nanowires [35]. This might be due to the growth mechanism, as the platelets grow from nanowires [36], or due to band bending [39]. The WF of nanotiles also varies with location and was found to be lower inside the corrugations (figure 2(f)). The difference between the CPD at top and the bottom of the corrugation can be up to 350 meV. The summarized positions of WF values are presented in table 2.

3.3. Optical properties

3.3.1. Raman spectroscopy. Raman spectra of WO_{3-x} nanomaterials can be tentatively divided into three regions, characterized by the peaks originating from different types of vibrations. Lattice modes generally appear below 200 cm^{-1}, W–O–W bending modes between approximately 200 and 400 cm^{-1}, whereas between 600 and 900 cm^{-1} one can observe W–O stretching modes [40, 41]. Figure 3 represents room temperature Raman spectra of WO_{3-x} nanostructures measured in three polarization

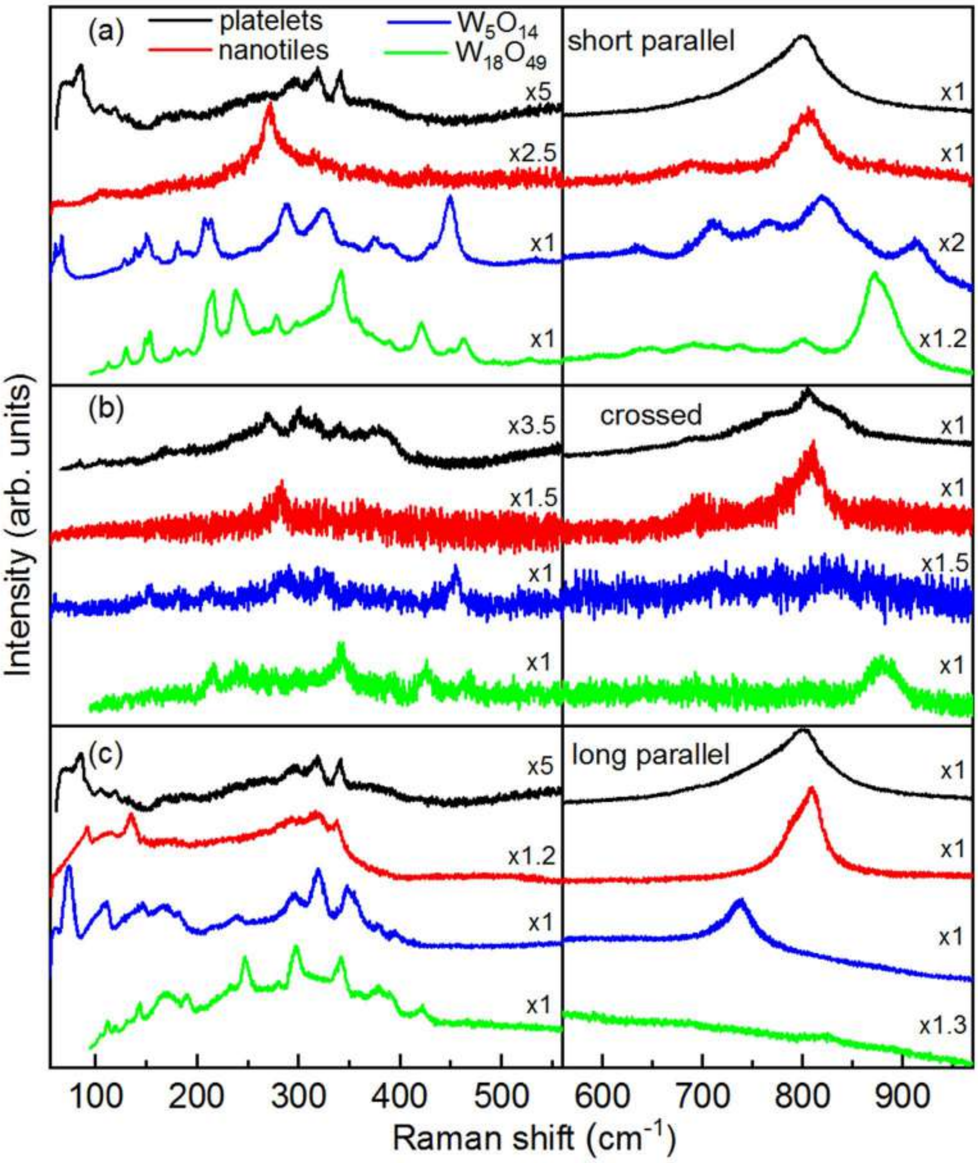

Figure 3. Raman scattering spectra of WO_{3-x} nanostructures measured at room temperature in three polarization configurations: (a) parallel, with incident and scattered light polarized along the short axis of the samples (short parallel configuration), (b) crossed, and (c) parallel, with incident and scattered light polarized along the long axis of the samples (long parallel configuration). For clarity, lower and higher-energy ranges are displayed with different scale factors.

Table 2. Summary of the assessed absorption and PL transitions, bandgap and work function values in tungsten suboxide nanomaterials.

	W_nO_{3n-1} platelets	W_nO_{3n-1} nanotiles	W_5O_{14} ($WO_{2.8}$)	$W_{18}O_{49}$ ($WO_{2.72}$)
UV–vis (nm)	207, 222, 241, 281, 323	205, 216, 240, 281, 324, 416	200, 223, 258, 326, 760	198, 208, 296, 776
PL (nm)	299, 323	302, 316	298, 324	299, 319
Bandgap (direct) (eV (nm))	4.11 (301)	4.05 (306)		
Bandgap (indirect) (eV (nm))	3.76 (330), 3.17 (391)	3.48 (356), 2.78 (446)	2.16 (574)	2.62 (473)
WF (eV)	4.18–4.31	4.94–5.30	4.20–4.34	4.55– 4.57
Average WF (eV)	4.25	5.12	4.27	4.56

configurations: short and long parallel, with incident and scattered light polarized along short and long axis of the sample respectively; and crossed, with polarisations parallel to the short and long axis of the sample but mutually orthogonal. In the case of the platelets, short and long parallel configurations are equivalent due to their symmetry.

Therefore, only two spectra were sufficient to observe all prominent modes noted in [36].

In platelets' crossed polarization configuration spectrum, there are four weak peaks, at 85, 105, 130 and 165 cm^{-1} related to lattice vibration, six peaks centred at 235, 271, 300, 319, 340 and 380 cm^{-1}, originating from W–O–W bending vibrations and one weak (690 cm^{-1}) and two strong (778 and 808 cm^{-1}) W–O stretching vibrations. In parallel configuration, one can observe few relatively weak peaks, at 85, 105, 120, 130, 297, 319 and 340 cm^{-1}, and two sharp overlapped peaks at 778 and 802 cm^{-1}. These results are in very good agreement with those from [36].

In the case of the nanotiles' short parallel polarization spectrum, only one weak peak (105 cm^{-1}) originating from lattice vibration, one strong peak at 271 cm^{-1}, a few weak peaks (at 231, 317, 331, 365 and 428 cm^{-1}) in the W–O–W bending region, and two prominent W–O stretching vibrations centred at 697 and 807 cm^{-1} are observed. In the crossed scattering configuration one can recognize the three highest intensity modes from that were also observed in the short parallel polarization (at 271, 697 and 807 cm^{-1}), whereas spectrum in long parallel polarization contains sharper and more pronounced low energy peaks, indicating good crystallinity and well-defined W–O bond length. Closer inspection revealed eight peaks, at 92, 113, 135, 175, 294, 319, 338 and 807 cm^{-1}, with the two prominent ones at 135 and 807 cm^{-1}, coinciding with the results given in [37].

Raman spectra of nanowires are qualitatively different from those of quasi-2D materials. Namely, for W_5O_{14} NW, in short parallel polarization seven lattice (at 67, 129, 139, 151, 181, 208 and 214 cm^{-1}), six W–O–W bending (at 288, 325, 376, 391, 430 and 448 cm^{-1}) and five W–O stretching vibrations, centred around 635, 712, 767, 819 and 912 cm$^{-1,}$ were observed. Crossed polarization revealed Raman peaks at 151, 181, 208, 288, 325, 448 and 712 cm^{-1}, whereas in long parallel polarization one can observe peaks at 73, 108, 147, 167, 181, 237, 297, 319, 350, 376, 394 and 737 cm^{-1}.

In the short parallel polarization, the $W_{18}O_{49}$ NW spectrum hosts a large number of peaks, at 113, 129, 149, 153, 178, 190, 211, 215, 238, 245, 278, 341, 358, 390, 422, 449, 463, 527, 644, 689, 737, 801, 871 and 882 cm^{-1}, some of which are overlapping. In crossed polarization configuration there are only a few peaks, centred at 211, 215, 238, 245, 341, 422, 463, 871 and 882 cm^{-1}, whereas the spectrum in the long parallel polarization contains modes at 113, 119, 131, 142, 168, 190, 232, 247, 280, 297, 341, 378, 390, 422 and 821 cm^{-1}. The peak positions of all four materials are summarized in tables S1–4 (available online at stacks.iop.org/NANO/33/275705/mmedia).

Unlike the spectra of the nanotiles and platelets, where the W–O stretching modes centred around 800 cm^{-1} are absolutely dominant, Raman spectra of the nanowires contain a large number of sharp peaks in the first two frequency regions, which are comparable or even more dominant than the ones from the stretching vibrations region. This indicates that 2D materials contain a higher number of W–O bonds with well-defined lengths, whereas W_5O_{14} and $W_{18}O_{49}$ nanowires have better crystallinity and higher number of W–O–W bonds with well-defined bond angles. The fact that spectra of all the analysed materials strongly depend on the sample orientation and light polarization unequivocally confirms their anisotropic structure.

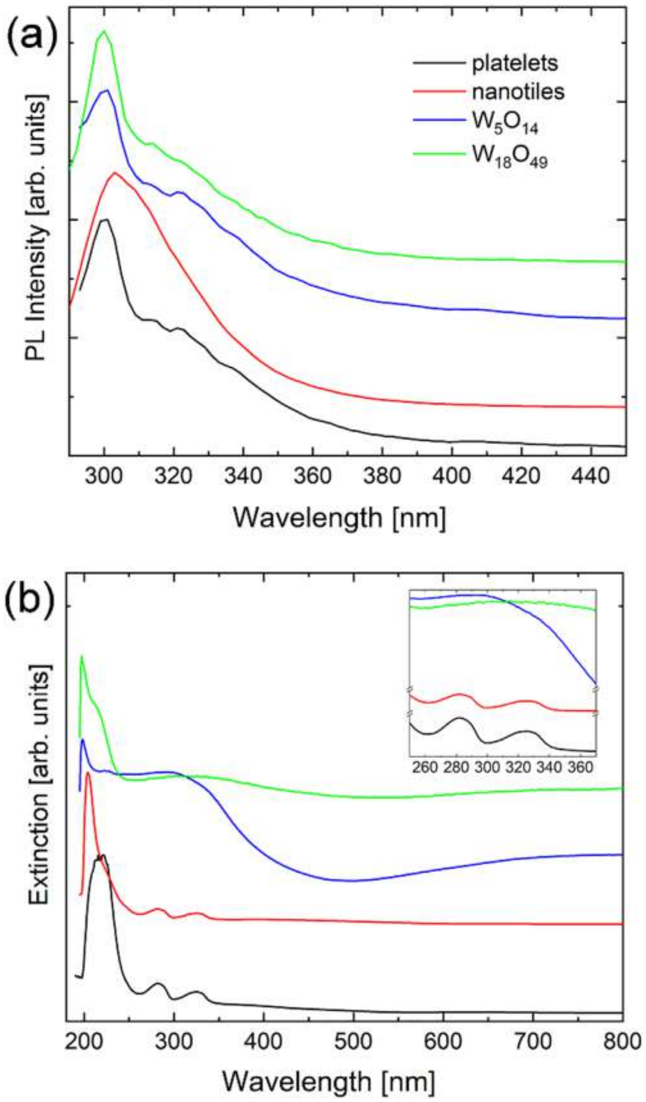

Figure 4. (a) Room temperature PL spectra and (b) UV–vis extinction spectra of platelets, nanotiles, W_5O_{14} and $W_{18}O_{49}$ nanowires.

3.3.2. Photoluminescence. In figure 4(a), the PL spectra of all four materials are presented, measured with the excitation centred at 275 nm (4.51 eV). The PL spectra were deconvolved, confirming that they contain two distinct emission lines in the UV region (figure S1). All of these suboxides have a dominant, high-energy peak situated around 300 nm (4.1 eV). An additional, red-shifted component appears in the 320 nm region (~3.9 eV), but its contribution varies. The positions of the PL peaks are summarized in table 2.

Because bulk WO_3 is an indirect band-gap semiconductor, its photoluminescence (PL) spectrum does not have any prominent features. In contrast, the appearance of new states in WO_{3-x} materials allows distinct optical transitions, often associated with PL emission lines. Many studies were reported on PL activity of the substoichiometric oxides [42–49], and, in general, correlated the electronic transitions to the defect states within the band gap, arising from oxygen vacancies. The two processes guiding these transitions were assigned either to the occurrence of localized states in the bandgap, stemming from oxygen vacancies or other defects; or to a band-to-band transition, arising from the electron–hole recombination induced by quantum confinement. However, there is no general consensus on interpretation of the observed emissions, as the experimental reports differ and do not unambiguously assign the observed emissions to the proposed mechanisms.

Theoretical models show that an oxygen vacancy can be in three new states, namely in a neutral (V_O^0), single- (V_O^+), or double-charged (V_O^{2+}) [25, 27, 34]. Within these models, the removal of an O atom from WO_3 structure (ReO_3-type, W^{6+}–O^{2-}–W^{6+}) results in creation of a V_O^0 state. This corresponds to creation of either a $W^{6+} + W^{4+}$ or $2W^{5+}$ defect states with levels inside or near the valence band (W^{4+}–V_O^0–W^{6+} or W^{5+}–V_O^0–W^{5+}) [25]. Removal of one additional electron, (i.e. conversion to V_O^+ (W^{5+})), leads to Coulombic repulsion between the positive vacancy and the nearest W-ion, displacing the ion and shifting the defect level into the bandgap (W^{5+}–V_O^+–W^{6+}). Removal of another electron creates a new state within the CB (W^{6+}–V_O^{2+}–W^{6+}). Therefore, the neutral state lies inside the valence band (VB), single-charged in the band gap, and the double-charged state inside the conduction band (CB). In other words, the W^{5+} states are shallow and can act as donor states, while electrons trapped in deeper states (W^{4+}) would need more energy to get excited into the CB. It is also important to note that the bandgap is closely related to the W–O bond length. When an O vacancy is introduced, structural relaxation of the lattice leads to an increase of the W–W distance. As the W ion gets displaced from the center of the WO_6 octahedron, the VB lowers and the CB rises, thus increasing the bandgap [50].

For PL spectra reported for $W_{18}O_{49}$ nanowires and nanorods, peaks appear in UV and blue spectral regions [31, 43, 45, 51]. For the nanorods, the peak located in the UV region blueshifts from 350 to 320 nm as the nanorod diameter decreases. This effect is assigned to quantum confinement, since the stoichiometry remains the same. The blue peak is situated around the absorption edge at 430 nm and does not show any size dependence, therefore it was assigned to the defect states within the bandgap [31].

Previously reported XPS measurements on these materials can provide more insight into origin of the transitions [29, 36, 37]. The valence band spectrum of the platelets indicates a semiconducting behaviour with a negligible density of states at the Fermi energy. On the other hand, the valence band spectrum of the nanotiles revealed a slightly metallic behaviour at room temperature due to a partial overlapping of a broad O 2p peak with W 5d orbitals [36, 37]. The W spectra confirm the presence of 5+ and 6+ oxidation states in both nanotiles and platelets. For the nanotiles, 6+ states represent 84% of the total W 4f, with the remaining 16% assigned to 5+, giving the average oxidation number of 5.84 and $3 - x$ value of 2.92. Similarly, the platelets spectrum is comprised of 81% of 6 + and 19% of 5+, with the oxidation number of 5.81 and $3 - x$ value of 2.91. These values are in great agreement with the stoichiometry deduced from the composition [36, 37]. Since the XPS measurements mainly correspond to the surface layers, these results confirm that the samples have no surface contaminations and that the additional defects do not accumulate at the surface layers. Similarly, 5+ and 6+ states have been observed for W_5O_{14} NW [29], while for the $W_{18}O_{49}$ NW, an additional 4+ state can appear [52, 53].

Focusing on the O 1s spectrum of nanotiles, platelets and W_5O_{14} NW, it can be observed that the peak at 533.5 eV is the most prominent for the platelets, the intensity decreases for NW while it is completely absent for the nanotiles. The WF values were increasing in the same order. This peak, together with the one at 532.0 eV, is attributed to O binding with W in lower oxidation states. HRTEM images shown in figure S3 reveal that the CS planes in the platelets appear parallel to the basal plane, which is still within the depth sensitivity of the XPS. On the other hand, the CS planes in the nanotiles are not close to the surface and are terminated in an unordered fashion, with the regular WO_3 dominating the surface. The effect of the oxidation state of the surface W can be of a great influence on the optical properties of these materials. Therefore, we can attribute the two observed emission bands in the UV to two electron–hole recombination processes, whereby the hole comes from the VB, while the electrons come from two resonant states within the CB, i.e. from two V_O^{2+} states [25, 48].

3.3.3. Extinction. As previously mentioned, both theoretical and experimental studies correlated oxygen vacancies and/or substoichiometric crystal structure to the appearance of defect states [27, 54, 55]. It was reported that up to $x = 0.1$, the optical and electrical properties of bulk WO_{3-x} are governed primarily by localized electrons involved in polarons [26]. The insulator-metal transition begins at $x = 0.1$, as the polaron wave functions start to overlap and form delocalized states [56]. As the x increases, free electrons start to dominate optical processes. In general, the indirect bandgap corresponds to the electronic transition from the filled O 2p orbitals at the top of the valence band to the empty W 5d orbitals in the conduction band [57]. Therefore, the absorption spectrum of WO_3 is essentially featureless until the photon energy reaches the bandgap value. Near the UV region, interband transitions start to take place and govern the optical properties [57].

Extinction (UV–vis) measurements, which include contributions of both absorbance and scattering processes, were performed on all four materials and the spectra are presented in figure 4(b). Although the samples were diluted in order to avoid the multi-scattering regime, the scattering effects in the near UV region cannot be completely excluded. The deconvolution of all the spectra has been performed and the positions of the individual peak contributions extracted, as shown in figure S2.

The most prominent transitions appear in the UVC range, with two contributions centred at 207 and 222 nm for the platelets and at 205 and 216 nm for the nanotiles, with another peak situated at 240 nm for both. Additionally, there are two prominent and closely positioned peaks, situated at 281 and 324 nm. These peaks may originate from exitonic transitions, as described later. A wide and less intense peak is also observed at 359 nm and 416 nm for the platelets and nanotiles, respectively. For both materials, the scattering is accounted for with a model function, as described in the SI.

On the other hand, the spectra of nanowires are significantly different compared to the quasi-2D materials. Both types of NWs have a high-energy peak around 200 nm. For $W_{18}O_{49}$ NWs, this peak can be deconvolved into two peaks positioned at 198 and 208 nm. $W_{18}O_{49}$ NWs spectrum has a higher-energy peak centred at 296 nm, ending with a broad transition at 776 nm. In addition to the peak at 200 nm, W_5O_{14} NWs have a very weak peak at 223 nm and an additional broad peak at approximately 300 nm, which can be deconvoluted into two peaks situated at 258 and 326 nm. An even broader peak appears at 760 nm in the near-IR part of the spectrum. The emergence of the near-IR peaks can be associated with LSPR due to free charge carriers. LSPR were observed previously in $W_{24}O_{68}$ ($WO_{2.83}$) and $W_{19}O_{55}$ ($WO_{2.89}$) nanorods, positioned at 900 nm and 600 nm, respectively [26, 55]. Assigning the near-IR tails to LSPR is also in agreement with earlier measurements on these NWs, which suggested metallic behaviour [29, 35].

Extinction spectra of these suboxides vary substantially in the literature, even within the same stoichiometry or morphology. For example, ultrathin (sub-nanometre) $W_{18}O_{49}$ ($WO_{2.72}$) nanowires show a large absorption tail in the visible part of the spectrum, which saturates upon oxidation [32, 51]. This effect points to the presence of a large number of oxygen vacancies or substoichiometric crystal structures. For the nanowires with larger diameter, the absorption in the visible and near-IR range drops. Nanorod bundles of the same stoichiometry have rather featureless spectra, with a steady decrease with increasing wavelength [31]. In the case of $W_{19}O_{55}$ ($WO_{2.89}$) nanorods, the extinction spectrum in UV–vis consists of one broad peak situated at 600 nm (2.07 eV) and a strong absorption band at 200–400 nm, similar to that seen in bulk WO_3 [55]. On the other hand, $W_{24}O_{68}$ ($WO_{2.83}$) nanorods support strong LSPRs, as evidenced by a broad peak centred around 900 nm [26]. WO_{3-x} reduced cubic nanosheets have a narrow peak around 220 nm, with a broader one centred around 300 nm [58]. The strong absorption in the long wavelength region is attributed to the new, oxygen vacancies-induced levels below the conduction band.

Qualitatively, the line shapes of the nanotiles and platelets spectra are similar to those of $WO_{2.9}$ ($W_{20}O_{58}$) nanoparticles [54] and WO_{3-x} quantum dots [59]. For the $WO_{2.9}$ NPs, the UV–vis spectrum consists of two shoulders at 220 and 265 nm, and a band at 320 nm with the bandgap estimated at 3.1 eV (400 nm). These NPs are also stoichiometrically the closest to platelets and nanotiles. Quantum dots have a high-intensity high-energy peak followed by broader bands around 230 and 285 nm. Therefore, the two peaks found in the nanotiles and platelets and positioned at 281 and 323 nm are most likely a consequence of the crystal structure, i.e. the CS planes.

From the measured extinction spectra, direct and indirect optical bandgaps can be calculated using the equation [60]:

$$\alpha = \frac{\mathbf{A(h\nu - E_g)^n}}{\mathbf{h\nu}},$$

Here, α is the absorption coefficient, A is a constant, and E_g is the indirect bandgap for $n = 1/2$ and direct bandgap in the case of $n = 2$. The corresponding Tauc plots are presented in figure S4.

The optical bandgaps are highly sensitive to morphology and stoichiometry. In the literature, the measured optical bandgaps of bulk WO_3, bulk $WO_{2.9}$ and $WO_{2.9}$ nanowires were reported at 2.67 eV, 3.05 eV and 3.17 eV, respectively [3, 32]. For $W_{18}O_{49}$ nanorod bundles, the absorption edge is situated at 2.95 eV [31]. The decrease of the bandgap value of these nanorods by approximately 0.5 eV compared to that of the WO_3 nanoparticles of similar size (3.44 eV) [61] is assigned to the presence of new states correlated to the oxygen vacancies. The appearance of these new states can lead to the rise of two indirect absorption edges, as reported for the suboxide nanosheets (at 2.6 eV and 1.11 eV) [58]. In general, the optical bandgap of these nanostructured suboxides is governed by several different processes. The quantum confinement results in the increase of the bandgap, i.e. the smaller the particle, the larger the bandgap. A similar effect can be assigned also to the Burstein–Moss shift [62]. Namely, in the case of n-type metal oxide semiconductors, an increase of dopants (i.e. oxygen vacancies and W^{5+} atoms) shifts the absorption edge to higher energies due to filling states. Consequently, the measured bandgap, as determined from the onset of interband absorption, moves to higher energies (i.e. undergoes a blue shift). On the other hand, in heavily doped semiconductors, bandgap renormalization takes place. As the electrons start interacting with defects and impurities, their energy shifts due to a variety of effects, such as exchange interaction or Coulombic repulsion [63]. Consequently, the bandgap shrinks with increasing doping level, explaining the decrease of the band-gap with the increase of x [64]. The complex interplay of all these effects makes the value of the bandgap difficult to predict.

For both the nanotiles and platelets, an increase of the indirect bandgap is observed. However, there is an opening of another, lower energy bandgap. This bandgap appears as a consequence of the altered electronic structure due to bond length changes caused by oxygen vacancies and formation of CS planes with W atoms in lower oxidation states. The appearance of two indirect absorption edges was previously reported in suboxide nanosheets [58]. The two indirect bandgaps appear at 3.76 and 3.17 eV for the platelets and at 3.48 and 2.78 eV for the nanotiles. The former value can be assigned to the regular bandgap (between the VB and the CB), while the latter appears between a new, defect-induced band and CB. The regular gap coincides with the transitions observed in the extinction spectra. These values lie in the upper range of the bandgaps reported in the literature, which is attributed to the distortions in the WO_6 octahedra in such sub-stoichiometric materials [12, 24].

Nanowires show the indirect bandgap values of 2.16 and 2.62 eV for W_5O_{14} and $W_{18}O_{49}$, respectively. As these materials show LSPR fingerprints and therefore free charge carriers, their bandgap decreased with respect to WO_3.

The calculated direct optical bandgap is 4.11 eV (302 nm) for the platelets and 4.05 eV (306 nm) for the nanotiles. These values are in good agreement with the dominant PL peaks that are situated at 4.15 eV and 4.11 eV for the platelets and nanotiles, respectively. As discussed previously, both recorded PL bands are in the UV region, in the 3.9–4.2 eV range and can be assigned to two resonant states introduced by oxygen vacancies [27, 47]. Namely, an electron–hole pair forms an exciton near the oxygen vacancy. When an electron is excited to a state at or above the resonance, it can be trapped. The emission bands in the UV are thus attributed to electron–hole recombination, where the electron comes from one of the two resonant levels in the CB, while the hole occupies the VB. Therefore, the direct bandgap stems from optical transitions related to the defect states. These transitions and the corresponding bandgaps are at the same positions for nanotiles and platelets, confirming their similar stoichiometry. The bang gap values and extinction peak positions are presented in table 2.

4. Conclusions

Structural and optical properties of four different WO_{3-x} nanostructures with different morphologies and/or stoichiometries are presented. While the two quasi-2D materials show polycrystallinity, nanowires are of uniform W_5O_{14} and $W_{18}O_{49}$ composition. Raman spectra reveal that less oxidized W_xO_{3x-1} stoichiometries have higher number of W–O bonds with well-defined lengths, whereas more reduced tungsten suboxides have a higher number of W–O–W bonds with well-defined bond angles. The extinction spectra reveal the appearance of excitonic states for the less oxidized W_xO_{3x-1} stoichiometries and two indirect bandgaps deduced from the Tauc plots. Both values appear in the upper range reported for suboxide materials, which can be explained by the formation of oxygen vacancies. The extinction spectra of the more reduced tungsten suboxides show the presence of LSPR in the near-IR region. Their bandgaps are lower, as they have a higher number of free charge carriers, confirmed by the LSPR-like peaks. PL spectra reveal two distinct emission peaks in the UV range, present in all four nanomaterials. They are attributed to electron–hole recombination, with the hole stemming from the VB and electron from one of the resonant states within the CB. Furthermore, the effects of stoichiometry and CS planes are discussed in relation to the understanding of the optical properties.

Acknowledgments

This work was financially supported by the Slovenian Research Agency through contracts P1-0099 and P1-0192. BV, MO, AM and NL acknowledge funding provided by the Institute of Physics Belgrade, through the grant by the Ministry of Education, Science, and Technological Development of the Republic of Serbia and Center for Solid State Physics and New Materials. Authors are grateful to Janez Jelenc (Jozef Stefan Institute) for KPFM measurements, and Lina Senica for technical assistance with the photoluminescence measurements.

Data availability statement

All data that support the findings of this study are included within the article (and any supplementary files).

ORCID iDs

Bojana Višić https://orcid.org/0000-0002-2065-0727
Luka Pirker https://orcid.org/0000-0003-0741-0048
Boris Majaron https://orcid.org/0000-0003-2841-8276
Maja Remškar https://orcid.org/0000-0002-8919-1768

References

[1] Mahjabin S *et al* 2021 Effects of oxygen concentration variation on the structural and optical properties of reactive sputtered WOx thin film *Sol. Energy* **222** 202–11
[2] Thummavichai K, Xia Y and Zhu Y 2017 Recent progress in chromogenic research of tungsten oxides towards energy-related applications *Prog. Mater Sci.* **88** 281–324
[3] Huang Z F, Song J, Pan L, Zhang X, Wang L and Zou J J 2015 Tungsten oxides for photocatalysis, electrochemistry, and phototherapy *Adv. Mater.* **27** 5309–27
[4] Pirker L and Višić B 2021 Recent progress in the synthesis and potential applications of two-dimensional tungsten (Sub) oxides *Isr. J. Chem.* (https://doi.org/10.1002/ijch.202100074)
[5] Zhang X, Wei Y and Yu R 2022 Multi-dimensional tungsten oxides for efficient solar energy conversion *Small Structures* **3** 2100130
[6] Liu J, Zhong M, Li J, Pan A and Zhu X 2015 Few-layer WO_3 nanosheets for high-performance UV-photodetectors *Mater. Lett.* **148** 184–7
[7] He Z, Liu Q, Hou H, Gao F, Tang B and Yang W 2015 Tailored electrospinning of WO_3 nanobelts as efficient ultraviolet photodetectors with photo-dark current ratios up to 1000 *ACS Appl. Mater. Interfaces* **7** 10878–85
[8] Aguir K, Lemire C and Lollman D 2002 Electrical properties of reactively sputtered WO_3 thin films as ozone gas sensor *Sensors Actuators* B **84** 1–5
[9] Zhang C *et al* 2011 Highly sensitive hydrogen sensors based on co-sputtered platinum-activated tungsten oxide films *Int. J. Hydrogen Energy* **36** 1107–14
[10] Hariharan V, Gnanavel B, Sathiyapriya R and Aroulmoji V 2019 A review on tungsten oxide (WO_3) and their derivatives for sensor applications *Int. J. Adv. Sci. Eng.* **5** 1163–8

[11] Sayama K, Mukasa K, Abe R, Abe Y and Arakawa H 2001 Stoichiometric water splitting into H2 and O2 using a mixture of two different photocatalysts and an IO3−/I− shuttle redox mediator under visible light irradiation *Chem. Commun.* **23** 2416–7

[12] Wang G, Ling Y and Li Y 2012 Oxygen-deficient metal oxide nanostructures for photoelectrochemical water oxidation and other applications *Nanoscale.* **4** 6682–91

[13] Miyazaki H, Ishigaki T and Ota T 2017 Photochromic smart windows employing WO_3-based composite films *J. Mater. Sci. Res.* **6** 62–6

[14] Hai Z, Wei Z, Xue C, Xu H and Verpoort F 2019 Nanostructured tungsten oxide thin film devices: from optoelectronics and ionics to iontronics *J. Mater. Chem.* C **7** 12968–90

[15] Granqvist C G 2000 Electrochromic tungsten oxide films: review of progress 1993–1998 *Sol. Energy Mater. Sol. Cells* **60** 201–62

[16] González-Borrero P *et al* 2010 Optical band-gap determination of nanostructured WO_3 film *Appl. Phys. Lett.* **96** 061909

[17] He T and Yao J 2007 Photochromic materials based on tungsten oxide *J. Mater. Chem.* **17** 4547–57

[18] Zheng H, Ou J Z, Strano M S, Kaner R B, Mitchell A and Kalantar-zadeh K 2011 Nanostructured tungsten oxide–properties, synthesis, and applications *Adv. Funct. Mater.* **21** 2175–96

[19] Polaczek A, Pekala M and Obuszko Z 1994 Magnetic susceptibility and thermoelectric power of tungsten intermediary oxides *J. Phys.:Condens. Matter* **6** 7909

[20] Tilley R 1970 The formation of shear structures in sub-stoichiometric tungsten trioxide *Mater. Res. Bull.* **5** 813–23

[21] Pickering R and Tilley R 1976 An electron microscope study of tungsten oxides in the composition range $WO_2.90 \cdot WO_2.72$ *J. Solid State Chem.* **16** 247–55

[22] Magnéli A 1953 Structures of the ReO_3-type with recurrent dislocations of atoms: homologous series' of molybdenum and tungsten oxides *Acta Crystallogr.* **6** 495–500

[23] Lundberg M, Sundberg M and Magnéli A 1982 The 'pentagonal column' as a building unit in crystal and defect structures of some groups of transition metal compounds *J. Solid State Chem.* **44** 32–40

[24] Mohamed A M, Amer A W, AlQaradawi S Y and Allam N K 2016 On the nature of defect states in tungstate nanoflake arrays as promising photoanodes in solar fuel cells *Phys. Chem. Chem. Phys.* **18** 22217–23

[25] Deb S K 2008 Opportunities and challenges in science and technology of WO_3 for electrochromic and related applications *Sol. Energy Mater. Sol. Cells* **92** 245–58

[26] Manthiram K and Alivisatos A P 2012 Tunable localized surface plasmon resonances in tungsten oxide nanocrystals *JACS* **134** 3995–8

[27] Karazhanov S Z, Zhang Y, Mascarenhas A, Deb S and Wang L-W 2003 Oxygen vacancy in cubic WO_3 studied by first-principles pseudopotential calculation *Solid State Ionics* **165** 43–9

[28] Migas D, Shaposhnikov V and Borisenko V 2010 Tungsten oxides. II. The metallic nature of Magnéli phases *J. Appl. Phys.* **108** 093714

[29] Remškar M, Kovac J, Viršek M, Mrak M, Jesih A and Seabaugh A 2007 W_5O_{14} nanowires *Adv. Funct. Mater.* **17** 1974–8

[30] Shi S, Xue X, Feng P, Liu Y, Zhao H and Wang T 2008 Low-temperature synthesis and electrical transport properties of $W_{18}O_{49}$ nanowires *J. Cryst. Growth* **310** 462–6

[31] Su C-Y and Lin H-C 2009 Direct route to tungsten oxide nanorod bundles: microstructures and electro-optical properties *J. Phys. Chem.* C **113** 4042–6

[32] Paik T *et al* 2018 Photocatalytic hydrogen evolution from substoichiometric colloidal WO_{3-x} nanowires *ACS Energy Lett.* **3** 1904–10

[33] Song K, Liu X, Tian C, Deng H, Wang J and Su X 2019 Oxygen defect-rich WO_{3-x} nanostructures with high photocatalytic activity for dehydration of isopropyl alcohol to propylene *Surf. Interfaces* **14** 245–50

[34] Wang F, Di Valentin C and Pacchioni G 2011 Semiconductor-to-metal transition in WO_{3-x}: nature of the oxygen vacancy *Phys. Rev.* B **84** 073103

[35] Saqib M *et al* 2020 Field emission properties of single crystalline W_5O_{14} and $W_{18}O_{49}$ nanowires *J. Electron. Spectrosc. Relat. Phenom.* **241** 146837

[36] Pirker L, Višić B, Škapin S D, Dražić G, Kovač J and Remškar M 2020 Multi-stoichiometric quasi-two-dimensional Wn O 3n− 1 tungsten oxides *Nanoscale.* **12** 15102–14

[37] Pirker L, Višić B, Kovač J, Škapin S D and Remškar M 2021 Synthesis and characterization of tungsten suboxide WnO3n − 1 nanotiles *Nanomaterials.* **11** 1985

[38] Maeda F, Takahashi T, Ohsawa H, Suzuki S and Suematsu H 1988 Unoccupied-electronic-band structure of graphite studied by angle-resolved secondary-electron emission and inverse photoemission *Phys. Rev.* B **37** 4482

[39] Lanzoni E M *et al* 2021 The impact of Kelvin probe force microscopy operation modes and environment on grain boundary band bending in perovskite and Cu (In, Ga) Se2 solar cells *Nano Energy* **88** 106270

[40] Daniel M, Desbat B, Lassegues J, Gerand B and Figlarz M 1987 Infrared and Raman study of WO_3 tungsten trioxides and WO_3, xH_2O tungsten trioxide tydrates *J. Solid State Chem.* **67** 235–47

[41] Hardcastle F D and Wachs I E 1995 Determination of the molecular structures of tungstates by Raman spectroscopy *J. Raman Spectrosc.* **26** 397–405

[42] Johansson M B, Zietz B, Niklasson G A and Österlund L 2014 Optical properties of nanocrystalline WO_3 and WO_{3-x} thin films prepared by DC magnetron sputtering *J. Appl. Phys.* **115** 213510

[43] Lee K, Seo W S and Park J T 2003 Synthesis and optical properties of colloidal tungsten oxide nanorods *JACS* **125** 3408–9

[44] Feng M *et al* 2005 Strong photoluminescence of nanostructured crystalline tungsten oxide thin films *Appl. Phys. Lett.* **86** 141901

[45] Hong K, Xie M, Hu R and Wu H 2007 Synthesizing tungsten oxide nanowires by a thermal evaporation method *Appl. Phys. Lett.* **90** 173121

[46] Wang J, Lee P S and Ma J 2009 Synthesis, growth mechanism and room-temperature blue luminescence emission of uniform WO_3 nanosheets with W as starting material *J. Cryst. Growth* **311** 316–9

[47] Luo J Y, Xu N S, Zhao F L, Deng S Z and Tao Y T 2011 Ultraviolet superfluorescence from oxygen vacancies in WO_{3-x} nanowires at room temperature *J. Appl. Phys.* **109** 024312

[48] Wang B, Zhong X, He C, Zhang B, Cvelbar U and Ostrikov K 2021 Nanostructure conversion and enhanced photoluminescence of vacancy engineered substoichiometric tungsten oxide nanomaterials *Mater. Chem. Phys.* **262** 124311

[49] Wang D *et al* 2013 High-performance gas sensing achieved by mesoporous tungsten oxide mesocrystals with increased oxygen vacancies *J. Mater. Chem.* A **1** 8653–7

[50] Walkingshaw A D, Spaldin N A and Artacho E 2004 Density-functional study of charge doping in WO_3 *Phys. Rev.* B **70** 165110

[51] Xi G *et al* 2012 Ultrathin W18O49 nanowires with diameters below 1 nm: synthesis, near-infrared absorption,

photoluminescence, and photochemical reduction of carbon dioxide *Angew. Chem. Int. Ed.* **51** 2395–9

[52] Guo C, Yin S, Dong Q and Sato T 2012 The near infrared absorption properties of $W_{18}O_{49}$ *RSC Adv.* **2** 5041–3

[53] Guo C, Yin S, Yan M, Kobayashi M, Kakihana M and Sato T 2012 Morphology-controlled synthesis of $W_{18}O_{49}$ nanostructures and their near-infrared absorption properties *Inorg. Chem.* **51** 4763–71

[54] Barreca F, Acacia N, Spadaro S, Curro G and Neri F 2011 Tungsten trioxide (WO_{3-x}) nanoparticles prepared by pulsed laser ablation in water *Mater. Chem. Phys.* **127** 197–202

[55] Qian J, Zhao Z, Shen Z, Zhang G, Peng Z and Fu X 2016 Oxide vacancies enhanced visible active photocatalytic W 19 O 55 NMRs via strong adsorption *RSC Adv.* **6** 8061–9

[56] Salje E and Güttler B 1984 Anderson transition and intermediate polaron formation in WO_{3-x} Transport properties and optical absorption *Philos. Mag.* B **50** 607–20

[57] Hjelm A, Granqvist C G and Wills J M 1996 Electronic structure and optical properties of WO_3, $LiWO_3$, $NaWO_3$, and HWO_3 *Phys. Rev.* B **54** 2436

[58] Fang Z *et al* 2017 Synthesis of reduced cubic phase WO_{3-x} nanosheet by direct reduction of $H_2WO_4 \cdot H_2O$ *Mater. Today Energy* **6** 146–53

[59] Wang Y *et al* 2017 Simultaneous synthesis of WO_{3-x} quantum dots and bundle-like nanowires using a one-pot template-free solvothermal strategy and their versatile applications *Small* **13** 1603689

[60] Pankove J I 1971 *Optical Processes in Semi-Conductors* (Mineola, NY: Dover Publications, Inc)

[61] He T *et al* 2002 Photochromism of WO_3 colloids combined with TiO_2 nanoparticles *J. Phys. Chem.* B **106** 12670–6

[62] Sarkar A, Ghosh S, Chaudhuri S and Pal A 1991 Studies on electron transport properties and the Burstein-Moss shift in indium-doped ZnO films *Thin Solid Films* **204** 255–64

[63] Walsh A, Da Silva J L and Wei S-H 2008 Origins of band-gap renormalization in degenerately doped semiconductors *Phys. Rev.* B **78** 075211

[64] Smith W, Zhang Z-Y and Zhao Y-P 2007 Structural and optical characterization of WO_3 nanorods/films prepared by oblique angle deposition *J. Vac. Sci. Technol.* B **25** 1875–81

Inorganic Chemistry

pubs.acs.org/IC

Article

Suppression of Superconductivity and Nematic Order in $Fe_{1-y}Se_{1-x}S_x$ ($0 \leq x \leq 1$; $y \leq 0.1$) Crystals by Anion Height Disorder

Aifeng Wang,* Ana Milosavljevic, A. M. Milinda Abeykoon, Valentin Ivanovski, Qianheng Du, Andreas Baum, Eli Stavitski, Yu Liu, Nenad Lazarevic, Klaus Attenkofer, Rudi Hackl, Zoran Popovic, and Cedomir Petrovic*

Cite This: *Inorg. Chem.* 2022, 61, 11036−11045

Read Online

ACCESS | Metrics & More | Article Recommendations | Supporting Information

Downloaded via NATL LBRY OF SERBIA on March 6, 2026 at 12:10:48 (UTC).
See https://pubs.acs.org/sharingguidelines for options on how to legitimately share published articles.

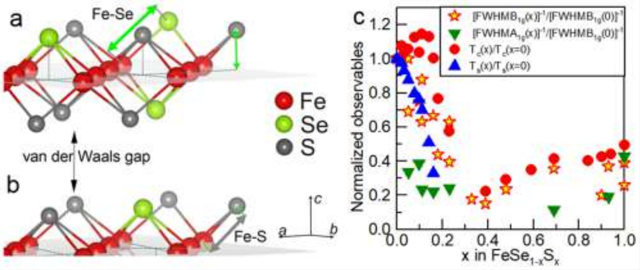

ABSTRACT: Connections between crystal chemistry and critical temperature T_c have been in the focus of superconductivity, one of the most widely studied phenomena in physics, chemistry, and materials science alike. In most Fe-based superconductors, materials chemistry and physics conspire so that T_c correlates with the average anion height above the Fe plane, i.e., with the geometry of the $FeAs_4$ or $FeCh_4$ (Ch = Te, Se, or S) tetrahedron. By synthesizing $Fe_{1-y}Se_{1-x}S_x$ ($0 \leq x \leq 1$; $y \leq 0.1$), we find that in alloyed crystals T_c is not correlated with the anion height like it is for most other Fe superconductors. Instead, changes in $T_c(x)$ and tetragonal-to-orthorhombic (nematic) transition $T_s(x)$ upon cooling are correlated with disorder in Fe vibrations in the direction orthogonal to Fe planes, along the crystallographic *c*-axis. The disorder stems from the random nature of S substitution, causing deformed $Fe(Se,S)_4$ tetrahedra with different Fe−Se and Fe−S bond distances. Our results provide evidence of T_c and T_s suppression by disorder in anion height. The connection to local crystal chemistry may be exploited in computational prediction of new superconducting materials with FeSe/S building blocks.

■ INTRODUCTION

The question of whether some specific crystal structure and bonding situation can facilitate superconducting pairing has intrigued chemists since shortly after the discovery of superconductivity.[1−10] Hence, the connection between the superconducting critical temperature (T_c) and aspects of the crystal structure is crucial yet poorly understood in all superconductors. This applies in particular for Fe- and Cu-based high-T_c superconductors; the former also feature an electronic nematic coupled with a structural orthorhombic transition (T_s) above T_c.[6−16] Fe superconductor materials crystallize in different space groups but share a common local structure feature, tetrahedrally coordinated Fe atoms.[6−12] One important empirical discovery for the future of materials design is that in most Fe-based superconductors the maximal T_c correlates with the average anion height above the Fe plane; the height depends on the geometry of the $FeAs_4$ or $FeCh_4$ (Ch = Te, Se, or S) tetrahedron.[7] The geometry also regulates the correlation strength due to average Fe−As(Ch) hybridization, pointing to a spin fluctuation mechanism of pairing that governs the magnitude of T_c.[7,12]

Interestingly, critical temperatures in FeSe conform to the anion height curve only at high pressures when T_s is fully suppressed.[7] A domelike magnetic phase supersedes the nematic order in the absence of chemical disorder in pressurized FeSe, and a T_c of 37 K is obtained at 6 GPa; in contrast, no magnetic order was found, and only small changes in T_c were detected when FeSe was subjected to the combined perturbation of chemical pressure and disorder for sulfur substitution of ≤20% at the Se atomic site.[17−19] An abrupt change in the superconducting gap structure points to two distinct pairing states as S substitutes for Se across the nematic critical point (NCP) around $x = 0.17$.[20−22] Substitution with sulfur in FeSe is expected to simply suppress electronic correlations associated with Fe d_{xy} orbitals.[23] Consequently, there should be a smooth change in T_c between FeSe (∼10 K) and FeS (∼5 K).[12]

However, due to the complex Fe−Se/S composition−temperature phase diagram and the unstable tetragonal phase that is difficult to synthesize, the clear connection of T_c and T_s with x and with crystal structure-related parameters in $FeSe_{1-x}S_x$ ($0 \leq x \leq 1$) is still unknown.[24−26] In contrast to the complex copper oxides or other Fe-based superconductors, the simpler crystal chemistry of binary iron chalcogenides might allow for deeper insight. To address this challenge, we

Received: February 18, 2022
Published: July 13, 2022

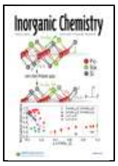

© 2022 American Chemical Society

https://doi.org/10.1021/acs.inorgchem.2c00568

present the entire progression of crystallographic changes as superconducting T_c evolves from FeSe to FeS. With the mixed S/Se occupancy of the anion atomic site, we observe Fe vacancy defects of $\lesssim$10%. We find that $T_c(x)$ is unrelated to the average anion height for a large portion of x, where T_c is found to be connected with the variation of the anion height induced by the fixed Fe−Se and Fe−S bonds and thereby induced disorder in Fe vibrations along the crystallographic c-axis, orthogonal to the Fe plane.

Our results show local deformations of $FeCh_4$ tetrahedra for most values of x in $Fe_{1-y}Se_{1-x}S_x$ $(0 \leq x \leq 1)$ crystals and provide evidence of T_c suppression related to disorder of Fe vibrations along the crystallographic c-axis. Because substantially higher superconducting T_c values can be induced in FeSe by an intercalating molecular spacer layer or by nanofabrication of ultrathin FeSe layers on $SrTiO_3$ substrates,[27−29] evidence of T_c suppression related to disorder in particular vibrations of atoms in the unit cell could be used to chemically tailor the critical temperature in not only intercalated FeSe crystals or few-layer samples but also novel superconductors with tetrahedral Fe−Ch or Fe−As building blocks in the unit cell.[10]

■ EXPERIMENTAL SECTION

Single crystals of $Fe_{1-y}Se_{1-x}S_x$ $(0 \leq x \leq 0.24)$ were grown using a eutectic mixture of KCl and $AlCl_3$ as the transport agent.[30] Namely, Fe, Se, S, KCl, and $AlCl_3$ powders were mixed together in a 1.1:(1 − x):x:1:2 Fe:Se:S:KCl:$AlCl_3$ ratio. After being ground in a mortar, the mixture was sealed in a quartz tube with a length of 12 cm and an inner diameter of 1.4 cm. Single crystals were grown in a horizontal tube furnace with a temperature gradient of 150 °C. Samples were very slowly heated to 420 °C in 2 weeks and kept for 2 months in the gradient. Shiny crystals with typical dimensions of 3 mm × 2 mm × 0.3 mm were picked up on the cool end. Single crystals of $Fe_{1-y}Se_{1-x}S_x$ $(0.39 \leq x \leq 1)$ were synthesized by deintercalation of potassium from the corresponding $K_{0.8}Fe_{2-y}(Se_{1-x}S_x)_2$ single crystals using the hydrothermal reaction method.[31,32] $K_{0.8}Fe_{2-y}(Se_{1-x}S_x)_2$ crystals were mixed with Fe powder, selenourea powder, and sulfourea pieces and weighted in a 1.1:(1 − x):x Fe:Se:S ratio, where the Se:S atomic ratio was identical to that of the crystals. Then, 5 mmol of the mixture, several pieces of $K_{0.8}Fe_{2-y}(Se_{1-x}S_x)_2$ single crystals, 2 mmol of Fe pieces, 0.1 g of NaOH, and 5 mL of deionized water were loaded into a 25 mL stainless steel autoclave with a Teflon liner. Additional Fe pieces were added to maintain the reducing atmosphere. The autoclave was tightly sealed, heated to 140 °C for 3 h, and kept at that temperature for 72 h in a small box furnace. Single crystals were obtained by rinsing the product using deionized water and alcohol and drying the sample overnight in a pumped vessel.

Element analysis was performed using energy-dispersive X-ray spectroscopy (EDX) in JEOL LSM-6500 and JEOL 7600F scanning electron microscopes with ∼2% accuracy.

Synchrotron powder XRD was measured on pulverized crystals using 74.69 keV (0.166 Å) synchrotron radiation of beamline 28-ID-1 of National Synchrotron Light Source 2 (NSLS 2). The sample−detector distance was 1216.272 mm. Rietveld analysis was carried out using the GSAS-II software package.[33] The X-ray absorption near-edge structure (XANES) and extended X-ray absorption fine structure (EXAFS) experiments were performed by mixing pulverized single crystals and BN powder uniformly and then pressing the mixture into pellets. The experiments were carried out at room temperature in the 8-ID beamline of NSLS 2 at Brookhaven National Laboratory (BNL) in transmission mode. Data were processed and analyzed using the ATHENA and ARTEMIS software programs.[34] The AUTOBK code was used to normalize the absorption coefficient and to separate the EXAFS signal, $\chi(k)$, from the atom absorption background. The extracted EXAFS signal, $\chi(k)$, was weighed by k^2 to emphasize the high-energy oscillation and then Fourier-transformed in a k range from 2 to 5 $Å^{-1}$ to analyze the data in the R space.

The investigation of the Mössbauer effect in the powdered samples, tetragonal $Fe_{0.9}Se_{0.82}S_{0.18}$ and tetragonal $FeSe_{0.31}Se_{0.69}$, was performed in transmission geometry using a $^{57}Co(Rh)$ source at room temperature. The spectrometer was calibrated with the spectrum of a natural iron foil. The spectra were recorded for samples in the low- and in high-velocity range. All Mössbauer spectra have been examined by the WinNormos-Site software package based on the least-squares method.[35] The measured isomer shift values (δ) are given relative to metallic α-iron (δ = 0).

Electrical transport was measured in a Quantum Design PPMS-9 instrument using a standard four-probe configuration with current flowing in the tetragonal plane. Magnetization was measured using a Quantum Design MPMS-XL5 instrument. Sample dimensions were measured with a model SMZ-800 Nikon optical microscope with 10 μm resolution. The dimensions were measured several times and then averaged. The standard deviation was <2%.

Raman experiments were performed using an excitation source solid state laser emitting at 532 nm. In our scattering configuration, the plane of incidence is the $a-b$ plane, with incident (scattered) light propagation along the c-axes. Right before being placed in vacuum, samples were cleaved in air. All measurements were performed in high vacuum (10^{-6} mbar) using a KONTI CryoVac continuous helium flow cryostat with a 0.5 mm thick window. The laser beam was focused using a microscope objective with 50× magnification. All spectra were corrected for the Bose factor. Experiments were performed using different crystals in two different institutions: Walther Meisner Institute (WMI) and Insititute of Physics Belgrade (IPB).

■ RESULTS

Synchrotron X-ray powder diffraction patterns (Figure 1a) confirm the phase purity of $Fe_{1-y}Se_{1-x}S_x$ for all investigated crystals in the range $0 \leq x \leq 1$. Typical Rietveld refinement of the average unit cell is shown in Figure 1b for the example of $Fe_{0.93}Se_{0.89}S_{0.11}$. Details of refinement are given in the Supporting Information.[36] The evolution of the unit cell parameters with substitution of S at the Se atomic site, inferred from the Rietveld refinement of the average crystal structure (Figure 2a), shows that both a and c decrease monotonically as the level of S is increased. However, a and c evolve at a different rates at low S substitution levels, in contrast to the same rate at the higher level. This change manifests itself as a clear kink in the c/a ratio (Figure 2b) near x = 0.25(5). The simultaneous decrease in the c/a ratio and the suppression of the resistivity hump with an increase in x (Figures 2c,d) suggest that the average crystal structure becomes more three-dimensional as x is increased. The decrease in the c/a ratio is stronger in the S-substituted crystals than in pure FeSe under high pressure where the crystal structure of the superconducting phase having a maximal T_c at 37 K changes, and magnetic order is observed up to 40 GPa.[17,18]

The resistivity anomaly associated with the structural transition at T_s in FeSe is suppressed to a lower temperature by S (Figure 2c,d), approaching 0 K above x = 0.18.[20] T_c increases slightly with S substitution from 9.3 K in FeSe to 10.9 K around x = 0.1, in agreement with previous observation,[37] whereas the transition width becomes broader and T_c decreases quickly with further S substitution, reaching a minimum value of 2.1 K at x = 0.4 (Figure 2c,d). With an even higher level of sulfur substitution, T_c increases slowly to 4.6 K for x = 1 (Figure 2d). The T_c values are consistent with those inferred from magnetic susceptibility, whereas values of ρ(300 K) are listed in Table S1.[36]

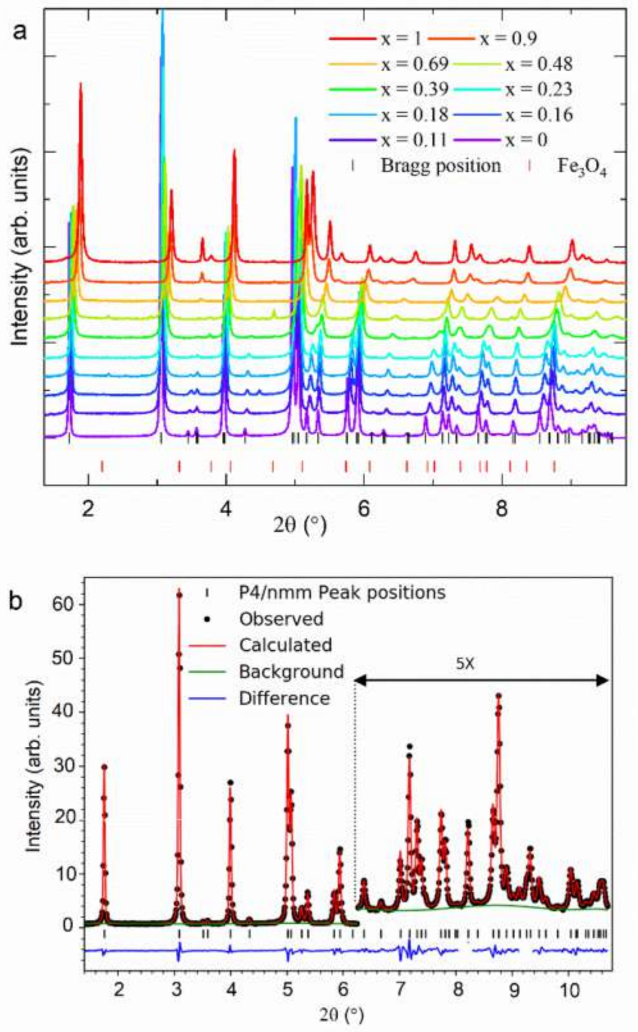

Figure 1. Average crystal structure from synchrotron powder XRD patterns. (a) Powder XRD patterns of $Fe_{1-y}Se_{1-x}S_x$ ($0 \leq x \leq 1$; $y \leq 0.1$). The top vertical tick marks represent FeSe Bragg reflections in the *P*4/*nmm* space group, whereas the bottom vertical tick marks show reflections of Fe_3O_4. The small Fe_3O_4 peaks visible for some values of *x* are due to oxidation during pulverization of air-sensitive crystals for 1 mm polyamide capillary loading. (b) Example of the Rietveld refinement of the background-subtracted data for $Fe_{0.93}Se_{0.89}S_{0.11}$.

In Fe-based superconductors, the highest T_c values are observed for regular Fe-Ch tetrahedra in which all bond angles approach 109.5°, empirically scaling with the average height of Ch(As) above the Fe plane.[7] We plot the average anion height from Rietveld refinement in Figure 2e, along with the evolution of T_c and T_s with *x*. The T_c values for FeSe and FeS in the absence of chemical substitutions scale with the change in the average anion height in the phase diagram. However, T_c values for FeSe, FeS, and any of the Se/S single-crystal alloys are not on the curve that connects the anion height above the Fe plane with the critical temperature in Fe-based superconductors; one should expect a T_c of ∼20 K for both compounds because the heights of Se and S atoms from the Fe atomic plane are 1.477(1) and 1.297(1) Å for FeSe and FeS, respectively. On the contrary, due to the smaller atomic radius of the sulfur atom, it is expected that S substitution in FeSe will induce a chemical pressure effect. Next, we will discuss differences in the effects of pressure [$T_c(P)$], S substitution [$T_c(x)$], and the small amount of disorder introduced by variations of $KCl/AlCl_3$ synthesis conditions[38] on T_c.

The evolution of the lattice parameters (Figure 2a) is different from the observed changes in the crystal structure of FeSe under applied pressure *P*. At high pressures, $2c/(a + b)$ decreases smoothly up to 4 GPa and then increases up to 9 GPa where the tetragonal crystal structure transforms into hexagonal FeSe.[39] When the applied pressure and chemical pressure in the FeSe phase diagram are scaled by the structural transition temperature (10 GPa for full S occupancy), $T_c(x)$ and $T_c(P)$ agree reasonably well with each other (Figure 3a) up to approximately the NCP.[18] Beyond the NCP, there is a local minimum of $T_c(P)$ at ∼1.5 GPa and magnetic order appears with the increase in T_c to 30 K, whereas T_c in $Fe_{1-y}Se_{1-x}S_x$ decreases to a minimum at $x = 0.4$ and increases with further S substitution. Thus, S provides mainly chemical pressure effects for *x* values below the NCP. This is also evident from the size of the *a* lattice parameter (Figure 2a) that decreases by $x = 0.16$ to ∼3.75 Å, consistent with pressurized FeSe.[17] It is instructive to stay focused on the nematic region and to compare $T_c(T_s)$ induced by S substitution, pressure, and disorder (Figure 3b).[18,38,40] The $T_c(T_s)$ values in $Fe_{1-y}Se_{1-x}S_x$ and pressurized FeSe have similar domelike behavior with the highest T_c at $T_s \sim 60$ K; in contrast, T_c decreases quickly with the suppression of T_s in FeSe disordered by small variations in the synthesis conditions. We also note that, even though intrinsic long-range magnetic order is absent in both FeS and FeSe and superconductivity is robust to small impurity phases,[30,41−44] there are strong magnetic fluctuations and magnetic order induced by pressure.[44−47] The absence of long-range magnetic order therefore can be explained by the collapse of the effect of chemical pressure just before the critical pressure for magnetic order is reached, as evidenced by the sharp deviation from the initial slope of the *c*/*a* ratio near the NCP (Figure 2b).

Beyond the average crystal structure, it is also instructive to address atomic element-specific bond distances. To shed light on the chemical bonding and the key parameters of the local crystallography of $FeCh_4$ (Ch = Se or S) tetrahedra, we studied the X-ray absorption near-edge structure (XANES) and the extended X-ray absorption fine structure (EXAFS), which provide important information about the hybridization between the Fe 3d and Ch 4p orbitals as well as accurate Fe−Ch bond distances.[48,49]

Typical features of the Fe K-edge XANES are denoted as A, B, and C, whereas those of the Se K-edge XANES are denoted as D and E (Figure 4a,b). Prepeak A is due to the direct 1s → 3d quadrupole transition to unoccupied states, with a contribution of the dipole transition from the Fe 1s to unoccupied Fe 3d−Se 4p hybrid bands.[50] Edge feature B is determined by the 1s → 4p transitions, whereas feature C results from the 1s → 4p state with a significant admixture to the Ch d states. The intensity of A increases with S concentration, indicating an increase in the level of Fe 3d−Se 4p hybridization. The decrease in the intensity of structure C indicates the reduction of the level of hybridization of the Fe 4p and Se d states due to the low Se concentration. The results for the Se K edge are consistent with those for the Fe K edge, in which peak D is due to the 1s → 4p dipole transition and feature E is the result of multiple scattering of the photoelectrons with the nearest neighbors. The increase in D with *x* is in agreement with the increase in A and the stronger

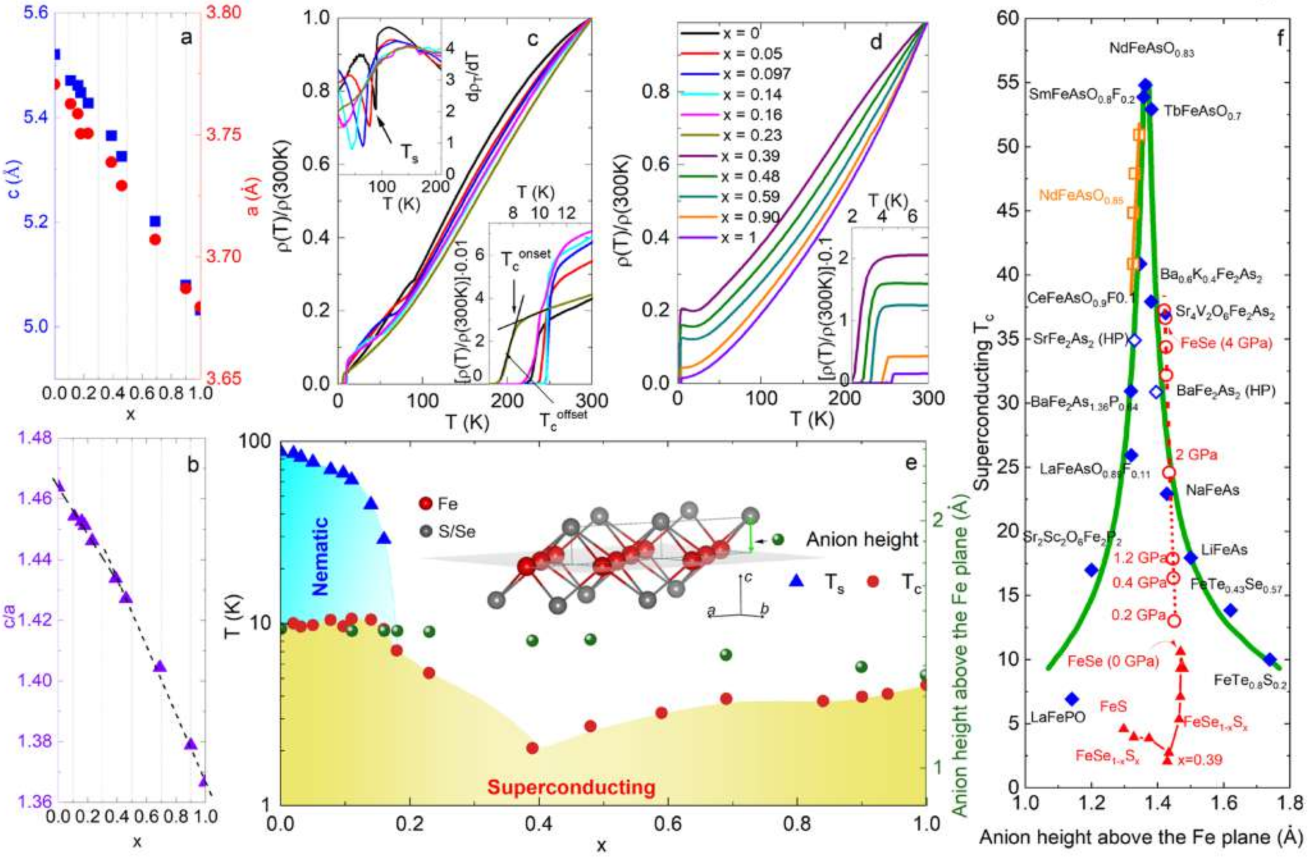

Figure 2. Changes in the average anion height above the iron plane in $Fe_{1-y}Se_{1-x}S_x$ ($0 \le x \le 1$; $y \le 0.1$). (a and b) Lattice parameters of the crystal structure (a, c, and the c/a ratio) obtained from Rietveld refinement. (c and d) Electrical resistivity of $Fe_{1-y}Se_{1-x}S_x$ normalized to values at 300 K [$\rho_T = \rho(T)/\rho(300\text{ K})$]. The left inset of panel c shows the $d\rho_T/dT$ around the structural transition; structural transition temperature T_s is inferred by the dip and indicated by the arrow. Legends for panels c and d are identical and are shown in panel d. (e) Composition−temperature (x−T) phase diagram for single crystals with values of T_c, T_s, and the average anion height above the Fe plane, depicted in the inset. (f) Superconducting T_c in iron-based superconductors from ref 5 with T_c values from this work (red triangles).

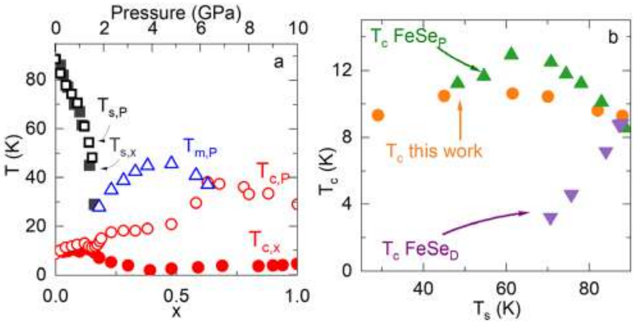

Figure 3. Comparison of pressure and sulfur substitution. (a) Comparison of the ground state changes as a function of chemical and hydrostatic pressure with x. Filled symbols represent data for $Fe_{1-y}Se_{1-x}S_x$, whereas empty symbols represent the temperature−pressure phase diagram of FeSe single crystals reported by Sun et al.[18] (b) T_c vs T_p for $Fe_{1-y}Se_{1-x}S_x$, pressurized FeSe ($FeSe_P$), and FeSe disordered by different synthesis conditions ($FeSe_D$).[18,38]

hybridization of Fe 3d−Se/S 4p bands. The dependence of the Fe and Se K-edge XANES features on S substitution resembles those observed for the high-pressure measurements and is the opposite of the effects induced by Te substitution.[48,51] Increased d−p hybridization is expected to promote delocalization.[52]

EXAFS presents a window into local bond distances around absorbing atom and could be described in the single-scattering approximation as[49]

$$\chi(k) = \sum_i \frac{N_i {S_0}^2}{k{R_i}^2} f_i(k_i R_i) e^{-2R_i/\lambda} e^{-2k^2\sigma_i^2} \sin[2kR_i + \delta_i(k)] \qquad (1)$$

where N_i is the number of neighboring atoms at a distance R_i from the photoabsorbing atom, ${S_0}^2$ is the passive electron reduction factor, $f_i(k, R_i)$ is the backscattering amplitude, λ is the photoelectron mean free path, δ_i is the phase shift of the photoelectrons, k is the photon wavenumber, and σ^2 is the correlated Debye−Waller factor measuring the mean square relative displacement of the photoabsorber−backscatter pairs. The first nearest neighbors of Fe atoms are four Se atoms located at 2.395 Å, and the next nearest neighbors are four Fe atoms sited at 2.668 Å.[39] The first nearest neighbors of Se atoms are four Fe atoms at 2.395 Å tetrahedral distances. Local structural information, such as the bond distance and Debye−Waller factor, was obtained by the best-fit model. The features above 3 Å are due to longer distances and multiple scattering effects. Because the first shell of the Se K edge is well separated from the distant shells, we fit the Se K-edge EXAFS using a model with a single distance and take only the main peaks of the Fe edge into consideration. Interestingly, the fitting can be improved only by using different values of Fe−Se and Fe−S

https://doi.org/10.1021/acs.inorgchem.2c00568
Inorg. Chem. 2022, 61, 11036−11045

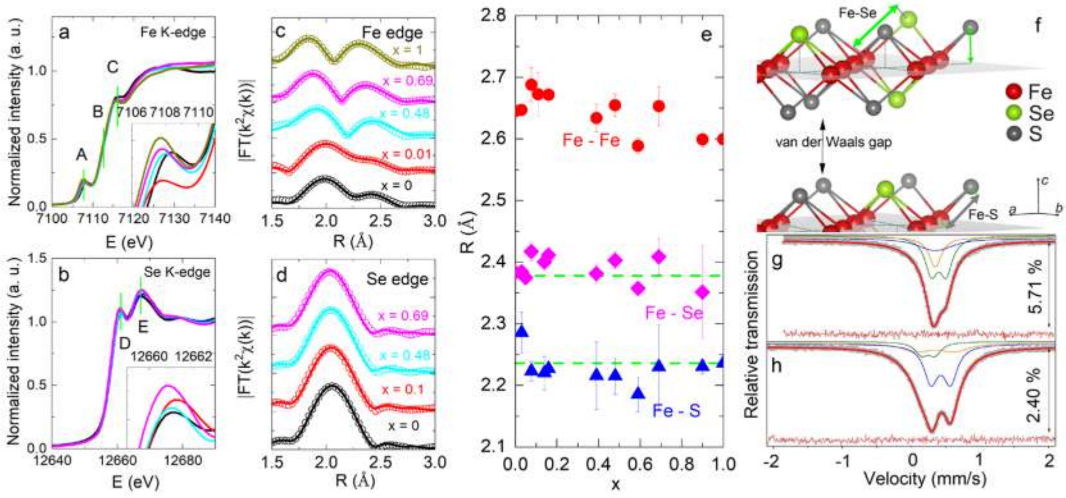

Figure 4. Local crystallography from XANES and EXAFS. (a and b) Normalized XANES spectra of $Fe_{1-y}Se_{1-x}S_x$ measured at the Fe K edge and Se K edge, respectively. The features in the Fe K-edge XANES are denoted by A, B, and C; those in Se K-edge XANES are denoted by D and E. (c and d) Fourier transform (FT) magnitudes of the k^2-weighted EXAFS oscillations at Fe K edge and Se K edge. (e) Fe−Fe, Fe−Se, and Fe−S distances determined by EXAFS as a function of x. The Fe−Se and Fe−S bond distances show small changes for all values of x and remain close to values observed in end member compounds FeSe and FeS. (f) Crystal structure of $Fe_{1-y}Se_{1-x}S_x$ with the depicted van der Waals gap, Fe planes, and different Fe−Se and Fe−S bond distances. Mössbauer spectra recorded in the low-velocity range at 295 K of (g) tetragonal $Fe_{0.96}Se_{0.31}S_{0.69}$ and (h) tetragonal $Fe_{0.9}Se_{0.82}S_{0.18}$.

bond lengths (Figure 4e,f). Hence, Fourier transform magnitudes of the EXAFS oscillations weighted by k^2 and extracted from the Fe K and Se K edges (Figure 4c,d) indicate that Fe−Se and Fe−S bond lengths in all investigated materials, including in alloyed crystals, do not deviate much from Fe−Se and Fe−S bond lengths in pure FeSe and pure FeS. The Fe−Fe bond length shows a small increase for $x \leq 0.10$, along with that of T_c (Figure 4e), and a decrease for further S substitution results as $x \to 1$. This suggests rather deformed $FeCh_4$ tetrahedra. Moreover, wider distributions of Fe−S and Fe−Se bond distances for $0.4 \leq x \leq 0.9$ inferred from error bars (Figure 4e) imply greater disorder. Consequently, there is a local structural inhomogeneity in most $Fe(Se/S)_4$ tetrahedra in the middle of the alloy series due to the comparable numbers of Fe−Se and Fe−S bonds in $FeCh_4$.

For insight into the local charge distribution around Fe atoms at the 2a Wyckoff site of the $P4/nmm$ space group, we have used Mössbauer spectroscopy. First, we consider the coordination spheres of the iron probe. The four nearest neighbor (NN) chalcogen atoms make the surrounding $FeCh_4$ (Ch = Se or S) tetrahedron. The next nearest neighbors (NNNs) are two metal shells with four iron atoms in each shell. Farther behind are two chalcogen shells that consist of four and eight chalcogen atoms, respectively. The nearer four are situated in the same atomic plane with the iron. The first half of farther eight atoms are above and the second half below this plane stacked along the c-axis. The symmetry point group of the Fe atomic site in FeS and FeSe is $\bar{4}m2$. The non-ideal tetrahedral surrounding of Fe results in a nonspherical charge distribution around the probe and the emergence of an electric field gradient (EFG).[53,54] Substitution of different chalcogen atoms into an iron−chalcogenide material additionally breaks the Fe local symmetry, causing more pronounced EFG. Replacement of sulfur with selenium defines a new Se-containing atomic plane that is different from the iron and sulfur planes in FeS.[53] In pure materials, bond distance d_{Fe-Se} in tetragonal FeSe is ∼10% longer than d_{Fe-S} in tetragonal FeS.[54] The Se plane in FeSe is farther from the Fe plane than from the S plane in FeS, expanding the crystallographic unit cell along the c-axis.

In alloys, the number of occupied chalcogen sites in the Se or S planes depends on the Se:S atomic ratio. This leads to many nonequivalent Fe sites in contrast to the uniform chalcogen surrounding in pure FeS or FeSe. It is expected that Mössbauer spectroscopy will detect a distribution of quadrupole splittings (Δ) because of different EFGs.

The binomial distribution describes the probability of the appearance of coordination spheres of the Fe atom with different S and Se ion contents:[55]

$$p(z_1, \ldots z_k, n_1, \ldots n_k, c) = \prod_{i=1}^{k} p_{z_i}(n_i, c) = \prod_{i=1}^{k} \binom{z_i}{n_i} c^{n_i}(1-c)^{z_i-n_i} \tag{2}$$

where $0 \leq n_i \leq z_i$ and p is the probability mass function (PMF). The PMF describes the probability of having n_i impurities on z_i host sites of the ith shell for impurity concentration c. Considering only the tetrahedron with four NNs for $c = 0.3$, the equation gives a $p(n_1 = 0)$:$p(n_1 = 1)$:$p(n_1 = 2)$:$p(n_1 = 3)$:$p(n_1 = 4)$ ratio of approximately 24:41:26:8:1. Hence, the Δ distribution by means of the doublets with Lorentz lines with an area ratio follows the PMF ratio. The experimental spectra can be fit with only the three doublets fitting model in which one of the doublets is collapsed into a single line in the spectrum of tetragonal $Fe_{0.96}Se_{0.31}S_{0.69}$ (Table S2). This is to be expected because it originates from the tetrahedron without Se atoms where a very low Δ value was measured.[46,53] When S substitutes for Se in $FeSe_4$, the subspectrum with the largest area is assigned to the $FeSe_4$ tetrahedron.[56,57] The other two doublets in both spectra arise from the Se atom in FeS_4 tetrahedra or, vice versa, the existence of at least one S on the $FeSe_4$ tetrahedron corners.

Wider lines and large hyperfine parameter uncertainties are consequences of a great number of spatial combinations of substituted atoms. Bader analysis of the pure iron chalcogenides shows that there is a larger charge transfer from the Fe atom to the S atom than to the Se atom.[54] The charge transfer changes the chemical shift, i.e., δ. Therefore, the value of δ is the result of a competition between electron occupation on the 4s and 3d orbitals of the Fe.[58] According to the Bader analysis, there is a bond critical point between the NN chalcogen ion and the NNN chalcogen from the adjacent layer in the fifth shell.[54] There are significant probabilities for the next PMF: $p(n_1 = 0, n_s = 2, 3)$, $p(n_1 = 1, n_s = 1, 2, 3, 4)$, and $p(n_1 = 2, n_s = 1, 2, 3)$. All contribute to changes in the probe electron density, additionally smearing the quadrupole distribution with consequences for the subspectrum area ratio. Therefore, our data confirm the randomness of the spatial distribution of the Se and S atoms in alloys, and therefore, sulfur entails both pressure and disorder. Because there is no comparably dramatic increase in T_c as in FeSe under pressure,[17] it is plausible to conclude that disorder counterbalances pressure for x up to the NCP where the abrupt change in the superconducting gap takes place.[19]

It is obvious that random sulfur substitution in FeSe and inhomogeneous Fe−Se/S bond distances in $FeCh_4$ tetrahedra induce changes in the S and Se atomic heights from the average values inferred from Rietveld measurement (Figure 2e). Therefore, we focus next on the atomic vibrations along the crystallographic *c*-axis. Of interest are the Raman shift and Lorentzian full width at half-maximum (fwhm) of A_{1g} and B_{1g} Raman modes at 100 K (Figure 5a). We observe a good agreement in the trends of the change in the Raman shift and peak widths. In the absence of Fano-shaped peak distortions, the peak width gives a caliper of phonon vibration-related crystallographic disorder. A larger fwhm is consistent with greater disorder. For better comparison with changes in superconducting T_c, in Figure 5b we plot $[\mathrm{fwhm}(x)]^{-1}$, normalized to $[\mathrm{fwhm}(0)]^{-1}$, i.e., to FeSe without S substitution, for B_{1g} and A_{1g} modes as S enters the lattice with an increase in x. Smaller values of $[\mathrm{fwhm}(x)]^{-1}/[\mathrm{fwhm}(0)]^{-1}$ point to greater disorder relative to that of pure FeSe.

The Raman active A_{1g} and B_{1g} phonon modes correspond to fully symmetric and out-of-phase vibrations of the chalcogen and Fe atoms along the *c*-axis, respectively.[59−61] The B_{1g} mode has the same symmetry as the nematic fluctuations, both charge and spin, and is therefore expected to couple to deformations of this type.[60,62,63] Both lines broaden due to disorder as x is increased. However, whereas the relative change in the inverse half-width of the B_{1g} phonon $[\mathrm{fwhm}\ B_{1g}(x)]^{-1}$ tracks relative changes in $T_c(x)$ and $T_s(x)$ (Figure 5c), the relative change in $[\mathrm{fwhm}\ A_{1g}(x)]^{-1}$ does not.

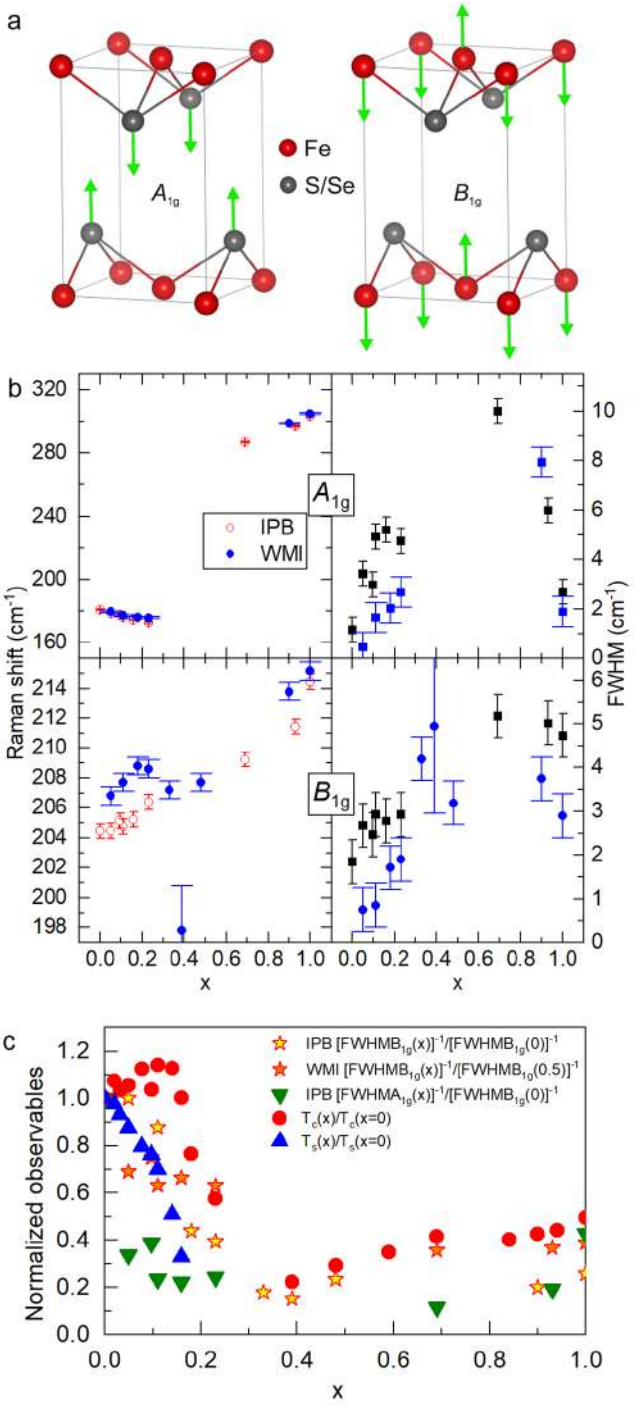

Figure 5. (a) Unit cell of FeSe/S with depicted A_{1g} and B_{1g} Raman modes. (b) Raman shift and Lorentzian full width at half-maximum of the A_{1g} and B_{1g} modes. (c) Relative changes in T_c, T_s, and widths of Raman active A_{1g} and B_{1g} modes with respect to FeSe; the B_{1g} mode measured at WMI is normalized to $x = 0.05$.

DISCUSSION

To start, we note that the concept of anion height comes from the average crystal structure; it does not contain information from local crystallography. However, bond lengths regulate the Fe−Ch overlap and the $FeCh_4$ tetrahedral shape that, in turn, controls the crystal field levels and thus the orbital occupancies and relative mixing of Fe atom d_{xz} and d_{yz} orbitals.[11,12] Hence, disorder in Fe−Ch bond distances is likely to suppress T_s, which is rather sensitive upon energy splitting between the d_{xz} and d_{yz} atomic orbitals of the Fe atom.[60,64] Moreover, it will also influence the superconducting gap at the Γ point at the Brillouin zone via perturbation of the d_{xz} spectral weight at the Fermi level, and thus T_c.[65] Finally, a high degree of bond disorder in this context could be connected to strong charge-nematic or magnetic spin fluctuations that mediate superconducting pairing in the middle of the alloy series.[7,12,63,66] The increase in Fe vibrational disorder along the *c*-axis is coincident with the suppression of $T_c(x)$, as shown in Figure 5c.

A picture emerges in which distinct Fe−S and Fe−Se chemical bonds randomly distributed in the lattice influence the atomic vibration of Fe and Ch atoms in the *c*-axis direction. Determining the spatial extent of this inhomogeneity as well as local conducting properties by transmission electron and scanning tunneling microscopy would be of interest. On the contrary, connection of Fe B_{1g} mode disorder with a change in the structural nematic and superconducting critical temperature with x may affect high-magnetic field properties such as upper critical field H_{c2}. This would be of interest for materials with higher values of T_c such as FeSe crystals intercalated by a molecular spacer layer or thin films.[27,28] We note that $Fe_{1+y}Te_{1-x}Se_x$, amenable to wire fabrication and of interest for applications, also exhibits distinct Fe−Te and Fe−Se bond distances.[67,68] In fact, changes in the Fe−Se and Fe−S bonds with x (Figure 4e) are smaller than changes in $Fe_{1+y}Te_{1-x}Se_x$ alloys in which Fe−Te and Fe−Se bond lengths exhibit an only small decrease from FeTe and FeSe.[69−71] The local structural inhomogeneity should have direct implications for the electronic states near the Fermi energy because they are connected with the degree of delocalization of the Fe d orbitals.[12]

CONCLUSION

In summary, in $Fe_{1-y}Se_{1-x}S_x$ $(0 \leq x \leq 1; y \leq 1)$ crystal alloys superconducting T_c values do not scale with anion height above the Fe plane in the presence (FeSe) or absence (FeS) of nematic order, in contrast to most known Fe-based superconductors. Investigation of the local crystallography from EXAFS and Mössbauer spectroscopy reveals that sulfur substitutes for Se randomly in alloys whereas Fe−Se and Fe−S bonds remain the same as in pure FeSe and pure FeS, respectively. This causes disorder in the atomic vibration orthogonal to the Fe plane as seen in A_{1g} and B_{1g} Raman active modes of Se and Fe, respectively. Changes in $T_s(x)$ and $T_c(x)$ compared to T_c and T_s in FeSe are not connected with A_{1g} but are connected with B_{1g} mode disorder. Suppression of the nematic transition associated with the tetragonal-to-orthorhombic change in the crystallographic unit cell upon cooling by S substitution at Se atomic positions follows the increased level of B_{1g} disorder. In contrast, increased B_{1g} mode disorder does not affect T_c, which increases with S substitution in the nematic region due to the chemical pressure effect. For a high degree of bond disorder near the middle of the alloy series when T_s is fully suppressed, relative changes in $T_c(x)$ with respect to FeSe follow the relative disorder in B_{1g} mode vibrations of Fe atoms. Because the B_{1g} mode couples to spin and charge nematic fluctuations, our results show that such fluctuations are tied to interlayer crystallography of FeSe/S and are of interest for the design of novel intercalated and ultrathin FeSe materials.

ASSOCIATED CONTENT

Supporting Information

The Supporting Information is available free of charge at https://pubs.acs.org/doi/10.1021/acs.inorgchem.2c00568.

Experimental details, crystal structures, sample to sample reproducibility and Wilson ratio, and results of first-principles calculation (PDF)

AUTHOR INFORMATION

Corresponding Authors

Cedomir Petrovic − *Condensed Matter Physics and Materials Science Department, Brookhaven National Laboratory, Upton, New York 11973, United States; Materials Science and Chemical Engineering Department, Stony Brook University, Stony Brook, New York 11790, United States;* orcid.org/0000-0001-6063-1881; Email: petrovic@bnl.gov

Aifeng Wang − *Condensed Matter Physics and Materials Science Department, Brookhaven National Laboratory, Upton, New York 11973, United States;* Present Address: School of Physics, Chongqing University, Chongqing 400044, China; orcid.org/0000-0003-2425-3259; Email: afwang@cqu.edu.cn

Authors

Ana Milosavljevic − *Center for Solid State Physics and New Materials, Institute of Physics Belgrade, University of Belgrade, 11080 Belgrade, Serbia*

A. M. Milinda Abeykoon − *National Synchrotron Light Source II, Brookhaven National Laboratory, Upton, New York 11973, United States*

Valentin Ivanovski − *Vinca Institute of Nuclear Sciences, University of Belgrade, Belgrade 11001, Serbia*

Qianheng Du − *Condensed Matter Physics and Materials Science Department, Brookhaven National Laboratory, Upton, New York 11973, United States; Materials Science and Chemical Engineering Department, Stony Brook University, Stony Brook, New York 11790, United States;* Present Address: Materials Science Division, Argonne National Laboratory, Lemont, IL 60439.

Andreas Baum − *Walther Meissner Institut, Bayerische Akademie der Wissenschaften, 85748 Garching, Germany; Fakultät für Physik E23, Technische Universität München, 85748 Garching, Germany*

Eli Stavitski − *National Synchrotron Light Source II, Brookhaven National Laboratory, Upton, New York 11973, United States*

Yu Liu − *Condensed Matter Physics and Materials Science Department, Brookhaven National Laboratory, Upton, New York 11973, United States;* Present Address: Los Alamos National Laboratory, MS K764, Los Alamos, NM 87545.; orcid.org/0000-0001-8886-2876

Nenad Lazarevic − *Center for Solid State Physics and New Materials, Institute of Physics Belgrade, University of Belgrade, 11080 Belgrade, Serbia;* orcid.org/0000-0001-6310-9511

Klaus Attenkofer − *National Synchrotron Light Source II, Brookhaven National Laboratory, Upton, New York 11973, United States;* Present Address: ALBA Synchrotron Light Source, Cerdanyola del Valles, E-08290 Barcelona, Spain.

Rudi Hackl − *Walther Meissner Institut, Bayerische Akademie der Wissenschaften, 85748 Garching, Germany; Fakultät für Physik E23, Technische Universität München, 85748 Garching, Germany*

Zoran Popovic − *Center for Solid State Physics and New Materials, Institute of Physics Belgrade, University of Belgrade, 11080 Belgrade, Serbia; Serbian Academy of Sciences and Arts, Belgrade 11000, Serbia*

Complete contact information is available at: https://pubs.acs.org/10.1021/acs.inorgchem.2c00568

Notes

The authors declare no competing financial interest.

ACKNOWLEDGMENTS

Work at Brookhaven National Laboratory was supported by the U.S. Department of Energy (DOE), Office of Science, Office of Basic Energy Sciences (DOE BES), under Contract DE-SC0012704 (A.W., Y.L., Q.D., and C.P.). This research used the 8-ID (ISS) and 28-ID-1 (PDF) beamlines of National Synchrotron Light Source 2, a U.S. DOE Office of Science User Facility operated for the DOE Office of Science by Brookhaven National Laboratory under Contract DE-SC0012704. Raman spectroscopy measurements were funded by Serbian Academy of Sciences and Arts Contract F-134, by the Institute of Physics Belgrade through a grant from the Ministry of Education, Science and Technological Development of the Republic of Serbia, and by the Science Fund of the Republic of Serbia (PROMIS, 6062656, StrainedFeSC). Mössbauer spectroscopy and corresponding calculations were funded by the Ministry of Education, Science and Technological Development of the Republic of Serbia.

REFERENCES

(1) Onnes, H. K. The persistence of electric currents without electromotive force in superconductors. *C. R. Hebd. Seances Acad. Sci.* **1914**, *159*, 34−38.

(2) Fröhlich, H. H. Theoretical aspects of superconductivity: crystal structure and superconductivity. *Nature* **1951**, *168*, 280.

(3) Matthias, B. T. Empirical Relation between Superconductivity and the Number of Valence Electrons per Atom. *Phys. Rev.* **1955**, *97*, 74−76.

(4) Müller-Buschbaum, H. The Crystal Chemistry of High-Temperature Oxide Superconductors and Materials with Related Structures. *Angew. Chem., Int. Ed. Engl.* **1989**, *28*, 1472−1493.

(5) Simon, A. Superconductivity and Chemistry. *Angew. Chem., Int. Ed. Engl.* **1997**, *36*, 1788−1806.

(6) Ozawa, T. C.; Kauzlarich, S. Chemistry of layered *d*-metal pnictide oxides and their potential as candidates for new superconductors. *Sci. Technol. Adv. Mater.* **2008**, *9*, 033003.

(7) Mizuguchi, Y.; Hara, Y.; Deguchi, K.; Tsuda, K.; Yamaguchi, T.; Takeda, K.; Kotegawa, H.; Tou, H.; Takano, Y. Anion height dependence of T$_c$ of the Fe-based superconductor. *Superconduct. Sci. Technol.* **2010**, *23*, 054013.

(8) Oganov, A.; Lyakhov, A. O.; Valle, M. How Evolutionary Crystal Structure Prediction Works − and Why. *Acc. Chem. Res.* **2011**, *44*, 227−237.

(9) Rasaki, S. A.; Thomas, T.; Yang, M. Iron based chalcogenide and pnictide superconductors: from discovery to chemical ways forward. *Prog. Solid State Chem.* **2020**, *59*, 100282.

(10) Gui, X.; Lv, B.; Xie, W. Chemistry in Superconductors. *Chem. Rev.* **2021**, *121*, 2966−2991.

(11) Fernandes, R. M.; Chubukov, A. V.; Schmalian, J. What drives nematic order in iron-based superconductors. *Nat. Phys.* **2014**, *10*, 97−104.

(12) Yin, Z. P.; Haule, K.; Kotliar, G. Kinetic frustration and the nature of the magnetic and paramagnetic states in iron pnictides and iron chalcogenides. *Nature Materails* **2011**, *10*, 932.

(13) McQueen, T. M.; Williams, A. J.; Stephens, P. W.; Tao, J.; Zhu, Y.; Ksenofontov, V.; Casper, F.; Felser, C.; Cava, R. J. Tetragonal to Orthorombic Structural Phase Transition at 90 K in the Superconductor Fe$_{1.01}$Se. *Phys. Rev. Lett.* **2009**, *103*, 057002.

(14) Wang, Q.; Shen, Y.; Pan, B.; Hao, Y.; Ma, M.; Zhou, F.; Steffens, P.; Schmalzl, K.; Forrest, T. R.; Abdel-Hafiez, M.; Chen, X.; Chareev, A.; Vasiliev, A. N.; Bourges, P.; Sidis, Y.; Cao, H.; Zhao, J. Strong interplay between stripe fluctuations, nematicity and superconductivity in FeSe. *Nat. Mater.* **2016**, *15*, 159−163.

(15) Lu, X.; Park, J. T.; Zhang, R.; Luo, H.; Nevidomskyy, A. H.; Si, Q.; Dai, P. Nematic spin correlations in the tetragonal state of uniaxial-strained BaFe$_{2\text{-}x}$Ni$_x$As$_2$. *Science* **2014**, *345*, 657−660.

(16) Chu, J.-H.; Analytis, J.; De Greve, K.; McMahon, P.; Islam, Z.; Yamamoto, Y.; Fisher, I. R. In-Plane Resistivity Anisotropy in a Underdoped Iron Arsenide Superconductor. *Science* **2010**, *329*, 824−826.

(17) Medvedev, S.; McQueen, T. M.; Troyan, I. A.; Palasyuk, I. A.; Eremets, M. I.; Cava, R. J.; Naghavi, S.; Casper, F.; Ksenofontov, V.; Wortmann, G.; Felser, C. Electronic and magnetic phase diagram of β-Fe$_{1.01}$Se with superconductivity at 36.7 K under pressure. *Nat. Mater.* **2009**, *8*, 630.

(18) Sun, J. P.; Matsuura, K.; Ye, G. Z.; Mizukami, Y.; Shimozawa, M.; Matsubayashi, K.; Yamashita, M.; Watashige, T.; Kasahara, S.; Matsuda, Y.; Yan, J. Q.; Sales, B. C.; Uwatoko, Y.; Cheng, J. G.; Shibauchi, T. Dome-shaped magnetic order competing with high-temperature superconductivity at high pressures in FeSe. *Nat. Commun.* **2016**, *7*, 12146.

(19) Sato, Y.; Kasahara, S.; Taniguchi, T.; Xing, X.; Kasahara, Y.; Tokiwa, Y.; Yamakawa, Y.; Kontani, H.; Shibauchi, T.; Matsuda, Y. Abrupt change of the superconducting gap structure at the nematic critical point in FeSe$_{1-x}$S$_x$. *Proc. Natl. Acad. Sci. U.S.A.* **2018**, *115*, 1227−1231.

(20) Hosoi, S.; Matsuura, K.; Ishida, K.; Wang, H.; Mizukami, Y.; Watashige, T.; Kasahara, S.; Matsuda, Y.; Shibauchi, T. Nematic quantum critical point without magnetism in FeSe$_{1-x}$S$_x$ superconductors. *Proc. Natl. Acad. Sci. U.S.A.* **2016**, *113*, 8139−8143.

(21) Coldea, A. I.; Blake, S. F.; Kasahara, S.; Haghighirad, A. A.; Watson, M. D.; Knafo, W.; Choi, E. S.; McCollam, A.; Reiss, P.; Yamashita, T.; Bruma, M.; Speller, S. C.; Matsuda, Y.; Wolf, T.; Shibauchi, T.; Schofield, A. J. Evolution of the low-temperature Fermi surface of superconducting FeSe$_{1-x}$S$_x$ across a nematic phase transition. *npj Quantum Mater.* **2019**, *4*, 2.

(22) Licciardello, S.; Buhot, J.; Lu, J.; Ayres, J.; Kasahara, S.; Matsuda, Y.; Shibauchi, T.; Hussey, N. E. Electrical resistivity across a nematic quantum critical point. *Nature* **2019**, *567*, 213−217.

(23) Reiss, P.; Watson, M. D.; Kim, T. K.; Haghighirad, A. A.; Woodruff, D. N.; Bruma, M.; Clarke, S. J.; Coldea, A. I. Suppression of electronic correlations by chemical pressure from FeSe to FeS. *Phys. Rev. B* **2017**, *96*, 121103.

(24) Okamoto, H. The Fe-Se (Iron-Selenium) System. *J. Phase Equilib.* **1991**, *12*, 383−389.

(25) Nitsche, F.; Goltz, T.; Klauss, H.-H.; Isaeva, A.; Müller, U.; Schnelle, W.; Simon, P.; Doert, Th.; Ruck, M. Room-Temperature Synthesis, Hydrothermal Recrystallization, and Properties of Metastable Stoichiometric FeSe. *Inorg. Chem.* **2012**, *51*, 7370−7376.

(26) Vanukov, A. V.; Babashev, I. S.; Bystrov, V. P. Phase-Diagram and Thermodynamics of Iron-Sulfur System. *Russ. J. Phys. Chem.* **1972**, *46*, 880.

(27) Burrard-Lucas, M.; Free, D. G.; Sedlmaier, S. J.; Wright, J. D.; Cassidy, S. J.; Hara, Y.; Corkett, A. J.; Lancaster, T.; Baker, P. J.; Blundell, S. J.; Clarke, S. J. Enhancement of the superconducting transition temperature of FeSe by intercalation of a molecular spacer layer. *Nat. Mater.* **2013**, *12*, 15−19.

(28) Wang, Q.-H.; Li, Z.; Zhang, W.-H.; Zhang, Z.-C.; Zhang, J.-S.; Li, W.; Ding, H.; Ou, Y.-B.; Deng, P.; Chang, K.; Wen, J.; Song, C.-L.; He, K.; Jia, J.-F.; Ji, S.-H.; Wang, Y.-Y.; Wang, L.-L.; Chen, X.; Ma, X.-C.; Xue, Q.-H. Interface-Induced High-Temperature Superconductivity in Single Unit-Cell FeSe Films on SrTiO$_3$. *Chin. Phys. Lett.* **2012**, *29*, 037402.

(29) Tan, S.; Zhang, Y.; Xia, M.; Ye, Z.; Chen, F.; Xie, X.; Peng, R.; Xu, D.; Fan, Q.; Xu, H.; Jiang, J.; Zhang, T.; Lai, X.; Xiang, T.; Hu, J.; Xie, B.; Feng, D. Interface-induced superconductivity and strain-dependent spin density waves in FeSe/SrTiO$_3$ thin films. *Nat. Mater.* **2013**, *12*, 634−640.

(30) Hu, R.; Lei, H.; Abeykoon, M.; Bozin, E. S.; Billinge, S. J. L.; Warren, J. B.; Siegrist, T.; Petrovic, C. Synthesis, crystal structure and magnetism of β-Fe$_{1.00(2)}$Se$_{1.00(3)}$ single crystals. *Phys. Rev. B* **2011**, *83*, 224502.

(31) Lei, H.; Abeykoon, M.; Bozin, E. S.; Wang, K.; Warren, J. B.; Petrovic, C. Phase Diagram of KxFe2-ySe2-xSz and the Suppression of

its Superconducting State by an Fe2-Se/S Tetrahedron Distortion. *Phys. Rev. Lett.* **2011**, *107*, 137002.

(32) Borg, C. K. H.; Zhou, X.; Eckberg, C.; Campbell, D. J.; Saha, S. R.; Paglione, J.; Rodriguez, E. E. Strong anisotropy in nearly ideal tetrahedral superconducting FeS single crystals. *Phys. Rev. B* **2016**, *93*, 094522.

(33) Toby, B. H.; Von Dreele, R. B. GSAAS-II: The genesis of a modern open-source all purpose crystallography software package. *J. Appl. Crystallogr.* **2013**, *46*, 544−549.

(34) Ravel, B.; Newville, M. J. ATHENA, ARTEMIS, HEPHAESTUS: data analysis for X-ray absorption spectroscopy using IFEFFIT. *Synchrotron Radiat.* **2005**, *12*, 537−541.

(35) Brand, R. A. *WinNormos Mössbauer fitting program*; Universität Duisburg: Duisburg, Germany, 2008.

(36) See the Supporting Information.

(37) Mizuguchi, Y.; Tomioka, F.; Tsuda, S.; Yamaguchi, T.; Takano, Y. Substitution Effects on FeSe Superconductor. *J. Phys. Soc. Jpn.* **2009**, *78*, 074712.

(38) Böhmer, A. E.; Taufour, V.; Straszheim, W. E.; Wolf, T.; Canfield, P. C. Variation of transition temperatures and residual resistivity ratio in vaor-grown FeSe. *Phys. Rev. B* **2016**, *94*, 024526.

(39) Margadonna, S.; Takabayashi, Y.; Ohishi, Y.; Mizuguchi, Y.; Takano, Y.; Kagayama, T.; Nakagawa, T.; Takata, M.; Prassides, K. Pressure evolution of the low-temperature crystal structure and bonding of the superconductor FeSe (T_c=37 K). *Phys. Rev. B* **2009**, *80*, 064506.

(40) Rößler, S.; Huang, C.-L.; Jiao, L.; Koz, C.; Schwarz, U.; Wirth, S. Influence of disorder on the signature of the pseudogap and multigap superconducting behavior in FeSe. *Phys. Rev. B* **2018**, *97*, 094503.

(41) Lai, X.; Zhang, H.; Wang, Y.; Wang, X.; Zhang, X.; Lin, J.; Huang, F. Observation of Superconductivity in Tetragonal FeS. *J. Am. Chem. Soc.* **2015**, *137*, 10148−10151.

(42) Hsu, F. C.; Luo, J.-Y.; Yeh, K.-W.; Chen, T.-K.; Huang, T.-W.; Wu, P. M.; Lee, Y.-C.; Huang, Y.-L.; Chu, Y.-Y.; Yan, D. C.; Wu, M. K. Superconductivity in the PbO-type structure of α-FeSe. *Proc. Natl. Acad. Sci. U.S.A.* **2008**, *105*, 14262−14264.

(43) Kirschner, F. K.; Lang, F.; Topping, C. V.; Baker, P. J.; Pratt, F. L.; Wright, S. E.; Woodruff, D. N.; Clarke, S. J.; Blundell, S. J. Robustness of superconductivity to competing magnetic phases in tetragonal FeS. *Phys. Rev. B* **2016**, *94*, 134509.

(44) Imai, T.; Ahilan, K.; Ning, F. L.; McQueen, T. M.; Cava, R. J. Why Does Undoped FeSe Become a High-T_c Superconductor Under Pressure? *Phys. Rev. Lett.* **2009**, *102*, 177005.

(45) Bendele, M.; Amato, A.; Conder, K.; Elender, M.; Keller, H.; Klauss, H.-H.; Luetkens, H.; Pomjakushina, E.; Raselli, A.; Khasanov, R. Pressure-Induced Static Magnetic Order in Superconducting $FeSe_{1-x}$. *Phys. Rev. Lett.* **2010**, *104*, 087003.

(46) Holenstein, S.; Pachmayr, U.; Guguchia, Z.; Kamusella, S.; Khasanov, R.; Amato, R.; Baines, C.; Klauss, H.-H.; Morenzoni, E.; Johrendt, D.; Luetkens, H. Coexistence of low-moment magnetism and superconductivity in tetragonal FeS and suppression of T_c under pressure. *Phys. Rev. B* **2016**, *93*, 140506.

(47) Kwon, K. D.; Refson, K.; Bone, S.; Qiao, R.; Yang, W.-L.; Liu, Z.; Sposito, G. Magnetic ordering in tetragonal FeS: Evidence for strong itinerant spin fluctuations. *Phys. Rev. B* **2011**, *83*, 064402.

(48) Bendele, M.; Marini, C.; Joseph, B.; Simonelli, L.; Dore, P.; Pascarelli, S.; Chikovani, M.; Pomjakushina, E.; Conder, K.; Saini, N. L.; Postorino, P. Dispersive X-ray absorption studies at the Fe K-edge on the iron chalcogenide superconductor FeSe under pressure. *J. Phys.: Condens. Matter* **2013**, *25*, 425704.

(49) Prins, R., Konningsberger, D. S., Eds. *X-ray Absorption: Principles, Applications, Techniques of EXAFS, XANES*; Wiley: New York, 1998.

(50) De Groot, F.; Vanko, G.; Glatzel, P. The 1*s* X-ray absorption pre-edge structures in transition metal oxides. *J. Phys.: Condens. Matter* **2009**, *21*, 104207.

(51) Joseph, B.; Iadecola, A.; Simonelli, L.; Mizuguchi, Y.; Takano, Y.; Mizokawa, T.; Saini, N. L. A study of the electronic structure of $FeSe_{1-x}Te_x$ chalcogenides by Fe and Se K-edge X-ray absorption near edge structure measurements. *J. Phys.: Condens. Matter* **2010**, *22*, 485702.

(52) Ishizuka, J.; Yamada, T.; Yanagi, Y.; Ono, Y. Fermi Surface, Pressure-Induced Antiferromagnetic Order, and Superconductivity in FeSe. *J. Phys. Soc. Jpn.* **2018**, *87*, 014705.

(53) Wang, A.; Wu, L.; Ivanovski, V. N.; Warren, J. B.; Tian, J.; Zhu, Y.; Petrovic, C. Critical current density and vortex pinning in tetragonal $FeS_{1-x}Se_x$. *Phys. Rev. B* **2016**, *94*, 094506.

(54) Koteski, V.; Ivanovski, V. N.; Umicevic, A.; Belosevic-Cavor, J.; Toprek, D.; Mahnke, H.-E. First-principles calculations of tetragonal Fe*X* (*X* = S, Se, Te): Magnetism, hyperfine-interaction, and bonding. *J. Magn. Magn. Mater.* **2017**, *441*, 769−775.

(55) Vincze, I.; Campbell, A. I. Mössbauer measurements in iron-based alloys with transition metals. *J. Phys. F: Met. Phys.* **1973**, *3*, 647−663.

(56) Blachowski, A.; Ruebenbauer, K.; Zukrowski, J.; Przewoznik, J.; Wojciechowski, K.; Stadnik, Z. M. Mössbauer spectroscopy evidence for the lack of iron magnetic moment in superconducting FeSe. *J. Alloys. Compounds* **2010**, *494*, 1−3.

(57) Sklyarova, A.; Linden, J.; Tewari, G. C.; Rautama, E.-L.; Karppinen, M. ^{57}Mössbauer study of a secondary phase in $FeSe_{1-x}$ with a large quadrupole splitting. *Hyperfine Interact.* **2014**, *226*, 341−349.

(58) Menil, F. Systematic trends of the ^{57}Fe Mössbauer isomer shifts in (FeO_n) and (FeF_n) polyhedra. Evidence of a new correlation between the isomer shift and the inductive effect of the competing bond *T-X* (→ Fe) (where X is O or F and T any element with a formal positive charge). *J. Phys. Chem. Solids* **1985**, *46*, 763.

(59) Baum, A.; Milosavljevic, A.; Lazarevic, N.; Radonjic, M. M.; Nikolic, B.; Mitschek, M.; Maranloo, Z. I.; Scepanovic, M.; Grujic-Brojcin, M.; Stojilovic, N.; Opel, M.; Wang, A.; Petrovic, C.; Popovic, Z. V.; Hackl, R. Phonon anomalies in FeS. *Phys. Rev. B* **2018**, *97*, 054306.

(60) Glamazda, A.; Lemmens, P.; Ok, J. M.; Kim, J. S.; Choi, K. Y. Dichotomic nature of spin and electronic fluctuations in FeSe. *Phys. Rev. B* **2019**, *99*, 075142.

(61) Baum, A.; Ruiz, H. N.; Lazarevic, N.; Wang, Y.; Böhm, T.; Hosseinian Ahangharnejhad, R.; Adelmann, P.; Wolf, T.; Popovic, Z. V.; Moritz, B.; Devereaux, T. P.; Hackl, R. Frustrated spin order and stripe fluctuations in FeSe. *Commun. Phys.* **2019**, *2*, 14.

(62) Massat, P.; Farina, D.; Paul, I.; Karlsson, S.; Strobel, P.; Toulemonde, P.; Méasson, M.-A.; Cazayous, M.; Sacuto, A.; Kasahara, S.; Shibauchi, T.; Matsuda, Y.; Gallais, Y. Charge-induced nematicity in FeSe. *Proc. Natl. Acad. Sci. U.S.A.* **2016**, *113*, 9177−9181.

(63) Ruiz, H.; Wang, Y.; Moritz, B.; Baum, A.; Hackl, R.; Devereaux, T. P. Frustrated magnetism from local moments in FeSe. *Phys. Rev. B* **2019**, *99*, 125130.

(64) Baek, S.-H.; Efremov, D. V.; Ok, M.; Kim, J. S.; van den Brink, J.; Büchner, B. Orbital-driven nematicity in FeSe. *Nat. Mater.* **2015**, *14*, 210−214.

(65) Liu, D.; Li, C.; Huang, J.; Lei, B.; Wang, L.; Wu, X.; Shen, B.; Gao, Q.; Zhang, Y.; Liu, X.; Hu, Y.; Xu, Y.; Liang, A.; Liu, J.; Ai, P.; Zhao, L.; He, S.; Yu, L.; Liu, G.; Mao, Y.; Dong, X.; Jia, X.; Zhang, F.; Zhang, S.; Yang, F.; Wang, Z.; Peng, Q.; Shi, Y.; Hu, J.; Xiang, T.; Chen, X.; Xu, Z.; Chen, C.; Zhou, X. J. Orbital Origin of Extremely Anisotropic Superconducting Gap in Nematic Phase of FeSe Superconductor. *Phys. Rev. X* **2018**, *8*, 031033.

(66) Rømer, A. T.; Hirschfeld, P. J.; Andersen, B. M. Raising the Critical Temperature by Disorder in Unconventional Superconductors Mediated by Spin Fluctuations. *Phys. Rev. Lett.* **2018**, *121*, 027002.

(67) Yao, C.; Ma, Y. Superconducting materials: Challenges and opportunities for large-scale applications. *iScience* **2021**, *24*, 102541.

(68) Hacisalihoglu, M. Y.; Paris, E.; Joseph, B.; Yanmaz, E.; Saini, N. L. The nanoscale structure and unoccupied valence electronic states in $FeSe_{1-x}Te_x$ chalcogenides probed by X-ray measurements. *Phys. Chem. Chem. Phys.* **2015**, *17*, 18131−18137.

(69) Joseph, B.; Iadecola, A.; Puri, A.; Simonelli, L.; Mizuguchi, Y.; Takano, Y.; Saini, N. L. Evidence of local structure inhomogeneity in FeSe1-xTex from extended x-ray absorption fine structure. *Phys. Rev. B* **2010**, *82*, 020502.

(70) Iadecola, A.; Joseph, B.; Puri, A.; Simonelli, L.; Mizuguchi, Y.; Testemale, D.; Proux, O.; Hazemann, J.-L.; Takano, Y.; Saini, N. L. Random alloy-like local structure of Fe(Se, S)$_{1-x}$Te$_x$ superconductors revealed by extended X-ray absorption fine structure. *J. Phys.: Condens. Matter* **2011**, *23*, 425701.

(71) Saini, N. L. Nanoscale structure and atomic disorder in the iron-based chalcogenides. *Sci. Technol. Adv. Mater.* **2013**, *14*, 014401.

CAS BIOFINDER DISCOVERY PLATFORM™
STOP DIGGING THROUGH DATA —START MAKING DISCOVERIES
CAS BioFinder helps you find the right biological insights in seconds
Start your search
CAS
A division of the American Chemical Society

BOOK OF ABSTRACTS

ADVANCES
IN SOLID STATE PHYSICS
AND NEW MATERIALS

ДОСТИГНУЋА У ФИЗИЦИ ЧВРСТОГ СТАЊА И НОВИХ МАТЕРИЈАЛА

30 година Центра за физику чврстог стања и нове материјале Института за физику у Београду

ADVANCES IN SOLID STATE PHYSICS AND NEW MATERIALS

30 years of the Center for Solid State Physics and New Materials at the Institute of Physics Belgrade

19 - 23 May 2025
Belgrade, Serbia

Anisotropic Strain Response in FeSe

A. Milosavljević[a], J. Blagojević[a], T. Belojica[a], B. Višić[a], S. Djurdjić Mijin[a, b], M. Opačić[a], A. Šolajić[a], J. Pešić[a], A. Wang[c], C. Petrovic[c, d, e], R. Hackl[f, g] and N. Lazarević[a]

[a]*Institute of Physics Belgrade, University of Belgrade, Pregrevica 118, 11080 Belgrade, Serbia*
[b]*Departamento de Fisica de Materiales, Facultad de Ciencias, Universidad Autonoma de Madrid, 28049 Madrid, Spain*
[c]*Condensed Matter Physics and Material Science Department, Brookhaven National Laboratory, Upton, NY 11973-5000, USA*
[d]*Shanghai Advanced Research in Physical Sciences (SHARPS), Shanghai 201203, China*
[e]*Department of Nuclear and Plasma Physics, Vinca Institute of Nuclear Sciences, University of Belgrade, Belgrade 11001, Serbia*
[f]*School of Natural Sciences, Technische Universität München, Garching 85748, Germany*
[g]*IFW Dresden, Helmholtzstrasse 20, Dresden 01069, Germany*

Abstract.

Unconventional superconductivity often arises in materials with complex interactions, where competing ordered states such as magnetism, nematicity, and superconductivity, interact and sometimes overlap, making their nature elusive. Among iron-based superconductors, the isostructural FeSe and FeS may appear similar but they differ significantly in their physical properties. While FeSe undergoes a nematic and structural phase transition, FeS shows no structural transition even at the lowest temperatures, with its critical temperature (T_c) halved compared to FeSe. Interestingly, substituting selenium with sulfur in FeSe suppresses the nematic transition temperature to zero near a quantum critical point (QCP), which coincides with a significant drop in T_c. It has been suggested that while spin-fluctuations dominate below the QCP and significantly affect electron-phonon interactions, nematic fluctuations become prominent above the QCP. Here, we present a detailed Raman scattering study of FeSe under uniaxial strain applied along two high-symmetry crystallographic directions, ⟨110⟩ and ⟨100⟩, to investigate how symmetry-breaking perturbations affect its lattice dynamics. Our results reveal a pronounced anisotropy in the phonon response to strain: orthorhombic distortion along the ⟨110⟩ direction leads to a moderate narrowing of the temperature window over which phonon anomalies occur, while strain along ⟨100⟩ which introduces rhombohedral distortion, results in a significant broadening of the temperature range over which phonon mode splitting, and energy and linewidth anomalies are observed. We find that the fully symmetric A_{1g} phonon mode is particularly sensitive to symmetry-breaking perturbations, while the B_{1g} phonon mode remains largely unaffected.

*This research was supported by the Science Fund of the Republic of Serbia, 10925, Dynamics of CDW transition in strained quasi-1D systems - DYNAMIQS

Raman Signatures Of Instabilities In $InSiTe_3$

T. Belojica[a], A. Milosavljević[a], S. Djurdjić Mijin[ba], J. Blagojević[a], A. Šolajić[a], J. Pešić[a], B. Višić[a], V. Damljanović[a], M. O. Ogunbunmi[c], S. Bobev[cd], Yu Liu[d], C. Petrovic[def], Z. Popović[g], R. Hackl[hi], and N. Lazarević[a]

[a]Institute of Physics Belgrade, University of Belgrade, Pregrevica 118, 11080 Belgrade, Serbia
[b]Departamento de Fisica de Materiales, Facultad de Ciencias, Universidad Autónoma de Madrid, 28049 Madrid, Spain
[c]Departament of Chemistry and Biochemistry, University of Delaware, Newark, Delaware 19716, USA
[d]Condensed Matter Physics and Materials Science Departament, Brookhaven National Laboratory, Upton, NY 11973-5000, USA
[e]Department of Nuclear and Plasma Physics, Vinca Institute of Nuclear Sciences, University of Belgrade, Belgrade 11001, Serbia
[f]Shanghai Advanced Research in Physical Sciences (SHARPS), Shanghai 201203, China
[g]Serbian Academy of Sciences and Arts, Knez MIhailova35, 11000 Belgrade, Serbia
[h]School of Natural Sciences, Technische Universität München, Garching 85748, Germany
[i]IFW Dresden, Helmholtzstrasse 20, Dresden 01069, Germany

Abstract. Layered van der Waals materials have gained considerable interest for their unique physical properties, yet $InSiTe_3$ remains largely unexplored due to uncertainties surrounding its crystal structure. In this work, we present a comprehensive experimental and theoretical investigation of $InSiTe_3$, confirming a rhombohedral structure with $P\bar{3}$ space group symmetry via single-crystal X-ray diffraction. Polarization-resolved Raman scattering reveals nine out of ten Raman-active modes expected for this symmetry, further validating the structural assignment. Beyond conventional phonon behavior, we identify strong anharmonicity and the emergence of a self-organized coherent phonon state associated with a high-energy A_g mode near 500 cm^{-1}. Analysis of phonon-phonon coupling parameters indicates that A_g modes exhibit coupling strengths up to eight times greater than E_g modes. Temperature-dependent Raman measurements from 80 to 300 K reveal notable changes in A_g mode intensities around 200 K and the appearance of broad spectral features in the phonon gap region, attributed to overtone excitations. Our findings point to an intrinsic lattice instability in $InSiTe_3$, driven by strong anharmonic interactions. However, further studies are required to fully uncover the microscopic origin of these instabilities and their implications for the material's physical properties.

*This research was supported by the Science Fund of the Republic of Serbia, 10925, Dynamics of CDW transition in strained quasi-1D systems – DYNAMIQS

Symmetry-Resolved Raman Study of Temperature-Induced Phonon Anomalies in $ZrTe_5$

Ana Kanjevac[a], Ana Milosavljević[a], Emil Božin[a,b], Jasmina Lazarević[a],
Jovan Blagojević[a], Qiang Li[c,d] and Nenad Lazarević[a]

[a] *Institute of Physics Belgrade, University of Belgrade, Pregrevica 118, 11080 Belgrade, Serbia*
[b] *Computational Science Initiative, Brookhaven National Laboratory, Upton, NY 11973, USA*
[c] *Condensed Matter Physics and Materials Science Department, Brookhaven National Laboratory, Upton, NY, USA*
[d] *Department of Physics and Astronomy, Stony Brook University, Stony Brook, NY, USA*

Abstract. Zirconium pentatelluride ($ZrTe_5$) has attracted considerable attention in the condensed matter community due to its temperature-dependent band gap variations. Additionally, it has been proposed that $ZrTe_5$ lies near a phase boundary between strong (STI) and weak topological insulator (WTI) phases, as well as undergoing an electronic topological (Lifshitz) transition. Depending on the sample and synthesis conditions, the Lifshitz transition temperature varies between 50 and 150 K [1–3]. In this study, we performed Raman spectroscopic analysis of $ZrTe_5$ single crystals over a temperature range of 76 to 300 K. The measurements were carried out in symmetry-resolved scattering geometries using parallel and cross polarization configurations along the principal crystallographic directions. In this setup, only phonon modes of A_g and B_{2g} symmetries are allowed in the respective configurations. The results reveal pronounced temperature-dependent behavior, including variations in phonon linewidths and peak positions. Notably, at lower temperatures, certain phonon modes exhibit asymmetric line shapes that are well described by the Fano profile. As the temperature increases, these features gradually evolve into symmetric peaks. This behavior indicates a strong coupling between lattice vibrations and electronic excitations in $ZrTe_5$. Our Raman scattering results provide valuable insight into the phonon dynamics and electron–phonon coupling in $ZrTe_5$, contributing to a deeper understanding of its fundamental properties.

REFERENCES

1. Zhang, J., Wang, C., Wang, J., et al. “Signatures of a Lifshitz Transition in the Mixed Dirac-Weyl Semimetal $ZrTe_5$,” Phys. Rev. B 108, L041202 (2023).
2. Lozano, P. M., et al. “Anomalous Hall Effect at the Lifshitz Transition in $ZrTe_5$,” Phys. Rev. B 106, L081124 (2022).
3. Zhang, Y., Xu, C., Song, Y., et al. “Electronic Evidence of Temperature-Induced Lifshitz Transition and Topological Nature in $ZrTe_5$” Nat. Commun. 8, 15512 (2017).

*This research was supported by the Science Fund of the Republic of Serbia, 10925, Dynamics of CDW transition in strained quasi-1D systems - DYNAMIQS

Phonon Signatures of Instabilities in van der Waals material $InSiTe_3$

Jasmina Lazarević[1]
Ana Milosavljević[1], Sanja Djurdjić Mijin[1,2], Tea Belojica[1], Jovan Blagojević[1], Andrijana Šolajić[1], Jelena Pešić[1], Bojana Višić[1], Vladimir Damljanović[1], Michael O. Ogunbunmi[3], Svilen Bobev[3,4], Yu Liu[4], Cedomir Petrovic[4,5,6], Zoran V. Popović[7], and Nenad Lazarević[1]

[1] Institute of Physics Belgrade, University of Belgrade, Pregrevica 118, 11080 Belgrade, Serbia
[2] Departamento de Fisica de Materiales, Facultad de Ciencias, Universidad Autnoma de Madrid, 28049 Madrid, Spain
[3] Department of Chemistry and Biochemistry, University of Delaware, Newark, Delaware 19716, U.S.A.
[4] Condensed Matter Physics and Materials Science Department, Brookhaven National Laboratory, Upton, NY 11973-5000, USA
[5] Shanghai Advanced Research in Physical Sciences (SHARPS), Shanghai 201203, China
[6] Department of Nuclear and Plasma Physics, Vinca Institute of Nuclear Sciences, University of Belgrade, Belgrade 11001, Serbia
[7] Serbian Academy of Sciences and Arts, Knez Mihailova 35, 11000 Belgrade, Serbia
jasmina.lazarevic@ipb.ac.rs

Although van der Waals materials are widely studied for their unique properties and applications, $InSiTe_3$ remains relatively neglected despite being synthesized over 30 years ago, especially when compared to the extensive research on related compounds like $CrSiTe_3$ and $CrGeTe_3$. Here, we present a detailed experimental and theoretical investigation of this van der Waals material. Single-crystal X-ray diffraction reveals the rhombohedral crystal symmetry of InSiTe3, described with the $P\bar{3}$ space group. Polarization-dependent inelastic light scattering experiments further validate the symmetry and reveal pronounced anharmonicity in $InSiTe_3$. Namely, in addition to the symmetry predicted Raman active modes, which show excellent agreement with DFT calculations, the spectra exhibit unexpected features; tripling of a localized high-energy A_g mode at approximately 500 cm^{-1}. For E_g modes the extracted phonon-phonon coupling constants indicate moderate anharmonicity. However, for A_g modes, the coupling strength increases dramatically, reaching values up to ten times higher than those of the doubly degenerate modes. The intensities of the analysed A_g modes display anomalous behaviour with increasing the temperature, particularly around 200 K. Notably, at this same temperature, higher-order overtone excitations emerge within the gap of the calculated phonon density of states. Having in mind that phonons couple to various degrees of freedom, these interactions leave a distinct fingerprint on their behaviour. While our findings highlight these instabilities, its origin lies beyond the scope of this research.

*This research was supported by the Science Fund of the Republic of Serbia, 10925, Dynamics of CDW transition in strained quasi-1D systems - DYNAMIQS

Exploring the Interplay of Ordered and Fluctuating States in Fe(Se:S): The Role of Internal Parameters and Uniaxial Strain

Ana Milosavljević[1]
Jovan Blagojević[1], Tea Belojica[1], Bojana Višić[1], Sanja Djurdjić Mijin[1, 2], Marko Opačić[1], Andrijana Šolajić[1], Jelena Pešić[1], Aifeng Wang[3], Cedomir Petrovic[3, 4, 5] and Nenad Lazarević[1]

[1]*Institute of Physics Belgrade, University of Belgrade, Pregrevica 118, 11080 Belgrade, Serbia*
[2]*Departamento de Fisica de Materiales, Facultad de Ciencias, Universidad Autonoma de Madrid, 28049 Madrid, Spain*
[3]*Condensed Matter Physics and Material Science Department, Brookhaven National Laboratory, Upton, NY 11973-5000, USA*
[4]*Shanghai Advanced Research in Physical Sciences (SHARPS), Shanghai 201203, China*
[5]*Department of Nuclear and Plasma Physics, Vinca Institute of Nuclear Sciences, University of Belgrade, Belgrade 11001, Serbia*
ana.milosavljevic@ipb.ac.rs

Unconventional superconductivity often arises in materials with complex interactions, where competing ordered states such as magnetism, nematicity, and superconductivity, interact and sometimes overlap, making their nature elusive. Among iron-based superconductors, the isostructural FeSe and FeS may appear similar at first glance but differ significantly in their physical properties. While FeSe undergoes a nematic and structural phase transition, FeS does not exhibit a structural transition even at the lowest temperatures, with its critical temperature (Tc) halved compared to FeSe. Interestingly, by substituting selenium with sulfur in FeSe, the nematic phase transition temperature can be suppressed to zero near a quantum critical point (QCP), resulting in a significant drop in T_c [1, 2]. It has been suggested that while spin-fluctuations dominate below the QCP and significantly affect electron-phonon interactions, nematic fluctuations become prominent above the QCP [3]. Given their exceptional sensitivity to variations in local crystal structure, iron-chalcogenides are ideal candidates for studying the interplay between ordered and fluctuating states through manipulation of internal parameters (doping) and external ones, such as uniaxial strain. Here, we present a study of all types of excitations, including phonons, charge, and spin fluctuations in Fe(S:Se) using inelastic light scattering experiments. Finally, we analyse the evolution of lattice dynamics as a function of uniaxial tensile strain along the Fe-Fe bond direction (that contains the nematic component) and along the direction diagonal to it in FeSe.

References

[1] A. Wang, A. Milosavljevic, et al., *Inorganic Chemistry 61* (29), 11036-11045 (2022)
[2] N. Lazarević, A. Baum, A. Milosavljević, et al., *Phys. Rev. B* 106, 094510 (2023)
[3] S. Neto, et al., *Nature Phys.* 21, 89–96 (2025)

*This research was supported by the Science Fund of the Republic of Serbia, 10925, Dynamics of CDW transition in strained quasi-1D systems - DYNAMIQS

INSTITUTE OF TECHNICAL SCIENCES OF SASA
MATERIALS RESEARCH SOCIETY OF SERBIA

Programme and the Book of Abstracts

TWENTY-THIRD YOUNG RESEARCHERS' CONFERENCE MATERIALS SCIENCE AND ENGINEERING

Belgrade, December 3 – 5, 2025

7-1

Raman signatures of CDW induced phonon folding in $TaTe_4$

Tea Belojica[1], Jovan Blagojević [1], Marko Opačić[1], Vladimir Damljanović[1], Jelena Pešić[1], Andrijana Šolajić[1], Cedomir Petrovic[2,3,4,5], Ana Milosavljević[1], Nenad Lazarević[1]

[1]*Institute of Physics Belgrade, University of Belgrade, Pregrevica 118, 11080 Belgrade, Serbia*
[2]*Condensed Matter Physics and Materials Science Department, Brookhaven National Laboratory, Upton, NY 11973-5000, USA*
[3]*Shanghai Advanced Research in Physical Sciences (SHARPS), Shanghai 201203, China*
[4]*Department of Nuclear and Plasma Physics, Vinca Institute of Nuclear Sciences, University of Belgrade, Belgrade 11001, Serbia*
[5]*Center for High Pressure Science & Technology Advanced Research (HPSTAR), Beijing 100094, China*

$TaTe_4$ is a quasi-one-dimensional transition metal telluride known for its commensurate charge density wave (CDW) state and complex lattice modulation below 450 K. In low-dimensional materials, CDW is mostly driven by strong electron–phonon coupling and give rise to complex lattice distortions and collective electronic order. Despite numerous studies, the detailed crystal structure and vibrational properties associated with the CDW state in $TaTe_4$ have yet to be fully characterized. Using polarization-resolved Raman spectroscopy in the temperature range between 100 and 300 K, we investigated the vibrational properties of $TaTe_4$ within its commensurate CDW phase. In total, seventeen modes were observed, exceeding the ten Raman-active ones expected in the high-temperature phase. The appearance of additional modes indicates zone folding consistent with the $2a \times 2a \times 3c$ CDW superstructure. Comparison with DFT-calculated phonon energies enabled assignment of the original zone-center modes of the high-temperature structure and the additional folded modes activated by the CDW superstructure. Beyond the discrete phonon lines, a broad continuum centered around 150 cm^{-1} was detected and attributed to two-phonon scattering from acoustic branches activated by zone folding. These findings provide direct experimental evidence of phonon folding driven by CDW modulation and underscore the intricate coupling between electronic and lattice degrees of freedom in $TaTe_4$. This study constitutes the first polarization-resolved Raman investigation of $TaTe_4$, offering new insight into the symmetry and temperature evolution of folded phonons in this quasi-low-dimensional CDW system.

Acknowledgements: This research was supported by the Science Fund of the Republic of Serbia, 10925, Dynamics of CDW transition in strained quasi-1D systems – DYNAMIQS. The authors acknowledge funding provided by the Institute of Physics Belgrade, through the grant by the Ministry of Science, Technological Development and Innovation of the Republic of Serbia.

7-3

Evidence of temperature-induced lifshitz transition in topological material $ZrTe_5$

Ana Kanjevac[1], Ana Milosavljević[1], Jasmina Lazarević[1], Jovan Blagojević[1], Qiang Li [2,3]
Emil S Božin[1,2], Nenad Lazarević[1]

[1]Center for Solid State Physics and New Materials, Institute of Physics Belgrade, University of Belgrade, Pregrevica 118, 11080 Belgrade, Serbia
[2]Condensed Matter Physics and Materials Science Department, Brookhaven National Laboratory, Upton, New York 11973-5000, USA
[3]Department of Physics and Astronomy, Stony Brook University, Stony Brook, New York, USA

Topological Dirac semimetal $ZrTe_5$ has been the subject of extensive experimental and theoretical investigation, as it lies near the boundary between strong and weak topological insulator phases and hosts a Dirac semimetal state at the electronic (Lifshitz) transition. The reported Lifshitz transition temperature in $ZrTe_5$ varies between 50 and 150 K, depending on sample quality and synthesis conditions. In this study, we performed Raman spectroscopic analysis of $ZrTe_5$ single crystals over a temperature range from 40 to 300 K. The measurements were carried out in symmetry-resolved scattering geometries using parallel and cross polarization configurations along the principal crystallographic directions, within the *ac* plane, allowing observation of six A_g and two B_{2g} phonon modes. Our results reveal that all A_g modes exhibit changes in energies and linewidths within the temperature range of the proposed topological transition. In the parallel polarization configuration, peak asymmetry is observed for four of the six A_g modes, while in the crossed polarisation configuration, only the first B_{2g} mode exhibits a similar feature. These asymmetric line shapes are well described by the Fano profile, suggesting a significant electron–phonon interaction. Our Raman scattering results provide insight into the coupling between lattice vibrations and electronic structure and its temperature-driven topological behavior.

Acknowledgements: This research is financed by HIP-2D-QM Project. This project received funding from the European Union's Horizon Europe research and innovation programme under grant agreement NO 101185375. This research was supported by the Science Fund of the Republic of Serbia, 10925, Dynamics of CDW transition in strained quasi-1D systems – DYNAMIQS. The authors acknowledge funding provided by the Institute of Physics Belgrade, through the grant by the Ministry of Science, Technological Development and Innovation of the Republic of Serbia.

7-4

Raman study of magnetic transitions in Mn_3Sn_2

Gorana Madžarević[1], Ana Kanjevac[2], Jovan Blagojević[2], Jelena Pešić[2], Ana Milosavljević[2], Nenad Lazarević[2]

[1]Faculty of Physics, University of Belgrade, Belgrade, Serbia
[2]Center for Solid State Physics and New Materials, Institute of Physics Belgrade, University of Belgrade, Pregrevica 118, 11080 Belgrade, Serbia

Manganese stannide Mn_3Sn_2 has recently emerged as a promising material for exploring the interplay between magnetism and topological electronic structure, with its multiple magnetic transitions providing an ideal setting to study spin, lattice, and electronic properties using Raman spectroscopy. The compound crystallizes in the orthorhombic Pnma structure and exhibits multiple magnetic transitions between 180 K and 270 K, along with theoretically predicted nodal lines and nodal surfaces near the Fermi level. In this study, we performed temperature-dependent Raman spectroscopic measurements of Mn_3Sn_2 single crystals in the range from 76 K to 300 K using circular polarization configurations to minimize orientation dependence. Several Raman active A_g phonon modes were clearly observed and analyzed as a function of temperature. Pronounced anomalies in phonon energies and linewidths are detected near the antiferromagnetic ordering temperature (~192 K) and two successive ferromagnetic transitions at ~227 K and ~260 K, indicating significant spin-phonon coupling. At lower temperatures, around 80 K, distinct modifications in phonon profiles coincide with the sign reversal of the Seebeck coefficient, suggesting sensitivity of the lattice dynamics to changes in the electronic transport regime. These findings point to a complex but temperature-dependent coupling among the lattice, magnetic, and electronic subsystems in Mn_3Sn_2.

Acknowledgements*:* This research is financed by HIP-2D-QM Project. This project received funding from the European Union’s Horizon Europe research and innovation programme under grant agreement NO 101185375. The authors acknowledge funding provided by the Institute of Physics Belgrade, through the grant by the Ministry of Science, Technological Development and Innovation of the Republic of Serbia.

ÉCOLE DE
PHYSIQUE DES HOUCHES

UGA Université Grenoble Alpes
cnrs
cea
ENS DE LYON
GRENOBLE INP UGA
WILHELM UND EL
HERAEUS-STIFTU

28th September - 3rd October 2025
Les Houches - France

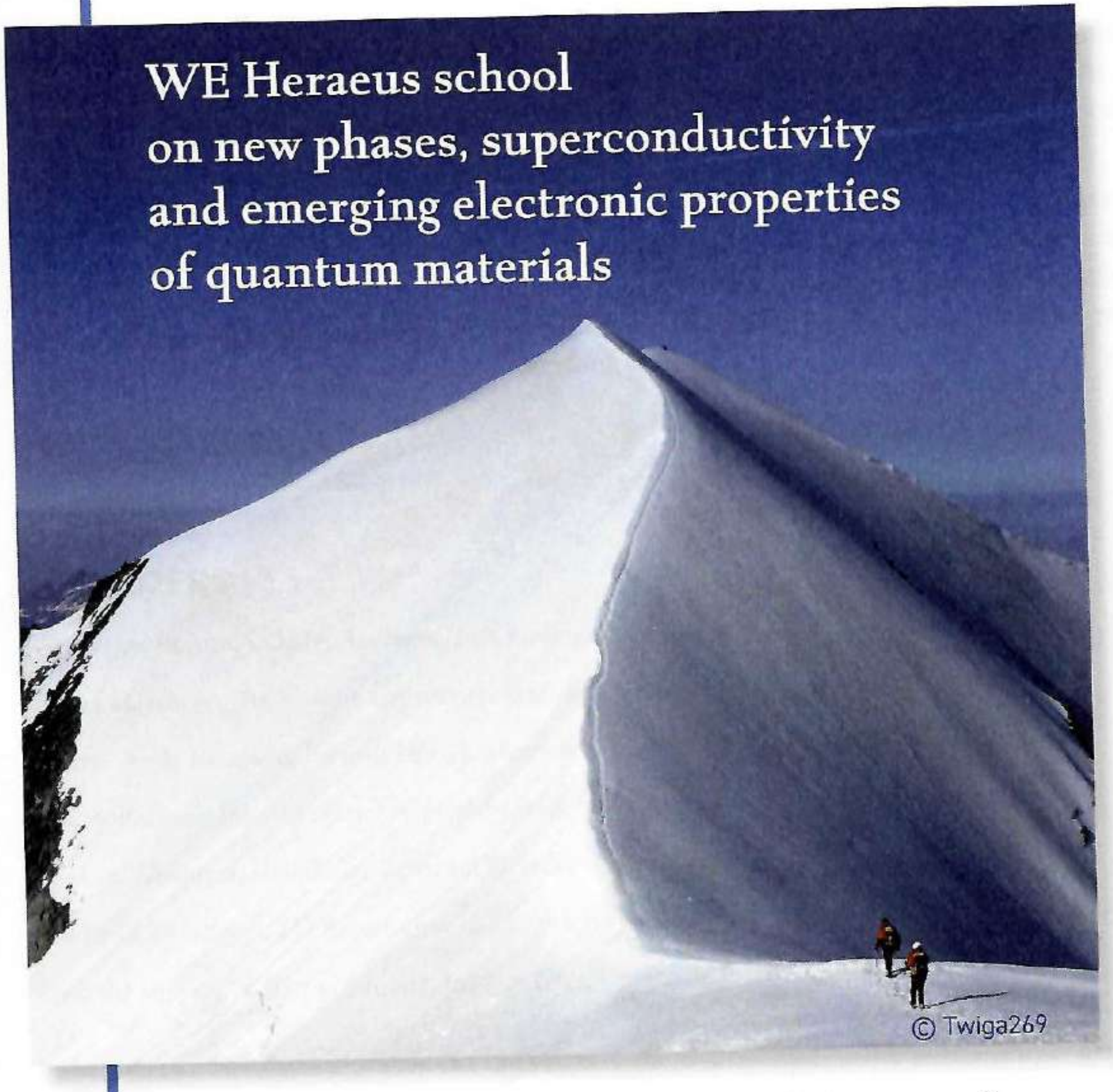

WE Heraeus school on new phases, superconductivity and emerging electronic properties of quantum materials

© Twiga269

https://fermi-sces2025.grenoble.cnrs.fr

cnrs
Université franco-allemande
Deutsch-Französische Hochschule
ct.qmat
Complexity and Topology in Quantum Matter
EMFL
European Magnetic Field Lab

LES HOUCHES – WE HERAEUS SCHOOL ON NEW PHASES, SUPERCONDUCTIVITY AND EMERGING ELECTRONIC PROPERTIES OF QUANTUM MATERIALS

Exploring, understanding, and describing materials with strong electronic Coulomb correlations remain among the big challenges of modern condensed-matter physics. Well-known examples of such systems are transition-metal oxides, metals containing lanthanide or actinide atoms, and organic conductors. At low temperatures, these materials exhibit novel phenomena such as metal-to-insulator transitions, heavy-fermion behavior, unconventional superconductivity, unusual magnetism, stripe and nematic orders as well as pronounced deviations from the typical universal metallic behavior. Superconductivity and ferromagnetism are not only found to coexist but even to cooperate. A central goal of the research, thereby, is to develop, on the theoretical side, a quantitative microscopic understanding of the possible complex states and their interactions as well as, on the experimental side, to characterize them using the broadest possible range of measurement methods.

The aim of the school is to deepen the understanding of the physics of quantum materials with a focus on superconductivity. The lectures will address materials growth, measurement techniques, experimental results, theory, computation, and general understanding. We attempt to provide a comprehensive overview of the fundamental ideas, the current status, the recent developments, and the perspective future directions in the field.

ORGANIZERS

- Sébastien Burdin, LOMA, Université de Bordeaux, France
- Elena Hassinger, Technische Universität Dresden, Germany
- Marie-Aude Méasson, Institut Néel, Université Grenoble Alpes, CNRS, Grenoble, France
- Pierre Rodière, Institut Néel, Université Grenoble Alpes, CNRS, Grenoble, France
- Jochen Wosnitza, Helmholtz-Zentrum Dresden-Rossendorf, Germany
- Gertrud Zwicknagl, TU Braunschweig, Braunschweig, Germany

With the support of Alyssa Arnoux, Institut Néel, Université Grenoble Alpes, CNRS, Grenoble, France

List of participants

ALEX Sonu George	Charles University, Prague - Czech Republic; alex@fzu.cz
ANSELMI Gabriele	University of Rome "Tor Vergata", Rome - Italy; gabriele.anselmi.01@alumni.uniroma2.eu
ARABI Soroush	Karlsruhe Institute of Technology, Karlsruhe - Germany; soroush.arabi@kit.edu
ARFAOUI Mohamed Khaled	Pheliqs, CEA Grenoble, Grenoble - France; Khaledcampus.arfaoui@gmail.com
AUFFRAY Elisa	Paris Saclay University, Orsay - France; elisa.auffray@universite-paris-saclay.fr
BARON Antoine	Institut Néel & Karlsruhe Institute of Technology, Karlsruhe - Germany; antoine.baron@neel.cnrs.fr
BERGE Siri Alva	University of St Andrews, St Andrews - United Kingdom; sb450@st-andrews.ac.uk
BISSET Rebecca	University of St Andrews, St Andrews - United Kingdom; rb254@st-andrews.ac.uk
BLAGOJEVIĆ Jovan	Institute of Physics Belgrade, Belgrade - Serbia; jovanb@ipb.ac.rs
BÖHMER Anna	RUB Bochum, Bochum - Germany; boehmer@physik.rub.de
BRISON Jean Pascal	CEA , Grenoble - France; jean-pascal.brison@cea.fr
BURDIN Sébastien	LOMA, Bordeaux - France; sebastien.burdin@u-bordeaux.fr
CHAU Chun Wang	University of Cambridge, Cambridge - United Kingdom; cwc61@cam.ac.uk
COCCHI Chiara	HFML-FELIX, Radboud University, Nijmegen - the Netherlands; chiara.cocchi@ru.nl
DOMANSKI Lukasz	Cavendish Laboratory, University of Cambridge, Cambridge - United Kingdom; lmd81@cam.ac.uk
FROLOV Aleksei	Max Planck Institute for Chemical Physics of Solids, Dresden - Germany; Aleksei.Frolov@cpfs.mpg.de
GALLO--FRANTZ Antoine	Institut Néel, Grenoble - France; gallofrantz.antoine@gmail.com
GHIHOR Anamaria	Max Planck Institute for Chemical Physics of Solids, Dresden - Germany; anamaria.ghihor@cpfs.mpg.de
GRAGLIA Johan	LNCMI, Toulouse - France; johan.graglia@lncmi.cnrs.fr
GUO Tingwen	Laboratoire des Solides Irradiés, Ecole Polytechnique, Palaiseau - France; tingwen.guo@polytechnique.edu

HASSINGER Elena	Technische Universität Dresden, Dresden - Germany ; elena.hassinger@tu-dresden.de
HUSSTEDT Freya	Dresden High Magnetic Field Laboratory, Dresden - Germany; f.husstedt@hzdr.de
KRELLNER Cornelius	Universität Frankfurt, Frankfurt - Germany; krellner@physik.uni-frankfurt.de
KURTANIDZE Ana	TU Dresden,HZDR, Dresden - Germany; a.kurtanidze@hzdr.de
LAMOUCHE Nils	Université de Montréal, Montréal - Canada; nils.lamouche@umontreal.ca
LE TACON Matthieu	KIT Karlsruhe, Karlsruhe - Germany; Matthieu.LeTacon@kit.edu
LECERF Meghan	Laboratoire Albert Fert - Thales, Palaiseau - France; meghan.lecerf@cnrs-thales.fr
LEPETIT Marie Bernadette	Institut Néel & ILL, Grenoble - France; marie-bernadette.lepetit@neel.cnrs.fr
MCCOLLAM Alix	University College Cork, Cork - Ireland; AMccollam@ucc.ie
MÉASSON Marie Aude	Institut Néel, CNRS, Grenoble - France; marie-aude.measson@neel.cnrs.fr
MENON Lorenzo	Institut Néel, Grenoble - France; lorenzo.menon@neel.cnrs.fr
MEPLAN Macha	Pheliqs, CEA Grenoble, Grenoble - France; macha.meplan@etu.univ-grenoble-alpes.fr
MIGNANI Niccolò	Dipartimento di Fisica, Politecnico di Milano, Milano - Italy.; niccolo.mignani@polimi.it
MILOSAVLJEVIĆ Ana	Institute of Physics Belgrade, University of Belgrade, Belgrade - Serbia; anam@ipb.ac.rs
MISTONOV Alexander	TU Dresden, Dresden - Germany; alexander.mistonov@tu-dresden.de
MITREVSKI Vojo	Saints Cyril and Methodius University in Skopje, Faculty of Natural Sciences and Mathematics, Skopje - Macedonia; vojo.mitrevski@gmail.com
NADUVILE THADATHIL Sajal	Dresden High Magnetic Field Laboratory, HZDR, Dresden - Germany; s.naduvile-thadathil@hzdr.de
OBLADEN Paula	Universidad Autónoma de Madrid, Madrid - Spain ; paula.obladen@uam.es
PAULESCU Ioana	University of Oxford, Oxford - United Kingdom; ioana.paulescu@physics.ox.ac.uk

Strain-Tuned Lattice Signatures of Fluctuating Phases in FeSe

Ana Milosavljević[1], Jovan Blagojević[1], Tea Belojica[1], Bojana Višić[1], Sanja Djurdjić Mijin[1,2], Marko Opačić[1], Andrijana Šolajić[1], Jelena Pešić[1], Aifeng Wang[3], Cedomir Petrovic[3,4,5], Rudi Hackl[6, 7] and Nenad Lazarević[1]

[1]*Institute of Physics Belgrade, University of Belgrade, Pregrevica 118, 11080 Belgrade, Serbia*
[2]*Departamento de Fisica de Materiales, Facultad de Ciencias, Universidad Autonoma de Madrid, 28049 Madrid, Spain*
[3]*Condensed Matter Physics and Material Science Department, Brookhaven National Laboratory, Upton, NY 11973-5000, USA*
[4]*Shanghai Advanced Research in Physical Sciences (SHARPS), Shanghai 201203, China*
[5]*Department of Nuclear and Plasma Physics, Vinca Institute of Nuclear Sciences, University of Belgrade, Belgrade 11001, Serbia*
[6]*School of Natural Sciences, Technische Universität München, Garching 85748, Germany*
[7]*IFW Dresden, Helmholtzstrasse 20, Dresden 01069, Germany*

Unconventional superconductivity often emerges in materials where different phases compete and overlap, making their nature elusive. Among iron-based superconductors, FeSe and its isostructural counterpart FeS highlight this complexity: while FeSe undergoes a nematic and structural phase transition, FeS shows no such transition, with its critical temperature (T_c) reduced by about half. Substituting Se with S in FeSe suppresses the nematic transition temperature to zero near a quantum critical point (QCP). We present a Raman scattering study addressing chemical substitution ($FeSe_{1-x}S_x$, $0 \leq x \leq 1$) and uniaxial strain applied to FeSe along the ⟨110⟩ and ⟨100⟩ crystallographic directions. In the substitution series, all types of excitations including phonons, spins, and electronic degrees of freedom were tracked as functions of temperature and scattering geometry. The Fe-related B_{1g} phonon evolves continuously across the entire range, whereas A_{1g} phonon exhibits discontinuities, disappearing above QCP and reemerging at much higher energy near x=0.69. The disappearance of the two-magnon around 500 cm^{-1} at $x > 0.23$ coincides with abrupt changes in the A_{1g} lattice response, underscoring a strong link between lattice and spin dynamics. Further, the low-energy fluctuation mode reaches the maximum at the nematostructural transition, tracking the phase boundary. Strain-dependent studies on FeSe reveal anisotropic behavior. Distortion along ⟨110⟩ narrows, while strain along ⟨100⟩ broadens the temperature window where A_{1g} mode splitting occurs. Notably, the A_{1g} phonon mode is highly sensitive to such symmetry-breaking perturbations, whereas the B_{1g} mode remains largely unaffected.

---

*This research was supported by the Science Fund of the Republic of Serbia, 10925, Dynamics of CDW transition in strained quasi-1D systems - DYNAMIQS

RÅC INTERNATIONAL SUMMER SCHOOL 2025

Advanced
Materials Design
at X-ray and
Neutron Facilities

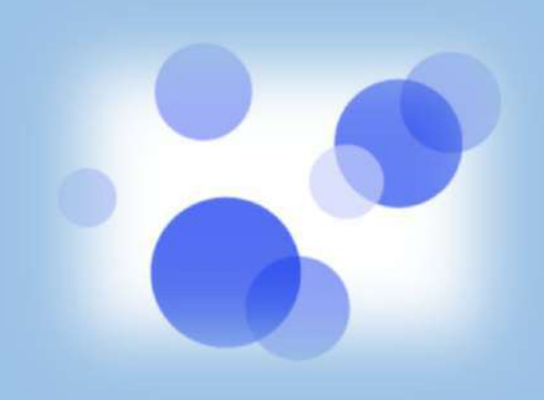

Diffraction and Spectroscopy in Materials Science

August 24-31, 2025
Tallinn, Estonia

POSTER ABSTRACTS

Sponsored by:

Swedish Research Council

This twinning project "EXANST" has received funding from the European Union's Horizon Europe research and innovation programme under grant agreement No. 101159716

Federal Ministry of Research, Technology and Space

Ana Milosavljević
anam@ipb.ac.rs

Institute of Physics Belgrade, University of Belgrade, Serbia
Belgrade, Serbia

Research Associate

Fields of interest:
Raman scattering of strongly correlated electron systems; Fe-based superconductors, quasi low-dimensional materials

Strain-Tunable Fluctuations near the Pseudogap Regime in $ZrTe_3$

We investigate the effect of uniaxial strain and temperature on the Raman response of quasi-one-dimensional $ZrTe_3$, with strain applied along the *a*-axis, the direction along which the incommensurate charge density wave (CDW) forms.

In addition to the symmetry-allowed Raman modes observed in parallel polarization configuration, we detect the emergence of an additional peak in the temperature range centered around 200 K, coinciding with the known onset of the pseudo-gap. This mode becomes pronounced under compressive strain at lower temperatures and under tensile strain at higher temperatures, indicating a crossover in the dominant fluctuation regime.

Furthermore, a clear Fano-like asymmetry in the Raman phonon modes reveals strong electron–phonon coupling, particularly near the fluctuation regime. This behaviour arises from direct phonon–continuum interactions characteristic for CDW systems.

*This research was supported by the Science Fund of the Republic of Serbia, 10925, Dynamics of CDW transition in strained quasi-1D systems - DYNAMIQS

Volume 427 - 11th International Conference of the Balkan Physical Union (BPU11) - S06-CMPSP Condensed Matter Physics and Statistical Physics

Raman Spectroscopy Study of magnetic Quasi-two-dimensional materials

S. Djurdjic Mijin*, *A. Šolajić, A.M.M. Abeykoon, A. Milosavljević, M. Šćepanović, Y. Liu, J. Pešić, C. Petrovic, N. Lazarević and Z.V. Popović*

**: corresponding author*

Full text: Not available

How to cite

Metadata are provided both in *article* format (very similar to INSPIRE) as this helps creating very compact bibliographies which can be beneficial to authors and readers, and in *proceeding* format which is more detailed and complete.

Open Access

Copyright owned by the author(s) under the term of the Creative Commons Attribution-NonCommercial-NoDerivatives 4.0 International License.

TWENTY-SECOND YOUNG RESEARCHERS' CONFERENCE
MATERIALS SCIENCE AND ENGINEERING

December 4 – 6, 2024, Belgrade, Serbia

Program and the Book of Abstracts

Materials Research Society of Serbia
&
Institute of Technical Sciences of SASA

2024

6-2

Study of crystal phases and temperature dependence of $InSiTe_3$

T. Belojica[1], J. Blagojević[1], S. Djurđić Mijin[1,2], A. Šolajić[1], J. Pešić[1], B. Višić[1], V. Damljanović[1], M. O. Ogunbunmi[3], S. Bobev[3,4], Yu Liu[4], C. Petrovic[4,5,6], Z.V. Popović[7], A. Milosavljević[1], N. Lazarević[1]

[1]Center for Solid State Physics and New Materials, Institute of Physics Belgrade, University of Belgrade, Pregrevica 118, 11080 Belgrade, Serbia, [2]Departamento de Fisica de Materiales, Facultad de Ciencias,Universidad Autonoma de Madrid, 28049 Madrid, Spain, [3]Department of Chemistry and Biochemistry, University of Delaware, Newark, Delaware 19716, U.S.A., [4]Condensed Matter Physics and Materials Science Department, Brookhaven National Laboratory, Upton, NY 11973-5000, USA, [5]Shanghai Advanced Research in Physical Sciences (SHARPS), Shanghai 201203, China, [6]Department of Nuclear and Plasma Physics, Vinca Institute of Nuclear Sciences, University of Belgrade, Belgrade 11001, Serbia, [7]Serbian Academy of Sciences and Arts, Knez Mihailova 35, 11000 Belgrade, Serbia

In recent years, quasi-low-dimensional materials have attracted significant attention due to their distinctive properties and possible applications in nanoeletronics and spintronics. The material of a specific interest within this group is $InSiTe_3$. Unlike related compounds, such as $CrSiTe_3$ and $CrGeTe_3$, research results $InSiTe_3$ are limited, most likely due to the unclear nature of its crystal structure. Detailed experimental and theoretical investigation was conducted to determine the crystal structure of $InSiTe_3$. Inelastic light scattering experiment performed on the $InSiTe_3$ reveals presence of six ($3A_{1g} + 3E_g$) out of eight and seven ($5A_g + 2E_g$) out of ten Raman active modes for proposed $P\bar{3}1m$ and $P\bar{3}$ space groups, respectively. These findings suggest a coexistence of two trigonal crystal phases: a high symmetry one corresponding to $P\bar{3}1m$ and athe lower symmetry one that corresponds to $P\bar{3}$ space group. Additional exitations were detected in parallel scattering configuration; two broad features in the gap of PDOS that can be a consequence of to two-phonon processes and a third one, at about 500 cm^{-1} that might indicate local symmetry breaking at nano scale. Temperature dependent measurements from 80 K to 300 K show monotonous decrease in energy and increase in linewidth up to 200 K at which point discontinuities appear across all analyzed modes. However, this anomaly overcomes the scope of this research and remains an open question.

Abstract book of the International meeting on superconducting quantum materials and nanodevices

17 to 21 April 2023

Poster session I

Tuesday 18 April
I-5 Ana Milosavljević

EVOLUTION OF LATTICE, SPIN, AND CHARGE PROPERTIES ACROSS FeSe$_{1-x}$S$_x$ PHASE DIAGRAM

A. Milosavljević[1*], N. Lazarević[1], A. Baum[2,3], L. Peis[2,3], R. Stumberger[2,3], J. Bekaert[4], A. Šolajić[1], J. Pešić[1], Aifeng Wang[5], M. Šćepanović[1], A. M. Milinda Abeykoon[6], M. V. Milošević[4], C. Petrovic[7], Z. V. Popović[8], and R. Hackl[2,3,9]

[1]*Center for Solid State Physics and New Materials, Institute of Physics Belgrade, University of Belgrade, Pregrevica 118, 11080 Belgrade, Serbia*
[2]*Walther Meissner Institut, Bayerische Akademie der Wissenschaften, 85748 Garching, Germany*
[3]*Fakultät für Physik, Technische Universität München, 85478 Garching, Germany*
[4]*Department of Physics, University of Antwerp, Groenenborgerlaan 171, B-2020 Antwerp, Belgium*
[5]*School of Physics, Chongqing University, Chongqing 400044, China*
[6]*National Synchrotron Light Source II, Brookhaven National Laboratory, Upton, New York 11973, USA*
[7]*Condensed Matter Physics and Materials Science Department, Brookhaven National Laboratory, Upton, New York 11973-5000, USA*
[8]*Serbian Academy of Sciences and Arts, Kneza Mihaila 35, 11000 Belgrade, Serbia*
[9]*IFW Dresden, Helmholtzstr. 20, 01069 Dresden, Germany*

**Presenting author: anam@ipb.ac.rs*

Iron-based compounds are widely believed to host unconventional superconductivity. Among them in binary compound FeSe nematic and structural phase transition occurs simultaneously at 90 K and below 9 K superconductivity is observed. In isoelectronic FeS, structural phase transition is not detected down to the lowest temperatures. By substituting selenium with sulfur atoms by 20% a zero nematic phase transition temperature is reached suggesting the existence of quantum critical point (QCP). At this point T_c drops down to approximately 2 K [1]. In order to investigate in which extent the properties and other instabilities of FeSe and FeS are interrelated, the entire substitution range of the FeSe$_{1-x}$S$_x$ is studied by Raman scattering technique. Data were taken as a function of sulfur concentration x for $0 \leq x \leq 1$, of temperature and of scattering symmetry. All types of excitations including phonons, spins, and charges are analyzed. It is observed that the energy and linewidth of the Fe-related B_{1g} phonon mode vary continuously across the entire range. The A_{1g} mode disappears above $x = 0.23$ and reappears at much higher energy for $x = 0.69$. In a similar way the spectral features appearing at finite doping in A_{1g} symmetry vary discontinuously. The magnetic excitation at approximately 500 cm^{-1} disappears above $x = 0.23$ where the A_{1g} lattice excitations exhibit a discontinuous change in energy. The low-energy mode associated with fluctuations displays maximal intensity at the nematostructural transition and thus tracks the phase boundary [2].

[1] A. Wang, A. Milosavljevic, A. M. Milinda Abeykoon et al., Inorganic Chemistry 2022 61 (29), 11036-11045

[2] N. Lazarević, A. Baum, A. Milosavljević, et al., Phys. Rev. B 106, 094510

Friday 21 April
08:55-09:20 Jelena Pešić

EVOLUTION OF VIBRATIONAL MODES OF FeSe UNDER UNIAXIAL STRAIN

J. Pešić*, A. Šolajić, A. Milosavljević and N. Lazarević

Center for Solid State Physics and New Materials, Institute of Physics Belgrade, University of Belgrade,
Pregrevica 118, 11080 Zemun, Serbia

**Presenting author: yelena@ipb.ac.rs*

Application of strain is one of the effective ways to engineer the various properties of materials. Iron-based superconductors are suitable materials to study the strain dependence on physical properties due to their high sensitivity to variations in the local crystal structure. Among the iron-based superconductor family, FeSe is prominent example of the interplay between superconductivity, magnetism, and electronic nematicity, which can be tuned both by chemical substitution and application of physical pressure.

Here we present the first principle study compared with Raman spectroscopy of evolution of vibrational modes of the strained FeSe superconductor. We performed systematic computational study on bulk FeSe crystals with applying in-plane uniaxial strain ranging from -2% to 2% using density functional theory formalism. We focus on the effect of the straining of the lattice constant, and consequent symmetry distortion, on characteristic A_{1g} and B_{1g} modes of FeSe. These numerical findings are compared with experimental data from Raman measurements studying the trend of changes of A_{1g} and B_{1g} modes with applied strain.

The authors acknowledge funding provided by the Institute of Physics Belgrade, through a grant from the Ministry of Science, Technological Development and Innovations of the Republic of Serbia. The work was supported by the Science Fund of the Republic of Serbia, PROMIS, No. 6062656, StrainedFeSC.

CMP

26 - 30 June 2023
Belgrade, Serbia

21. СИМПОЗИЈУМ ФИЗИКЕ КОНДЕНЗОВАНЕ МАТЕРИЈЕ

THE 21st SYMPOSIUM ON CONDENSED MATTER PHYSICS

BOOK OF ABSTRACTS

Institute of Physics
Belgrade

Vinca Institute of
Nuclear Sciences

University of Belgrade,
Faculty of Physics

Serbian Academy of
Sciences and Arts

Ministry of Science, Technological
Development and Innovation

Evolution of Lattice, Spin, and Charge Properties Across $FeSe_{1-x}S_x$ Phase Diagram

A. Milosavljević[a], A. Baum[b,c], L. Peis[b,c], R. Stumberger[b,c], J. Bekaert[d], A. Šolajić[a], J. Pešić[a], Aifeng Wang[e], M. Šćepanović[a], A. M. Milinda Abeykoon[f], M. V. Milošević[d], C. Petrovic[g], Z. V. Popović[h], R. Hackl[b,c,i], and N. Lazarević[a]

[a]Center for Solid State Physics and New Materials, Institute of Physics Belgrade, University of Belgrade, Pregrevica 118, 11080 Belgrade, Serbia
[b]Walther Meissner Institut, Bayerische Akademie der Wissenschaften, 85748 Garching, Germany
[c]Fakultät für Physik, Technische Universität München, 85478 Garching, Germany
[d]Department of Physics, University of Antwerp, Groenenborgerlaan 171, B-2020 Antwerp, Belgium
[e]School of Physics, Chongqing University, Chongqing 400044, China
[f]National Synchrotron Light Source II, Brookhaven National Laboratory, Upton, New York 11973, USA
[g]Condensed Matter Physics and Materials Science Department, Brookhaven National Laboratory, Upton, New York 11973-5000, USA
[h]Serbian Academy of Sciences and Arts, Kneza Mihaila 35, 11000 Belgrade, Serbia
[i]IFW Dresden, Helmholtzstr. 20, 01069 Dresden, Germany

Abstract. It is widely believed that iron-based compounds host unconventional superconductivity. Among them in binary compound FeSe nematic and structural phase transition occurs simultaneously at 90 K and below 9 K superconductivity emerges. In isostructural and isoelectronic FeS, structural phase transition is not observed down to the lowest temperatures. By substituting selenium with sulfur atoms by approximately 20% a zero nematic phase transition temperature is reached suggesting the existence of quantum critical point (QCP). At this point T_c drops down to approximately 2 K [1]. By further increasing the sulfur content, the T_c increase up to 4 K for pure FeS. In order to investigate in which extent the properties and other instabilities of FeSe and FeS are interrelated, the entire substitution range of the $FeSe_{1-x}S_x$ was studied using inelastic light scattering technique. Data were taken as a function of sulfur concentration x for $0 \leq x \leq 1$, of temperature and of scattering symmetry. All types of excitations including phonons, spins, and charges are analyzed. It is observed that the energy and linewidth of the Fe-related B_{1g} phonon mode vary continuously across the entire range. The A_{1g} mode disappears above $x = 0.23$ and reappears at much higher energy for $x = 0.69$. In a similar way the spectral features appearing at finite doping in A_{1g} symmetry vary discontinuously. The magnetic excitation at approximately 500 cm^{-1} disappears above $x = 0.23$ where the A_{1g} lattice excitations exhibit a discontinuous change in energy. The low-energy mode associated with fluctuations displays maximal intensity at the nematostructural transition and thus tracks the phase boundary [2].

REFERENCES

1. A. Wang, A. Milosavljevic, et al., *Inorganic Chemistry* 2022 *61* (29), 11036-11045.
2. N. Lazarević, A. Baum, A. Milosavljević, et al., *Phys. Rev. B* 106, 094510.

Uniaxial Strain-Induced Changes in Vibrational Modes of FeSe

J. Pešić[a], A. Šolajić[a], A. Milosavljević[a] and N. Lazarević[a]

[a]*Center for Solid State Physics and New Materials, Institute of Physics Belgrade,*
University of Belgrade, Pregrevica 118, 11080 Belgrade, Serbia

Abstract. Strain application is an effective method for manipulating the characteristics of materials, and it proves particularly valuable in investigating the impact of local crystal structure changes on physical properties. Iron-based superconductors are ideal candidates for studying this strain dependence due to their heightened sensitivity to variations in crystal structure. Among these superconductors, FeSe stands out as a notable example that showcases the intricate relationship between superconductivity, magnetism, and electronic nematicity. This interplay can be adjusted through both chemical substitution and the application of physical pressure.
In this study, we present a comparison between first-principle calculations and Raman spectroscopy to examine the evolution of vibrational modes in strained FeSe superconductors. Using density functional theory, we conducted a comprehensive computational investigation on bulk FeSe crystals, subjecting them to in-plane uniaxial strain ranging from -2% to 2%. Our primary focus was to analyze the impact of straining the lattice constant and the resulting symmetry distortion on the distinctive A1g and B1g modes of FeSe. These numerical findings were then compared to experimental data obtained from Raman measurements, which allowed us to study the trends in changes of the A1g and B1g modes with applied strain.

Crystal structure and phase transitions in $InSiTe_3$

T. Belojica[a], A. Milosavljević[a], S. Đurđić Mijin[a], A. Šolajić[a], J. Pešić[a], B. Višić[a], Yu Liu[b], C. Petrovic[b], Z. V. Popović[a,c] and N. Lazarević[a]

[a]*Center for Solid State Physics and New Materials, Institute of Physics Belgrade, University of Belgrade, Pregrevica 118, 11080 Belgrade, Serbia*
[b]*Condensed Matter Physics and Materials Science Department, Brookhaven National Laboratory, Upton, NY 11973-5000, USA*
[c]*Serbian Academy of Sciences and Arts, Knez Mihailova 35, 11000 Belgrade, Serbia*

Abstract. Although first report of $InSiTe_3$ single crystal synthesis and its structure dates nearly 30 years ago, only a few studies are available up till today. Unlike its related compounds ($CrSiTe_3$, $CrGeTe_3$) which have been intensively studied, and their high and low temperature physical properties are well established, only resistivity and thermal conductivity, as well as theoretical predictions of thermodynamical and mechanical stability of $InSiTe_3$ were investigated. Probably, one of the main issues causing lack of research data is the proper determination of $InSiTe_3$ crystal structure, since the literature predicts three different space groups for this material, $P3$, $P\bar{3}$, and $P\bar{3}1m$.

In order to properly investigate $InSiTe_3$ crystal structure we employed inelastic light scattering technique, and DFT calculations for all suggested crystal structures. Six out of eight and seven out of ten Raman active modes for proposed $P\bar{3}1m$ and $P\bar{3}$ space groups, respectively, are observed and assigned, in agreement with numerical calculations. The theoretical calculations for $P3$ crystal structure are in a strong discrepancy with theoretical results, hence this proposed space group can be neglected. The obtained results suggest the coexistence of two triagonal crystal phases, high symmetry one, $P\bar{3}1m$ and low symmetry $P\bar{3}$ space group. Additionally, to the modes that are theoretically predicted, at around 500 cm^{-1} the A_{1g}/A_g "splitting" mode is detected. The appearance of this peak might be a consequence of local symmetry breaking due to a small difference in lattice parameters of both crystal phases. The temperature dependence of energies and linewidths of the most prominent Raman active modes show a monotonous decrease in energy and increase in linewidth when the material is heated from 80 K. At around 200 K discontinuities in phonon properties can be observed. Above the same temperature, additional features in Raman spectra between 175 and 300 cm^{-1} only in parallel scattering configuration are present, and may be a consequence of two-phonon processes. The phonon temperature dependence and these additional excitations indicate the presence of some kind of phase transition above 200 K. Due to the lack of theoretical and experimental studies the origin and type of this transition remains an open question and requires further analysis.

Effect of disorder and electron-phonon interaction on 2*H*-$TaSe_{2-x}S_x$ lattice dynamics

Jovan Blagojević[1], Sanja Đurđić Mijin[1], Ana Milosavljević[1], Marko Opačić[1], Jonas Bekaert[2], Milorad Milošević[2], Zoran Popović[3] and Nenad Lazarević[1]

[1]Institute of Physics, University of Belgrade, Pregrevica 118, 11080 Belgrade, Serbia
[2]Department of Physics & NANOlab Center of Excellence, University of Antwerp, Groenenborgerlaan 171, B-2020 Antwerp, Belgium
[3]Serbian Academy of Sciences and Arts, Knez Mihailova 35, 11000 Belgrade, Serbia

Abstract. Quasi-2D materials have gained a significant attention in the last few years because of their unique physical properties. The family of transition metal dichalcogenides is particularly intriguing due to their complex phase diagrams, characteristic optical properties and possibility to observe collective electron phenomena at higher temperatures. A strong correlation was observed between the electron-phonon interaction and the CDW phase in materials that display such states. Recent study has revealed that crystalline disorder promotes superconductivity while simultaneously suppresses CDW phase in metallic single crystal alloys of 2H-$TaSe_{2-x}S_x$.

Raman spectroscopy was used to investigate the effect of defects on lattice dynamics and electron-phonon coupling in these materials, and the results were compared to theoretical calculations. In our scattering configuration two out of four Raman active modes predicted by symmetry for parent compounds are identified. Additionally, in the spectra of pure samples broad two-phonon structures are observed, emerging as a consequence of strong electron-phonon coupling in related phonon branches. By substituting Se with S atoms, extra peak obeying A_{1g} selection rules, overtone in nature, appears in spectra along with an intriguing evolution of two-phonon structure. The Raman spectra of the $x = 0.84$ sample shows single-phonon excitations that are superimposed on already existing structure. These excitations correspond to PDOS maxima projected due to significant crystallographic disorder. Symmetry predicted A_{1g} modes expectedly harden with doping as unit cell volume decreases, whereas E_{2g} modes exhibit anomalous behavior attributed to enhanced electron-phonon coupling. The analysis of E_{2g} mode Fano parameter indicates that disorder has a minor impact on electron-phonon interaction.

21th International Workshop on Computational Physics and Materials Science: Total Energy and Force Methods | (SMR 3814)

11 Jan 2023 - 13 Jan 2023
ICTP, Trieste, Italy

P01 - ABDURRAZAQ Abdulgaffar

Tricking germanium to open the band gap

P02 - ACHEHBOUNE Mohamed

Atomic scale nucleation and formation mechanism of hexagonal boron nitride (hBN) on graphene and Germanium : A DFT study

P03 - ADAK Abhishek Kumar

Insights from density functional theory into the formation and rotation of an enantiospecific assembly of molecular raffle wheels

P04 - ARTACHO CORTÉS Martin Emilio Martin

Floquet Theory of Electronic Stopping of nuclei projectiles in solids

P05 - ASHANI Mitonji Timothy

Exploring plasmon properties of the Dirac compound LiNa2Bi using TDDFT.

P06 - ATAEI Seyedeh Samaneh

Interlayer Excitons in 2D TMD Heterostructures

P07 - ATTIA Mahmoud Mostafa Elsayed

Li vs. Na Solid-State based Batteries : Modelling of Diffusion in Solid Electrolytes

P08 - AZIZI Khatereh

Investigation of the structural complexity of aqueous systems through machine learning

P09 - BANERJEE Debarshi

Development of a computational toolbox to analyse first-passage times and diffusion coefficients in heterogeneous soft-matter systems

P10 - BHATTACHARYA Sanchari

Signature of cubic and linear Rashba in LaAlO3 /KTaO3 (0 0 1) heterostructure

P11 - BIDOGGIA Davide

Ab-initio characterization of CoTPyP and CoTPyP-Co metalorganic monolayers for catalytic application

P12 - BINCI Luca

Noncollinear relativistic Hubbard parameters and DFT+U with ultrasoft pseudopotentials

P13 - BONACCI Miki

Automated Many-Body Perturbation Theory

P14 - BORGHESI Costanza

Tailoring High-Entropy Oxides (HEOs) as Emerging Radiative Materials for Green Energy Buildings

P15 - BOUCHRIT Abir

The effect of vacancies on the thermoelectric properties of half-Heusler materials

P69 - MONACELLI Lorenzo

Computing the phase diagram of strongly anharmonic crystals. CsSni3: the route to eco-friendly solar cells

P70 - MORRESI Tommaso

Anharmonic Phonons From Path Integral Molecular Dynamics Simulations

P71 - MULWA Winfred Mueni

Atomistic Study of an Ideal Thermoelectric Contact: the Full – Heusler / Half – Heusler Interface

P72 - MUŽEVIĆ Matko

Tuning of MoS2 band structure with atom intercalation during synthesis

P73 - NEUPANE Krishna Hari

Effect of N & C sites vacancy defects in (G/h-BN) HS of 2D materials

P74 - NGUYEN Truong Truong Long

Structural prediction of group IV monochalcogenides and their pressure-induced transitions mechanism

P75 - NKOU Falonne Bertholde Sharone

Selective oxidation of ethylene glycol on transition metal oxide under dry and humid conditions from ab-initio molecular dynamics approach

P76 - NOURBAKHSH Zahra

An ab initio supercell approach for high-harmonic generation in liquids

P77 - NUNEZ AVILA Jose Andres

Lattice dynamics and electron-phonon coupling in Fe_{1-x}Co_xGe: effects of magnetism

P78 - OMRANPOOR Amir Hossein

Ab initio Molecular Dynamics Study of 2-propanol Oxidation at Co3O4(001)/H2O Interface

P79 - PANDEY Dhanshree

Theoretical Studies On Investigation Of Gas Adsorption and Sensing On 2-Dimensional Surfaces

P80 - PAVLIN Matic

Effects of Solvation on Reduction of Carbon Dioxide on Copper Electrocatalyst

P81 - PEGOLO Paolo

Hydrodynamic contributions to the thermal conductivity of amorphous materials in the infinite-size limit

P82 - PEREIRA CARDOSO Claudia Maria

GW multipole approach for the frequency description of the dielectric screening in metals

P83 - PEŠIĆ Jelena

The Evolution of Vibrational Modes of FeSe Under Uniaxial Strain

P84 - PETERSON Ann Elizabeth Ann

Elucidating the chiral anomaly in Dirac materials via electronic structure calculations

P85 - PEZO LOPEZ Armando Arquimedes

Orbital Hall effect in 2D Dirac materials

P86 - PIRES FERREIRA Pedro

P83

The Evolution of Vibrational Modes of FeSe Under Uniaxial Strain

Jelena Pešić, Andrijana Šolajić, Ana Milosavljević, Sanja Đurđić Mijin, Borislav Vasić, Novica Paunović and Nenad Lazarević

Center for Solid State Physics and New Materials, Institute of Physics Belgrade, Serbia

Application of strain is one of the effective ways to engineer the various properties of materials. Iron-based superconductors are suitable materials to study the strain dependence of physical properties due to their high sensitivity to variations in the local crystal structure. Among the iron-based superconductor family, FeSe is a prominent example of the interplay between superconductivity, magnetism, and electronic nematicity, which can be tuned both by chemical substitution and by application of physical pressure and consequent lattice distortions [1].

Here we present a first principle study of evolution of vibrational modes of the strained FeSe. We performed a systematic computational study, using density functional theory formalism, on bulk FeSe crystals with applying the in-plane uniaxial strain in B_{1g} and B_{2g} symmetry channels, in the range -1.5% to 1.5%. For the calculation, we used the experimental parameters and the volume cell of the unit cell is conserved under applied uniaxial strain [2].

We focus on the effect of the modification of the lattice constant, and the consequent symmetry distortion, on characteristic A_{1g} and B_{1g} modes of FeSe. These findings are compared with experimental data from Raman measurements, studying the trend of changes of A_{1g} and B_{1g} modes with applied strain using a piezoelectric strain device. The sample was mounted in such a way that the strain was applied in the *ab*-crystallographic plane and that the direction of incident light propagation is along the crystallographic *c*-axes. The sample orientations were set so that [110] (B_{2g}) and [100] (B_{1g}) crystallographic directions were orthogonal to a gap between the holder plates.

The work was supported by the Science Fund of the Republic of Serbia, PROMIS, No. 6062656, StrainedFeSC [3].

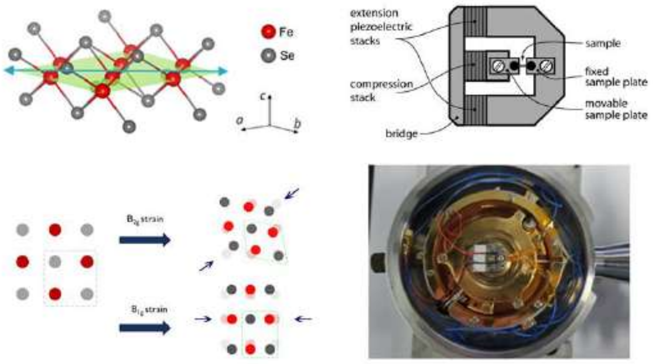

Left: Schematic representation of applied strain, Right: piezoelectric strain device, schematic and photography

[1] M. Ghini et al. Strain tuning of nematicity and superconductivity in single crystals of FeSe, Physical Review B,103, 205139 (2021)

[2] Willa, R. et al. Strain tuning and anisotropic spin correlations in iron-based systems. Physical Review B, 100(8) (2019).

[3] http://strainedfesc.ipb.ac.rs/

INSTITUTE OF TECHNICAL SCIENCES OF SASA
MATERIALS RESEARCH SOCIETY OF SERBIA

Programme and the Book of Abstracts

TWENTIETH YOUNG RESEARCHERS' CONFERENCE MATERIALS SCIENCE AND ENGINEERING

Belgrade, November 30 – December 2, 2022

7-1

Crystal structure of $InSiTe_3$ studied by Raman spectroscopy

Ana Milosavljević[1], Sanja Đurđić[1], Tea Belojica[1], Andrijana Šolajić[1], Jelena Pešić[1], Bojana Višić[1], Yu Liu[2], Cedomir Petrovic[2], Zoran V. Popović[1,3], Nenad Lazarević[1]
[1]Center for Solid State Physics and New Materials, Institute of Physics Belgrade, University of Belgrade, Pregrevica 118, 11080 Belgrade, Serbia, [2]Condensed Matter Physics and Materials Science Department, Brookhaven National Laboratory, Upton, NY 11973-5000, USA, [3]Serbian Academy of Sciences and Arts, Knez Mihailova 35, 11000 Belgrade, Serbia

Even though the first report of $InSiTe_3$ single crystal synthesis and its structure dates from about 30 years ago, unlike its related compounds ($CrSiTe_3$, $CrGeTe_3$), there has been only a few studies availabile. One of the reasons behind the lack of research data is the fact that its crystal structure is not unambigously determined. Raman scattering study of of $InSiTe_3$ reveals presence of six ($3A_{1g} + 3E_g$) out of eight and seven ($5A_g + 2E_g$) out of ten Raman active modes for proposed $P\bar{3}1m$ and $P\bar{3}$ space groups, respectively. These results suggest the coexsistence of two triagonal crystal phases, high symmetry one, $P\bar{3}1m$ and a lower symmetry one, which corresponds to $P\bar{3}$ space group. The theoretical predictions obtained by DFT calculations for both space group support this scenario. In addition to the symmetry predicted modes, at around 500 cm^{-1} a mode ascribed to the A_{1g}/A_g mode „splitting“ is detected. The emergence of additional peak could be a consequence of local symmetry breaking due to a small difference in lattice parameters of both crystal phases. The temperature dependence of energies and linewidths of most prominent Raman active modes is also presented in the temperature range from 80 to 300 K. Monotonous decrease in energy and increase in linewidth is present upon heating up to 200 K. Around this temperature discontinuities in properties of all analyzed modes are detected. Yet, due to lack of theoretical and experimental studies of this material this anomaly still remains an open question.

7-2

Optical properties of nanostructured multi-stoichiometric tungsten suboxides

Bojana Višić[1,2,3], Luka Pirker[1,3], Marko Opačić[2], Ana Milosavljević[2], Nenad Lazarević[2], Boris Majaron[3,4], Maja Remškar[1]
[1]Department of Condensed Matter Physics, Jozef Stefan Institute, Jamova Cesta 39, 1000 Ljubljana, Slovenia, [2]Institute of Physics Belgrade, University of Belgrade, Pregrevica 118, 11080 Belgrade, Serbia, [3]Department of Complex Matter, Jozef Stefan Institute, Jamova 39, 1000 Ljubljana, Slovenia, [4]Faculty of Physics and Mathematics, University of Ljubljana, Jadranska 19, Slovenia

Tungsten suboxide ($WO_{3–x}$) nanomaterials were synthesized via chemical vapor transport method and the role of their crystal structures on the optical properties was investigated. These materials grow either in the shape of platelets or nanotiles, or as nanowires (W_5 O_{14}, $W_{18}O_{49}$). For the first one which represents thin quasi-2D materials, the appearance of defect states gives rise to two indirect absorption edges. One is assigned to the regular bandgap between the valence and the conduction band, while the second is a defect-induced band. While the bandgap values of platelets and nanotiles are in the upper range of the reported values for the suboxides, the nanowires’ bandgaps are lower due to the higher number of free charge carriers. Both types of nanowires sustain localized surface plasmon resonances, as evidenced from the extinction measurements, whereas the quasi-2D materials exhibit excitonic transitions. Photoluminescence emission peaks in the UV region were detected for all four materials. The interplay of the crystal structure, oxygen vacancies and shape can result in changes in optical behavior, and the understanding of these effects could enable intentional tuning of selected properties.